LBL-36515
UC-400

Lawrence Berkeley Laboratory
UNIVERSITY OF CALIFORNIA

EARTH SCIENCES DIVISION

Contact Micromechanics in Granular Media with Clay

S.L. Ita
(Ph.D. Thesis)

August 1994

Prepared for the U.S. Department of Energy under Contract Number DE-AC03-76SF00098

LBL-36515
UC-400

Contact Micromechanics in Granular Media with Clay

Stacey Leigh Ita
PhD. Thesis

Materials Science and Mineral Engineering Department
University of California, Berkeley

and

Earth Sciences Division
Lawrence Berkeley Laboratory
University of California
Berkeley, CA 94720

August 1994

This work was supported by the Director, Office of Energy Reserarch, Office of Basic Energy Sciences, Materials Sciences Division, of the U.S. Department of Energy under Contract No. DE-AC03-76F00098.

Contact Micromechanics in Granular Media with Clay

by

Stacey Leigh Ita

B.A. (University of California at Berkeley) 1988
M.Eng. (University of California at Berkeley) 1991
M.S., (University of California at Berkeley) 1994

A dissertation submitted in partial satisfaction of the

requirements for the degree of

Doctor of Philosophy

in

Engineering-Materials Science
and Mineral Engineering

in the

GRADUATE DIVISION

of the

UNIVERSITY of CALIFORNIA at BERKELEY

Committee in charge:

Professor Neville G.W. Cook, Chair
Doctor Larry R. Myer
Professor James W. Rector
Professor Keith Loague

1994

Contact Micromechanics in Granular Media with Clay

by

Stacey Leigh Ita

ABSTRACT

Contact Micromechanics in Granular Media with Clay

by

Stacey Leigh Ita

Doctor of Philosophy in Engineering

University of California at Berkeley

Professor Neville G.W. Cook, Chair

Many granular materials, including sedimentary rocks and soils, contain clay particles in the pores, grain contacts, or matrix. The amount and location of the clays and fluids can influence the mechanical and hydraulic properties of the granular material. This research investigated the mechanical effects of clay at grain-to-grain contacts in the presence of different fluids. Laboratory seismic wave propagation tests were conducted at ultrasonic frequencies using spherical glass beads coated with Montmorillonite clay (SWy-1) onto which different fluids were adsorbed.

For all bead samples, seismic velocity increased and attenuation decreased as the contact stiffnesses increased with increasing stress demonstrating that grain contacts control seismic transmission in poorly consolidated and unconsolidated granular material. Coating the beads with clay added stiffness and introduced viscosity to the mechanical contact properties that increased the velocity and attenuation of the propagating seismic wave. Clay-fluid interactions were studied by allowing the clay coating to absorb water, ethyl alcohol, and hexadecane. Increasing water amounts initially increased seismic attenuation due to clay swelling at the contacts. Attenuation decreased for higher water amounts where the clay exceeded the plastic limit and was forced from the contact areas into the surrounding open pore space during sample consolidation. The decreased clay thickness at

the contacts increased the contact stiffness and decreased attenuation. Attenuation was larger for clay with absorbed ethyl alcohol and hexadecane than for similar water amounts.

Both compressional and shear waves cause the clay-coated contacts to move towards and away from one another resulting in pumping loss due to viscous deformation of the clay. Pumping loss attenuation will depend on the contact microgeometry and material viscosity.

The grain contacts were shown to behave as low-pass filters by use of a Butterworth mathematical filter. Analyses of the mechanics of contact stiffness were made using effective modulus and discontinuity theories. Numerical modeling was performed on idealized columns of grains coupled by discontinuous displacement and discontinuous velocity boundary conditions. The numerical trials accurately simulated the laboratory velocity and attenuation variations, confirming the experimental interpretations of the dominance of contact stiffness on wave propagation.

_____

Chair Date

TABLE OF CONTENTS

List of Figures

List of Tables

List of Symbols

Symbol	Description	Units
a	Scatterer size	m
α	Attenuation coefficient	Nepers/m
b	Diameter of capillary tubes	m
B_{local}	Constant depending on fluid properties used in Biot flow attenuation	-
C	Coordination Number	-
C_c	Clay content	kg-clay/kg-sample
c	Velocity	m/sec
c_p	Compressional wave velocity	m/sec
c_s	Shear wave velocity	m/sec
χ	Proportionality constant	-
D	Displacement of a Hertzian contact	m
D_{el}	Dielectric constant	-
e	Electron charge	C
E	Elastic Modulus	Pa
E_y	Young's Modulus	Pa
E'	Effective Elastic Modulus	Pa
ε_{ij}	Strain tensor	-
ε_o	Static permittivity	F/m
f	Frequency	Hz
f_c	Critical Frequency	Hz
F	Force on sphere	N
ϕ	Porosity	-

Symbol	Description	Units
$G(f)$	Geometrical correction factor	-
η	Viscosity	Pa-s/m
η_f	Fluid viscosity	Pa-s/m
η_{sp}	Specific viscosity	Pa-s/m
k	Wavenumber	-
k_B	Boltzmann constant	J/K
K	Stiffness	Pa/m
K_c	Contact Stiffness	Pa/m
K_i	Imaginary component of specific stiffness	Pa/m
K_r	Real component of specific stiffness	Pa/m
K_{sp}	Specific Stiffness	Pa/m
$1/K_{DL}$	Double Layer Thickness	m
κ	Permeability	m^2
L	Length of sample	m
λ	Wavelength	m
	Lame's constant	Pa
μ	Shear modulus	Pa
	Lame's constant	Pa
n	Number of interfaces	-
n_o	cation concentration	eq/liter
N	Total number of data points	-
N_d	Number of contacts displacing	-
N_e	Effective number of contacts	-
N_p	Number of particles	-
ν	Poisson's ratio	-

Symbol	Description	Units
P_e	Effective Pressure	Pa
ρ	Density	kg/m^3
ρ_f	Fluid Density	kg/m^3
Q	Quality Factor	-
R	Radius of grain	m
s	Slowness vector	sec/m
SE	Strain Energy	1/Pa
σ_{ij}	Stress tensor	Pa
t	Time	sec
T	Temperature	K
$T(f)$	Transmission coefficient	-
u	Displacement	m
u_o	Initial Displacement	m
v	Cation valence	-
V	Volume	m^3
x	Distance	m
x(n)	Windowed trace	V
$X(f)$	Fourier transform of windowed trace	V/(# of points)
Z	Impedance	Pa-s/m

Acknowledgements

My sincere thanks are owed foremost to my advisor, Professor Neville Cook. He has been a constant source of inspiration to me since my undergraduate days. It is due to his enouragement that I entered graduate school and pursued a doctorate. He has been a true mentor and it has been a privelege to be a part of his research group. Dr. Larry Myer also deserves my most earnest thanks for being my co-research advisor. His guidance and support were above and beyond the call of duty. I was very fortunate to work with these two remarkable investigators. Dr. Kurt Nihei was very generous with his time in discussing my ideas and reviewing this material.

I am grateful to Professors Keith Loague and Jamie Rector for serving on my thesis committee. Their attentive reviews have improved this material. Also, I wish to thank Professors George Cooper, Fiona Doyle, Nari Narasimhan, and Gene Rochlin for their participation in my preliminary and qualifying examinations. Their thoughtful questions and discussions made these encounters stimulating and insightful, rather than arduous. I am particularly endebted to Gene Rochlin for his moral support over the past year. He has helped to make a difficult situation tolerable.

I wish to thank Dr. Kurt Nihei, Dr. Roberto Suárez-Rivera, and (Dr.?) Galen Hesler for introducing me to the laboratory when I first began. The cooperative atmosphere they created provided an invaluable setting for learning experimental research. My office-mates - Brun Hilbert, Taylor Hwong, and recently Brad Bessinger - deserve special recognition. They have been very understanding and become good friends. My best wishes to the new experimentalists in the group: Jianli Fan and Seiji Nakagawa. Thank you for keeping me company over the last nights of this dissertation.

I owe deepest appreciation to my family. My mother Dorothy has taught me to love and value knowledge. She has been an enthusiastic supporter of my seemingly never-ending studies. My sister Kimberlee has endured countless delays on my part, as I defered

my family obligations during numerous academic deadlines. Her understanding has been greatly appreciated. Most importantly, I am indebted to my husband Joel. His continual encouragement, consideration, and love have supported me through graduate life. He is my sunshine, and I look forward to the many years ahead.

Chapter 1: Introduction

1.1 Introduction

Seismology is the study of sound waves in solid media. The velocities of propagating sound waves can be used to determine the elastic properties of the material. This has allowed the material structure to be delineated. Surveys have been performed on a wide-range of scales, from the interior of the earth to laboratory specimens. Practical applications have included resource exploration, foundation analysis, and contaminant transport surveys.

Recent improvements in field seismic measurement tools now allow for recording of the full seismic waveform. The increased information available has generated renewed interest in characterizing geomaterials from their seismic behavior, a process called seismic imaging. In particular, many studies have concluded that "attenuation is much more sensitive to rock properties than is velocity" (Winkler and Nur, 1982). Rock properties of most interest include minearology, porosity, permeability, and pore fluid type.

Despite extensive research, there is still considerable uncertainty over the relationships between rock properties and seismic behavior. This may be partially due to the effect of clays. Clays can be located in the pores, contacts, and matrix of granular materials (Figure 1.1). Clays have small size, large surface areas, and a negative charge. Because of these properties, clays may have important effects on the rock properties. The surface charge of clay will cause it to interact with the pore fluid. Clays at contacts may control the permeability by clogging critical pore throats in the flowpaths. In addition, clay at contacts may control the rock elastic behavior due to their high compressibilities.

Illustration of Clay Minerals in Granular Media

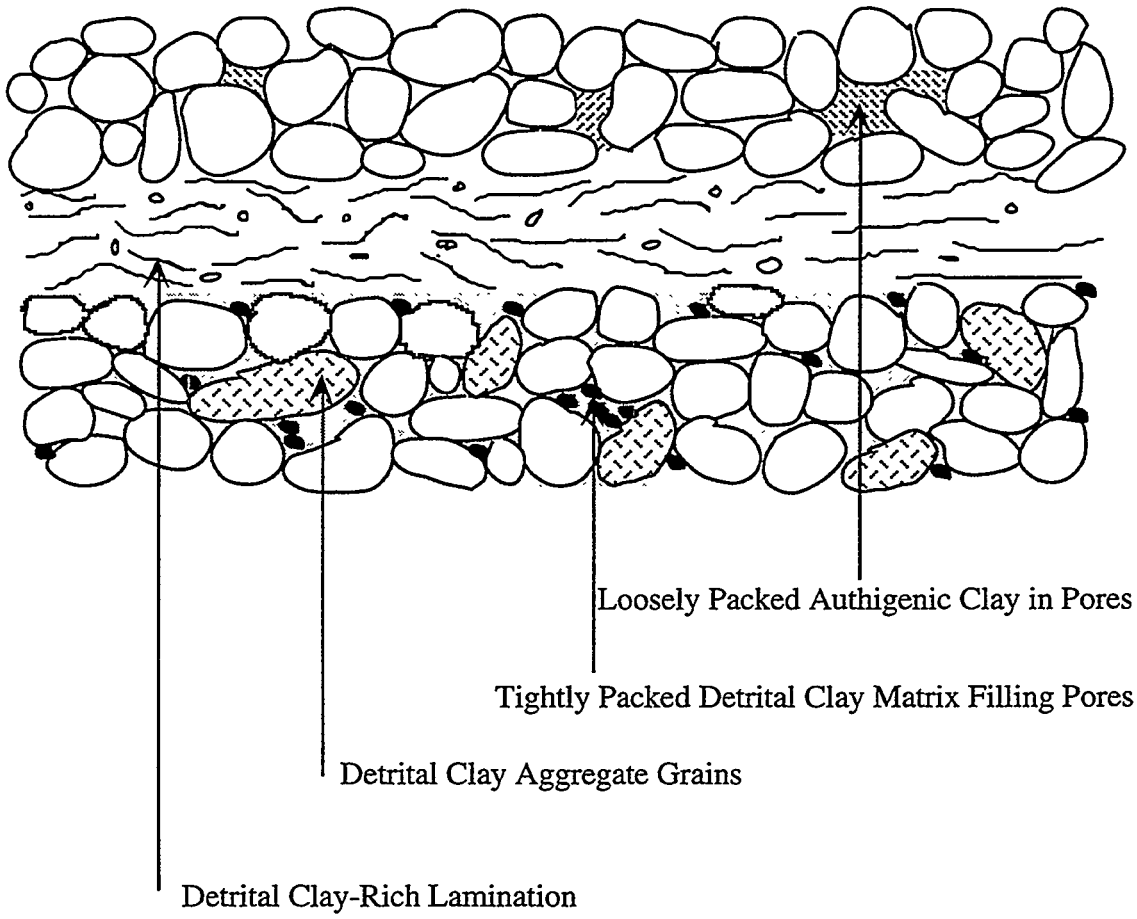

Figure 1.1: Illustration of clay types and locations in granular media. Clay can be located in pores, at contacts, or as part of the granular matrix (After Pittman and Thomas, 1979).

This work investigates how clay located at grain contacts affects the micromechanical, particularly seismic, behavior of granular materials. The need for this work is shown by a review of the effects of clays on seismic wave propagation, laboratory measurements of attenuation in granular media, and proposed mechanisms for attenuation in granular media.

1.2 Effect of Clays

Laboratory investigations have shown that seismic velocities are dependent on the presence of clays. The first studies showed that scatter in the velocity-porosity relationships for consolidated rocks could be partially explained by clay content (DeMartini *et. al.*, 1976; Tosaya and Nur, 1982; Kowallis *et. al.*, 1984). In general, they found that increasing clay content systematically decreases acoustic velocities. Subsequent work has attempted to quantify the effect of clay content by measuring samples with a wide-range of properties. These studies established empirical relationships between velocities, porosities, clay contents, and other factors. The empirical relationships are listed in Figure 1.2. The negative coefficient of clay content in the velocity equations shows that an increase in clay content decreases the velocity. The majority of the relationships show that the effect of clay is on the same order of magnitude, but smaller, than the effect of porosity. The standard deviations between the measured data and the mathematical relationships are quite small, typically less than five percent.

These empirical relationships are of limited utility beyond demonstrating the dependence of velocity on clay content. Tutuncu *et. al.* (1994) attempted to apply them to data from water-saturated tight gas sandstones with poor correlation. This can partially be explained by the differences in rock type. However, a major problem with these equations

Velocity - Porosity - Clay Content

Tosaya and Nur (1982), Brine and Water-Saturated Sandstones

$$c_p = 5.8 - 8.6\phi - 2.4C_c$$

Han, Nur, and Morgan (1986), Water-Saturated Sandstones

$$c_p = 5.59 - 6.93\phi - 2.18C_c$$
$$c_s = 3.52 - 4.91\phi - 1.89C_c$$

Velocity - Porosity - Clay Content - Permeability

Klimentos (1991), Water-Saturated Sandstones

$$c_p = 5.66 - 6.11\phi - 3.53C_c + 0.0007\kappa$$

Velocity - Porosity - Clay Content - Effective Pressure

Eberhart-Phillips *et. al.* (1989), Water-Saturated Sandstones

$$c_p = 5.77 - 6.94\phi - 1.73\sqrt{C_c} + 0.446\left(P_e - e^{-16.7P_e}\right)$$
$$c_s = 3.70 - 4.94\phi - 1.57\sqrt{C_c} + 0.361\left(P_e - e^{-16.7P_e}\right)$$

Attenuation - Porosity - Clay Content

Klimentos and McCann (1990), Water-Saturated Sandstones

$$\alpha_p = 0.0315\phi + 0.241C_c - 0.132$$

Table1.1: Empirical relationships between (a) velocity c, porosity ϕ, clay content C_C, effective pressure P_e, and permeability κ and (b) attenuation α, porosity, and clay content. The negative coefficient of clay content in the velocity equations indicates that it reduces velocity. In general, the clay content effect is smaller but of the same order of magnitude as the porosity effect. The positive coefficient of clay content in the attenuation equation indicates that it increases attenuation. The clay content effect on attenuation is an order of magnitude larger than the porosity effect.

is the fact that they are insensitive to clay location. Clays can be distributed throughout the granular material, including in the large pores or at contacts.

By consideration of a thin section, Anstey (1991) has discussed the relationship between petrophysical properties and seismic velocities. He concludes that an important property is the clay location. Clay that is located in the pores will both decrease the seismic velocity by increasing the density of the pores and concurrently increase the seismic velocity by increasing the stiffness or modulus of the pores. Similarly, clay at contacts can have contrasting effects. If the clay forms a link between grains, thereby increasing the number of contacts, the presence of clay will increase the velocity. However, clay at existing contact areas is more compliant than the matrix, decreasing the seismic velocity.

The effect of clay location on seimic wave propagation has not been thoroughly studied. Marion (1990) has investigated the acoustic velocity and porosity behavior in a full range of clay-sand mixtures. He found that as clay content increased from pure sand, the porosity initially decreased to a minimum between 20 to 40% clay content. The porosity then incrementally increased to the pure clay sample. The compressional velocity had the opposite trend. Velocity initially increased to a maximum at approximately 40% clay content, then decreased to 100% clay content. Marion developed a micro-geometrical mixture model to explain this behavior. The porosity minima and velocity maxima represent the point where the mixture changes from clays dispersed in the pores of a sand matrix to sand grains dispersed in a clay matrix. The model reproduces the general trend of measured data, but does not make attenuation measurements and does not fully account for the scatter in the data, possibly because it does not account for clay rheology effects. It confirms the importance of clay location during seismic wave propagation.

Few studies have examined the relationship between clay content and seismic attenuation. Clark *et. al.* (1980) observed that as water content increased attenuation decreases were larger in sandstones with clays than clay-free sandstones. Klimentos and McCann (1990) measured attenuation as a function of porosity, clay content, and permeability for 42 water-saturated sandstones. They calculated an empirical dependence, given in Table 1.1. According to the equation, as clay content increases the attenuation increases. The coefficients show that the clay content effect on attenuation is an order of magnitude larger than the porosity effect.

Seismic attenuation by thin layers of clay located at planar contacts has been investigated by Suárez-Rivera (1992). Compressional waves were insensitive to the presence of thin clay layers. Shear wave peak-to-peak amplitudes, an indicator of attenuation, were sensitive to the addition of polar fluids as shown in Figure 1.2. The effects were attributed to clay swelling. This study shows that clay located at planar contacts can have large effect on seismic wave propagation. These studies suggest that clay located at granular contacts may also have significant effects.

1.3 Laboratory Measurements of Attenuation

Seismic attenuation in sedimentary rock has been the subject of considerable laboratory research. Comprehensive reviews of the research can be found in Toksöz and Johnston (1981), White (1983), Vassiliou *et. al.* (1984), Yale (1985), Bourbie *et. al.* (1987). The results are summarized here.

A number of different techniques have been used to measure attenuation in the field (*in situ*) and laboratory. Table 1.2 details the frequency ranges and typical wavelengths for the various techniques. Laboratory techniques include stress-strain, resonant bar, and

Seismic Tranmission Across a Single, Sodium-Montmorillonite Coated Planar Contact

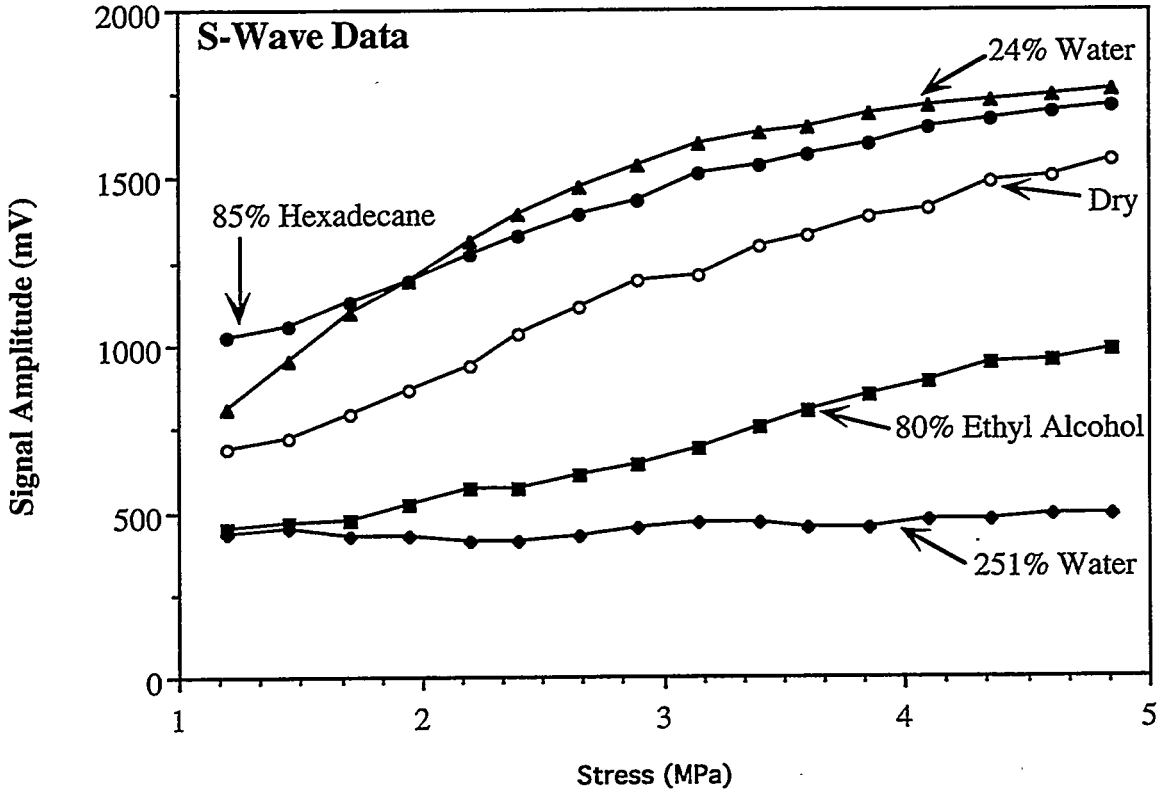

Figure 1.2: Peak-to-peak amplitudes across a single, sodium-montmorillonite coated planar contact under uniaxial stress. Peak-to-peak amplitudes are an indicator of attenuation. The percentages are measures of water content (weight water/weight clay). (After Suárez-Rivera, 1992).

Seismological Frequency Spectrum

Frequency	Wavelength (m) for V=4000 m/s	Frequency Range	*In Situ* Technique	Laboratory Measurement Technique
10^{-1}	4×10^{4}	Seismic		
			Earthquakes	
10^{0}	4×10^{3}			
10^{1}	4×10^{2}			
			Surface Reflection	Stress-Strain Curve
10^{2}	40	Acoustic		
			Cross-Borehole	Resonant Bar
10^{3}	4			
			Echo Sounders	
10^{4}	0.4	Ultrasonic		
			Borehole Logging	Waveform Inversion
10^{5}	4×10^{-2}			
				Pulse Transmission
10^{6}	4×10^{-3}			

Table 1.2: Frequency spectrum and associated wavelengths for seismological investigations of rocks. The *in situ* and laboratory techniques are in the indicated ranges. Based on Bourbie *et. al.* (1987) and Nihei (1992).

pulse transmission and echo measurements. Studies have shown that the measurement of attenuation will depend on the testing conditions, including compaction, confining stress, frequency, and strain amplitude. Most studies have shown that in the hertz to kilohertz range attenuation is approximately independent of frequency for dry rocks, but depends on frequency for saturated rocks. Attenuation varies with saturation. It is lowest for completely dry rocks, and increases as the first few layers of fluid are adsorbed. For compressional waves, attenuation is lower for fully saturated than partially saturated conditions. The opposite is true for shear waves. Attenuation will depend on the pore fluid properties of dipole moment, surface tension, and viscosity. Microgeometrical properties can also affect attenuation, including grain size, grain shape, and grain packing.

Recent studies have emphasized the importance of grain contacts and cementation (Nihei, 1992; Dvorkin *et. al.*1994). The seismic attenuation in unconsolidated and fused glass bead samples were compared by Winkler (1983). Fused bead attenuation was found to be independent of saturation while unconsolidated attenuation depended on saturation. The differences were attributed to the differences in crack geometry, with unconsolidated samples having more low aspect ratio "cracks" near contacts. Bourbie and Zinszner (1985) determined that the the differences in seismic velocities and attenuations for Fontainbleau sandstones at the same porosities could be explained by different microstructures. The sample with the porosity at grain contacts had a higher attenuation. Remy *et. al.* (1994) have measured attenuation during repeated freeze-thaw cycles. They attributed the increases in seismic attenuation to creation of microcracks.

The importance of contacts was confirmed by pore isolation studies conducted by Nihei (1992). Molten sulfur and Wood's metal were introduced into the pore space of Berea Sandstone samples and then allowed to solidify in pace to isolate the effects of pores

and grain contacts. Sulfur is a wetting fluid, and will move into the grain contacts. Once solid, it should lessen the effects of grain contacts on seismic wave propagation by partially welding the contacts. Wood's metal is a non-wetting fluid that remains in the larger pores. When solidifed, it reduces the influence of the large pores on seismic wave propagation. Attenuation data measured in these altered samples and a dry reference sample are shown in Figure 1.3. It can be seen that the introduction of both low melting point solids significantly reduces attenuation. This confirms that grain contacts are at least as important as pores for attenuation. The importance of grain contacts on seismic wave attenuation was also noted by Palmer and Traviolia (1980). They found that the introduction of a fluid layer between simulated grain contacts increased attenuation by two to three orders of magnitude over direct contacts.

1.4 Attenuation Models for Granular Media

Propagating seismic waves lose some of their energy due to attenuation. Recent studies have shown that attenuation depends on the petrophysical properties of the granular material, including permeability, porosity, grain size, grain shape, clay content, clay location, pore fluid type and pore fluid amount (Vassiliou *et. al.*, 1984; Han *et. al.*, 1986; Klimentos and McCann, 1990; Marks *et. al.*, 1992; Prasad and Meissner, 1992). Winkler and Nur (1982) found that attenuation was significantly more sensitive to changes in these rock properties than were velocities. Measurements of attenuation therefore can provide a potential means of estimating these parameters *in situ.*

Petrophysical properties are interpreted from measurements of seismic attenuation by using theoretical models. A list of proposed models based on different mechanisms is given in Table 1.3. The application of a particular model will depend on the given conditions. In particular, surface energy, squirt fluid flow, bubble resonance frequency,

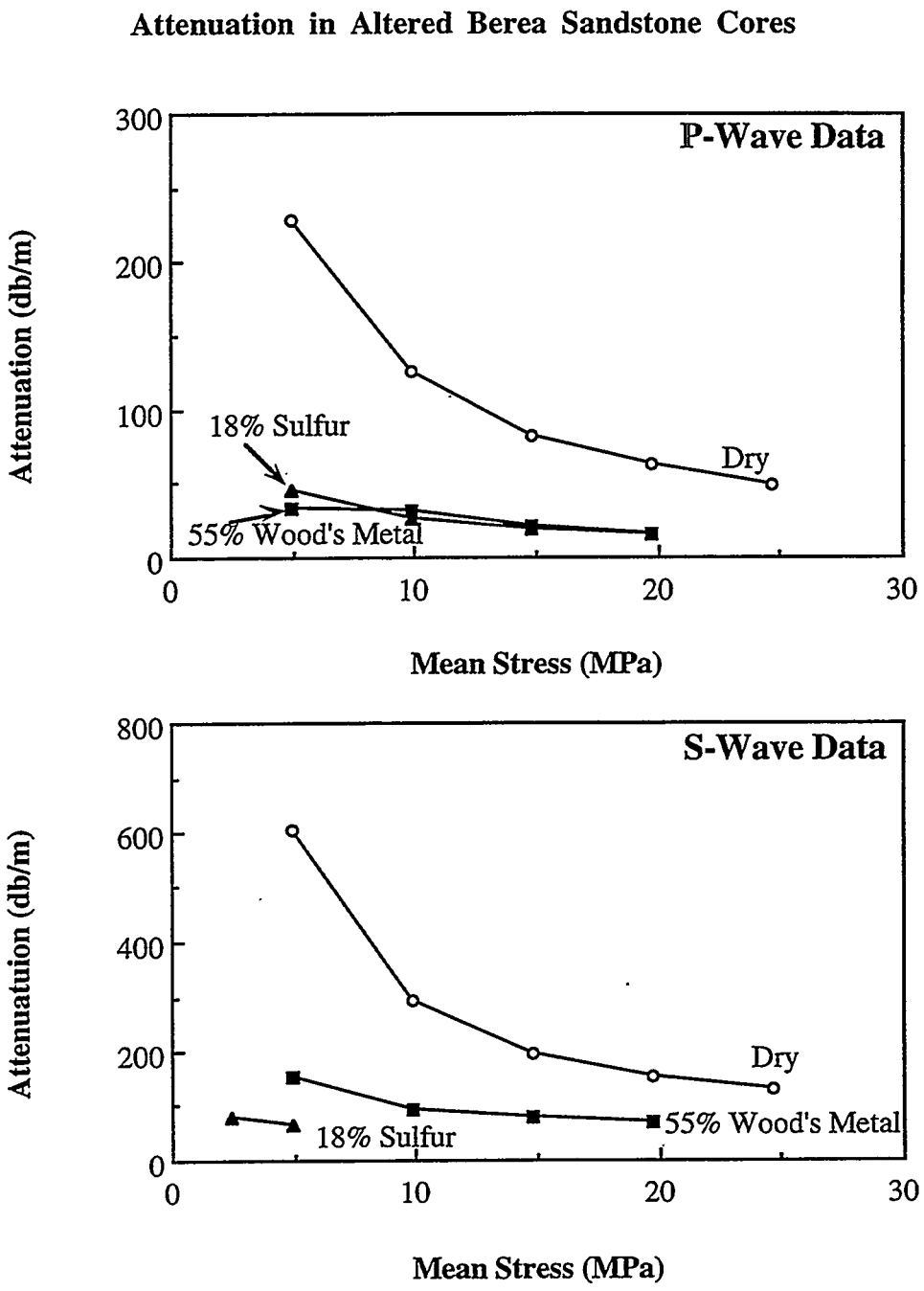

Figure 1.3: P-wave and S-wave attenuation coefficients for dry Berea Sandstone samples with and without isolated pore spaces. Sulfur solidified in the contacts; Wood's metal in the pores. Measurements were made under uniaxial stress. The attenuation coefficients were calculated for $f = 635$ kHz. From Nihei (1992).

Proposed Attenuation Mechanisms in Granular Media and Associated References

Bubble Resonance Frequency
Dutta and Odé (1979a), Dutta and Odé (1979b), Anderson and Hampton (1980a), Anderson and Hampton (1980b), Bedford and Stern (1983)

Crystal Imperfections/Dislocation Excitation
Mason et. al. (1970), Mason (1976), Karato and Spetzler (1990)

Global Fluid Flow (Biot Theory)
Biot (1956a), Biot (1956b), Biot (1962), Plona (1980), McCann and McCann (1985), Winkler (1985), Berryman (1988)

Grain Boundary Friction
Born (1941), Walsh (1966), Johnston et. al. (1979), Brennan (1981), Winkler and Nur (1982), Remy et. al. (1994)

Scattering Off Boundaries
Küster and Toksöz (1974a), Küster and Toksöz (1974b), Plona and Johnston (1981), Winkler (1983), Winkler and Murphy (1984), Blair (1990), Lucet and Zinszner (1992)

Squirt Fluid Flow
Mavko and Nur (1979), Palmer and Traviolia (1981), Bulau et. al. (1984), Dvorkin et. al. (1994), Mavko and Jizba (1994)

Surface Energy
Clark et. al. (1980), Tittman et. al. (1980), Spencer (1981), Bulau et. al. (1984), Murphy et. al. (1984), Parks (1984), Bourbie et. al. (1987),Tutuncu and Sharma (1992)

Thermo-Relaxation
Savage (1966), Kjartansson (1979), Armstrong (1980)

Viscous Relaxation
Walsh (1968), Walsh (1969), O'Connell and Budiansky (1977)

Table 1.3: Proposed mechanisms for seismic attenuation in granular media. Contacts contribute to the grain boundary friction, scattering, squirt fluid flow, and surface energy models.

and global fluid flow (Biot) models span the range of saturation states, from low to full saturations, respectively. Mechanical processes at grain contacts are important in five of these models: grain boundary friction, scattering, squirt fluid flow, surface energy, and viscous relaxation.

1.4.1 Scattering Attenuation

Attenuation in dry granular media is due to scattering losses. Reflections from heterogeneities remove energy from the direct seismic wave and redistribute this energy into scattered waves that appear in the coda (Nihei, 1992). In granular media, these heterogeneities can range in scale from pores, grain contacts, and microcracks to vugs, joints, fractures, faults, and sedimentary layers.

Scattering depends on the the product of the wavenumber, k, and the size of the scatterer, a for spherical particles. There are four types of scattering with different ka ranges, as shown in Figure 1.4. The wavenumber is inversely related to the wavelength. For spherical particles, the size of the scatterer is defined as the diameter. There is no direct, geometrical measurement of a for planar interfaces. Non-welded interfaces can produce signficant scattering losses despite having negligible thickness.

For wavelengths significantly larger than the scatterer size, $k <<< a$, scattering is described as point scattering. The scatterers can be any heterogeneity in material properties. Recent studies have suggested that these heterogeneities can be centimeter-scale density variations and grain clusters in addition to the millimeter-scale grains (Blair,1990; Lucet and Zinszner, 1992). It may be that the discontinuities are fractal and exist at all scales. At larger scales the discontinuities could include bedding variations and regional

Frequency-dependent Scattering in Rocks

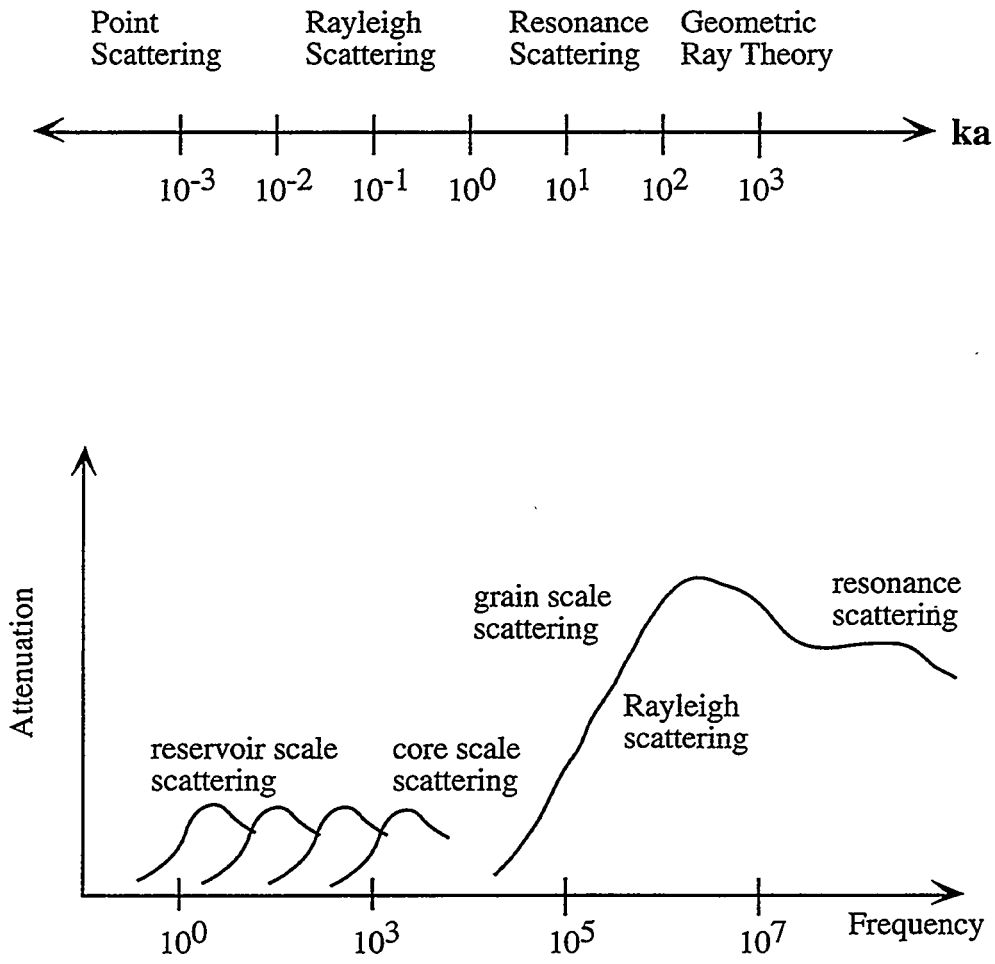

Figure 1.4: Frequency-dependent scattering in rocks. (a) The type of scattering is controlled by the product of the wavenumber k and size of scatterer a for spherical inclusions. (b) Scattering regimes in granular rocks.

faults. Existence of a fractal size distribution of scatterers would explain the frequency independent quality factor trend seen for a range of field and laboratory measurements.

Models have been developed to relate seismic velocities to scattering. These effective medium models idealize scatterers as isolated, interacting pores and cracks in a solid matrix (Kuster and Toksöz, 1974; O'Connell and Budiansky, 1974; Korringa *et. al.*, 1979; Toksöz and Cheng, 1980; Hudson, 1981; Crampin, 1984). By definition effective media theories are applied at zero frequency and therefore account only for viscous type attenuation and not scattering type attenuation.

Rayleigh scattering occurs as the wavelength λ approaches, but is still much larger than the size of the scatterer, $\lambda > a$. For spherical particles, Rayleigh scattering predicts a fourth order dependence between frequency (f) and attenuation (α), i.e. $\alpha = \chi f^4$ where χ is a constant. Laboratory studies on dry low porosity sandstones, fused glass bead samples, and unconsolidated glass bead samples have measured this fourth-order frequency dependence at ultrasonic frequencies (Winkler, 1983; Winkler and Murphy, 1984; Winkler, 1985). However, the measured attenuation magnitudes were an order of magnitude higher than predicted by a model developed by Sayers (1981) for spherical pores embedded in a matrix (Winkler, 1983). Winkler and Nur (1984) conclude that the pore/crack models are not applicable to granular media since "they do not consider the interaction between grains".

When the wavelength approaches the scatterer, i.e. $ka \approx 1$, the wave can become trapped and resonant in the scatterer. This strong scattering is known as Mie or resonance scattering. The direct wave is almost completely transformed into standing waves. Geometrical optics governs scattering when wavelengths are signficantly smaller than the

scatterer size. The last two situations are of little interest in seismic studies, since wavelengths of this order are rarely used to due thier large attenuations at high frequencies.

1.4.2 Squirt Fluid Flow Attenuation

Attenuation due to local fluid flow is called squirt flow. This mechanism is initiated by the wave propagation. The stresses of the propagating seismic wave generate high pressures in the fluids in cracks or near contacts. This induces pressure differentials in the pore fluid. The pore fluid flows in response to the pressure differential, as governed by Darcy's law, causing viscous losses in the material. The flow is expected to be between pores (interpore flow) in saturated granular media, and within pores (intracrack flow) in partially saturated media.

Fluid flow attenuation will be maximum at a particular frequency. When the pore space is modeled as a set of interconnected regular tubes, this critical frequency, f_c, is defined as (Johnston and Plona, 1982):

$$f_c = \frac{\eta_f}{\pi \rho_f b^2} \tag{1.1}$$

where η_f is the fluid viscosity, ρ_f the fluid density, and b the diameter of the tubes. This frequency corresponds to the onset of Poiseuille flow as shear stresses just couple across the tubes. It ranges from 1 to 10 kHz for a range of fluids (Bulau *et. al.* 1984).

Many different idealized geometries have been used to quantify squirt flow (O'Connell and Budiansky, 1977; Mavko and Nur, 1979; Palmer and Traviolia, 1980;

Murphy *et. al.*, 1984). Mavko and Nur (1979) developed an analytical solution for squirt flow attenuation in parrallel-walled pores. When $f>>f_c$,

$$\alpha_p = \frac{B_{local}}{c_p(f)}(\eta_f f)^{1/2} \qquad (1.2)$$

where B_{local} is a constant depending on fluid properties, pore geometry, and matrix shear modulus, η_f is fluid viscosity, and c_p the phase velocity. Attenuation is highly sensitive to aspect ratios of the pores, with the distribution of small aspect ratios dominating losses. Palmer and Traviolia (1980) formulated a solution for attenuation due to squirt flow in a simple cubic packing of elastic spheres in Hertzian contact. Packs of equal-size spheres resulted in negligible attenuation. When spheres ranged in diameter, the attenuation was sensitive to the aspect ratio of the near-contact pores.

Both the Mavko and Nur (1979) and Palmer and Traviolia (1980) squirt flow formulations have been found to underestimate attenuation by more than an order of magnitude. The concept, however, has been used to successfully interpret laboratory results (Spencer, 1981; Winkler and Nur, 1979; Murphy, 1982; Winkler, 1983; Winkler, 1985; Mavko and Jizba, 1991). Recent work by Tutuncu and Sharma (1992) has suggested that inclusion of fluid surface forces improves the estimation of attenuation. Also, Mavko and Jizba (1994) have proposed using dry rock properties as a base, instead of an idealized geometries. This has yielded good agreement for velocity dispersion.

1.4.3 Surface Energy Attenuation

Large attenuation decreases have been observed in rocks as small amounts of volatiles are added (Spencer, 1981; Tittman *et. al.*, 1980; Murphy, 1982; Bulau *et. al.*,

1984; Murphy *et. al.*, 1984; Tutuncu and Sharma, 1992). Studies have shown that chemical forces strongly affect rock strength at low water saturations (Parks, 1984; Lasaga, 1984; Dietrich and Conrad, 1984). This is attributed to physico-chemical interactions between the water and the mineral surfaces that lower the mineral surface energy. These same interations may affect seismic wave propagation.

When water is introduced into a granular material, it will preferentially saturate grain contacts and microcracks due to capillary suction. There it can have two effects on seismic wave propagation. First, its presence alone can affect the stiffness of these boundaries. Water can also interact with the grain surfaces. Minerals, such as quartz, have a sufficient negative charge to "ionize" the water film. Hydrogen bonds are formed between the mineral surface and the water film, decreasing the surface energy of the mineral. The extent of surface energy reduction by other fluids will depend on their polarity and activity. A decrease in surface energy decreases the stiffness of the contact.

Tittman *et. al.* (1980) investigated the effects of surface energy by studying attenuation as small amounts of volatiles were removed from sandstones. Boundary lubrication and water-assisted crack growth were rejected as possible mechanisms because the time frames needed are much longer than the seismic period. They found that a surface energy model based on thermally activiated motion of absorbed fluids explained their data. Attenuation was driven by both inertial and defomational forces. Interial forces involve the desorption and resorption of the volatiles as the stress wave propagates through the granular material. The propagating stress wave may also cause deformation by shear displacement and diffusion of the adsorbed fluid. The extent of attenuation was controlled by the bonding energies.

Similar effects were observed in sandstones, limestones, and granites by Spencer (1981). Murphy (1982) found that a combination of capillary and chemical effects qualitatively accounted for attenuation in Massilon sandstones and Vycor ® porous glass. Murphy *et. al.* (1984) compared the surface energy effects to elastic contact stiffness. They determined that surface energy effects will be most significant at tlow effective pressures.

1.4.4 Other Contact Attenuation Models

Grain boundary friction was one of the earliest proposed mechanisms for attenuation (Born, 1941). Coulomb friction is a well understood process: for a body on a flat surface, the frictional force is equal to the normal force times a coefficient of friction. A frictional attenuation model yields frequency independent attenuation, since friction does not depend on loading rate. However, later studies have identified two potential problems with the friction model. Savage (1966) found that for typical seismic strain amplitudes and reasonable microcrack dimensions, the computed slip at contacts was less than the interatomic spacing. Winkler *et. al.* (1979) invetigated friction both theoretically and experimentally and determined that frictional attenuation is significant only at strains above 10^{-6}, a value greater than the strains encountered in most seismological studies.

If the fluids in a crack have significant viscosity, they can resist applied stress. This resistance causes a viscous relaxation in the propagating seismic wave. O'Connell and Budiansky (1977) theoretically compared this mechanism to squirt flow and found that it will occur at frequencies four order of magnitude larger than squirt flow. Winkler and Nur (1982) estimate that viscous relaxation in rocks filled with water or light oils will occur at frequencies of 10^9 to 10^{12} hertz. This is significantly larger than typical frequencies in both field and laboratory measurements (10^0 to 10^7 hertz).

Because their ranges of significance are oustide normal parameters, grain boundary friction and viscous relaxation are not considered to be important attenuation mechanisms for seismic wave propagation in granular media.

1.4.5 Non-Contact Attenuation Models

Crystal dislocations have been shown to affect the acoustic behavior of polycrystalline minerals (Mason *et. al.*, 1970). Since granular materials are composed of grains of mineral crystals, it is possible that dislocations have an effect on wave propagation in granular materials. However, Bourbie *et. al.* (1987) have pointed out that the length of dislocations and the forces resisting dislocation require strains above 10^{-4} to have significant dislocation movement. This is beyond the range of most seismic and acoustic waves, which have strains below 10^{-6} (Winkler and Nur, 1982).

The thermo-relaxation model accounts for thermal dissipation during seismic propagation. Seismic waves apply stress to the material in a short time period, suggesting that the adiabatic properties will control the response. Each grain will respond in accordance with its particular properties, leading to temperature variations in the overall sample. These variations will attempt to equilibrate through thermal conduction, leading to a thermo-relaxation in the propagating seismic wave. Kjartansson (1979) found that this model can correctly predict the peak attenuation frequencies, but does not accurately represent attenuation variations with frequency or with saturation. Bourbie *et. al.* (1987) suggest that thermo-relaxation is likely to be negligible below temperatures of 100°C.

The remaining non-contact models have been widely applied. The global fluid flow model, also known as Biot theory, was derived for fully saturated granular materials. Attenuation is attributed to viscous losses caused by the "global" relative motion between a

compressible pore fluid and solid matrix. Attenuation can be calculated from the elastic constants, permeability, and porosity of the granular material. Burridge and Keller (1981) provided theoretical justification for the model by considering the microstructure of granular material. The model was shown to be robust by the detection of a predicted slow compressional wave (Berryman, 1980; Johnston andPlona, 1982; Klimentos and McCann, 1988). Many authors have proposed refinements to the basic model. Stoll and Bryan (1970) incorporated complex elastic moduli into the theory to include the frame losses. McCann and McCann (1985) removed the constraints on single pore size. By using a realistic distribution of pore sizes the model correctly predicted the variation of attenuation with frequency. Berryman (1988) found that the use of mean permeability, rather than the harmonic mean, correctly predicts the magnitude of seismic attenuation. Various forms of this model have been applied successfully to many results (Hovem, 1980; Ogushwitz, 1985; Winkler, 1985; Yamamoto and Turgut, 1988; Keller, 1989; Winkler *et. al.*, 1989; Klimentos and McCann, 1990; Mavko and Jizba, 1994). Biot model has been used to explain velocity data, but it typically underestimates attenuation (Mochizuki 1982).

The bubble resonance frequency attenuation model simulates granular materials at relatively high fluid saturations. The fluid phase must be continuous, with the gas phase discontinuous. Energy losses are due to the relative motion between the entrapped air bubbles and the pore fluid and solid matrix. By assuming that the acoustic wavelength is long with respect to the bubble size and distance between bubbles, and by assuming that the gas bubbles do not interact, Dutta and Odé (1979a) were able to generate corrections to Biot's model for gassy sediments. This model has been applied to marine sediments with good success (Dutta and Odé, 1979b; Anderson and Hampton, 1980b).

1.5 Dissertation Objectives

The primary objective of this research is to analyze the micromechanical effects of clay at grain contacts. A detailed study of clay at a controlled location can help to resolve some of the uncertainties over attenuation in granular materials. It may also have important practical applications in imaging the properties of poorly consolidated and unconsolidated sediments. Both experimental and numerical techniques will be used.

This chapter has reviewed recent studies on clay effects and attenuation mechanisms in granular materials. Seismic wave propagation has been empirically shown to depend on clay content, but no detailed work has been performed on the effect of clay location. Recent studies have also demonstrated the significant effects that grain contacts can have on seismic wave propagation. Scattering and squirt fluid flow attenuation models incorporate grain contact losses and have been shown to be relevant for a range of conditions. However, they do not account for clay at the contacts.

The theories of seismic wave propagation, contact stiffness, and clay swelling are given in Chapter 2. They provide the basis for the interpretation of the experimental results. Chapter 3 presents the laboratory procedures used in the experiments. Significant effort was invested to produce repeatable specimens, to insure comparability. Laboratory measurements of glass bead specimens with and without clay coatings are detailed in Chapter 4. Different fluid amounts and types are absorbed into the clay to analyze the importance of clay-fluid interactions. Two numerical analysis techniques are utilized in Chapter 5 to assess contact stiffness effects. Low pass filtering evaluates the general efficacy of non-welded contact models. Also, rheologic models and a boundary element technique together assess the proposed attenuation mechanism at clay-filled contacts.

Chapter 2: Theory of Seismic Wave Propagation, Interface Mechanics and Clay Swelling

2.1 Introduction

This chapter describes the theories that will be used throughout this dissertation. The theory of seismic wave propagation in an elastic, isotropic medium is presented. This provides an introduction to the parameters that will be measured and calculations that will be peformed in chapters 4 and 5. Models for discontinuous interfaces are also discussed. The contact stiffness models will be used to investigate the effects of stress in section 4.3. The rheologic models will be used as boundary conditions in the numerical modeling in chapter 5. Finally, a basic description of clay swelling is provided to aid the interpretation of the experimental results in section 4.5.

2.2 Theory of Seismic Wave Propagation in Elastic, Homogeneous, Isotropic Media

The theory of seismic wave propagation has been presented in detail by many authors (Aki and Richards, 1980; White, 1983; Bourbie *et. al.*, 1987). This summary follows the approach of White (1983). Seismic wave propagation in a homogeneous, isotropic media can be determined from stress-strain relationships and Newton's third law.

Consider stress on a cube, as shown in Figure 2.1. Only the stresses in the x direction are shown on this example. The cube has a mass equal to $\rho\Delta x\Delta y\Delta z$, where ρ is the density and $\Delta x\Delta y\Delta z$ is the unit volume. The tensor of stress can be related to strains through Hooke's Law, as follows:

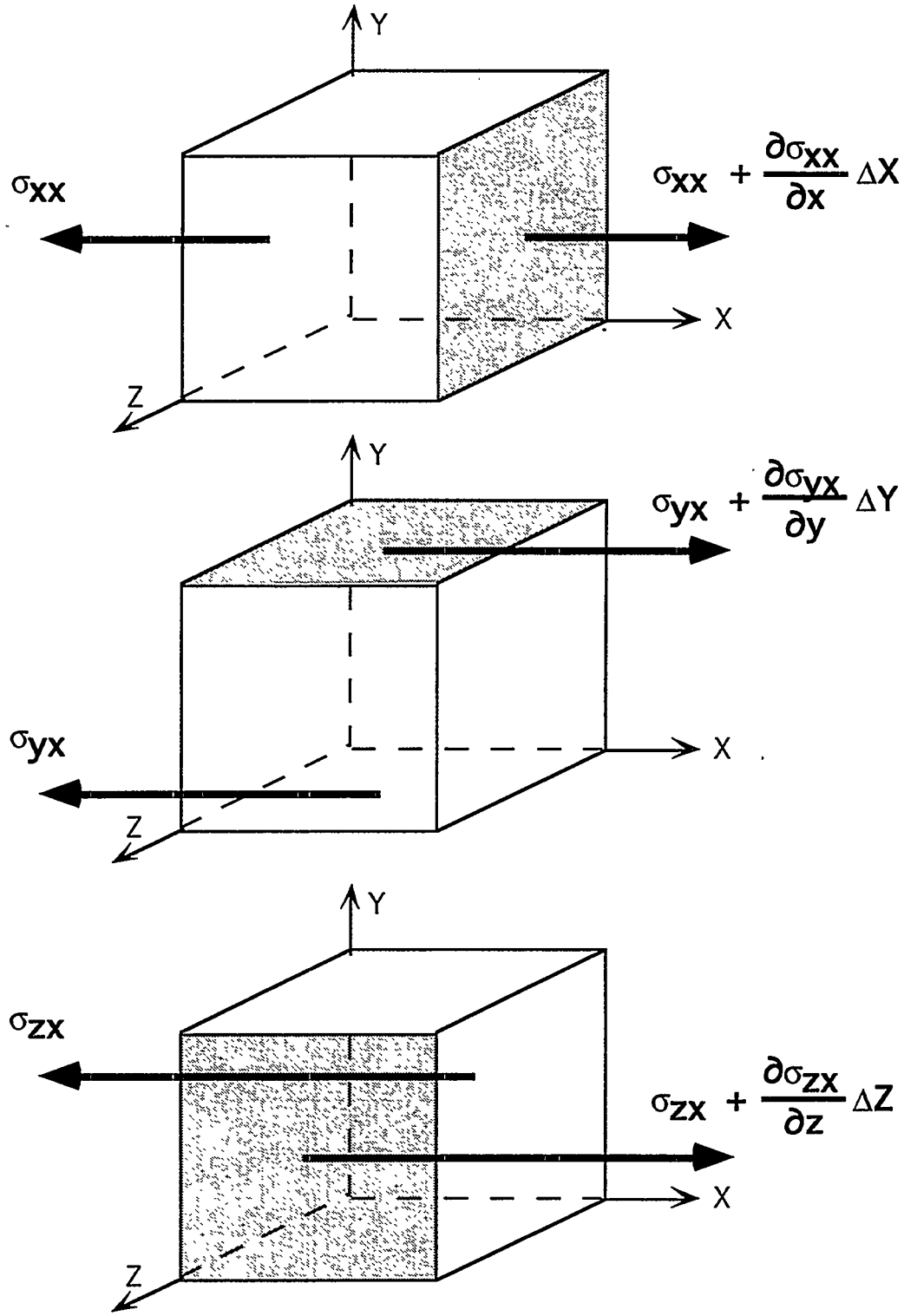

Figure 2.1: Surface stresses on a cube that are parallel to the x-axis. The forces are not drawn to scale.

$$\sigma_{xx} = (\lambda + 2\mu)\varepsilon_{xx} + \lambda\varepsilon_{yy} + \lambda\varepsilon_{zz}$$
$$\sigma_{yy} = \lambda\varepsilon_{xx} + (\lambda + 2\mu)\varepsilon_{yy} + \lambda\varepsilon_{zz} \qquad (2.1)$$
$$\sigma_{zz} = \lambda\varepsilon_{xx} + \lambda\varepsilon_{yy} + (\lambda + 2\mu)\varepsilon_{zz}$$

$$\sigma_{xy} = 2\mu\varepsilon_{xy} \qquad \sigma_{xz} = 2\mu\varepsilon_{xz} \qquad \sigma_{xz} = 2\mu\varepsilon_{xz} \qquad (2.2)$$

where σ is stress, are λ and μ the Lamé constants, and ε is the strain. When the stress is unbalanced, there will be a surface force as follows:

$$\left(\sigma_{xx} + \frac{\partial\sigma_{xx}}{\partial x}\Delta x - \sigma_{xx}\right)\Delta y\Delta z + \left(\sigma_{yy} + \frac{\partial\sigma_{yy}}{\partial y}\Delta y - \sigma_{yy}\right)\Delta x\Delta z + \left(\sigma_{zz} + \frac{\partial\sigma_{zz}}{\partial z}\Delta z - \sigma_{zz}\right)\Delta x\Delta y$$

$$= \left(\frac{\partial\sigma_{xx}}{\partial x} + \frac{\partial\sigma_{yy}}{\partial y} + \frac{\partial\sigma_{zz}}{\partial z}\right)\Delta x\Delta y\Delta z \qquad (2.3)$$

This force can be related to displacements through Newton's second law, force equals mass times acceleration:

$$F = ma = m\ddot{u} = (\rho\Delta x\Delta y\Delta z)\ddot{u} \qquad (2.4)$$

$$\frac{\partial\sigma_{xx}}{\partial x} + \frac{\partial\sigma_{xy}}{\partial y} + \frac{\partial\sigma_{xz}}{\partial z} + G_x = \rho\frac{\partial^2 u_x}{\partial t^2}$$
$$\frac{\partial\sigma_{yx}}{\partial x} + \frac{\partial\sigma_{yy}}{\partial y} + \frac{\partial\sigma_{yz}}{\partial z} + G_y = \rho\frac{\partial^2 u_y}{\partial t^2} \qquad (2.5)$$
$$\frac{\partial\sigma_{zx}}{\partial x} + \frac{\partial\sigma_{zy}}{\partial y} + \frac{\partial\sigma_{zz}}{\partial z} + G_z = \rho\frac{\partial^2 u_z}{\partial t^2}$$

where G_i are any unit volume body forces within the cube. This equation (2.5) is called the equation of motion. Body forces are typically negligible in seismic wave propagation,

so for the remainder of this discussion they will be set equal to zero. The strains are the gradients of the displacements:

$$\varepsilon_{ij} = \tfrac{1}{2}\left(\frac{\partial u_i}{\partial x_j} + \frac{\partial u_j}{\partial x_i}\right) \tag{2.6}$$

This allows the stresses to be removed from equation 2.5 by differentiating equations 2.1 and 2.2 and then substituting the results into equation 2.5:

$$\begin{aligned}
&(\lambda+2\mu)\frac{\partial^2 u_x}{\partial x^2} + \mu\left(\frac{\partial^2 u_y}{\partial y^2} + \frac{\partial^2 u_z}{\partial z^2}\right) + (\lambda+2\mu)\left(\frac{\partial^2 u_y}{\partial x \partial y} + \frac{\partial^2 u_z}{\partial x \partial z}\right) = \rho\frac{\partial^2 u_x}{\partial t^2} \\
&(\lambda+2\mu)\frac{\partial^2 u_y}{\partial y^2} + \mu\left(\frac{\partial^2 u_x}{\partial x^2} + \frac{\partial^2 u_z}{\partial z^2}\right) + (\lambda+2\mu)\left(\frac{\partial^2 u_x}{\partial x \partial y} + \frac{\partial^2 u_z}{\partial y \partial z}\right) = \rho\frac{\partial^2 u_y}{\partial t^2} \\
&(\lambda+2\mu)\frac{\partial^2 u_z}{\partial z^2} + \mu\left(\frac{\partial^2 u_x}{\partial x^2} + \frac{\partial^2 u_y}{\partial y^2}\right) + (\lambda+2\mu)\left(\frac{\partial^2 u_x}{\partial x \partial z} + \frac{\partial^2 u_y}{\partial y \partial z}\right) = \rho\frac{\partial^2 u_z}{\partial t^2}
\end{aligned} \tag{2.7}$$

This equation (2.7) is known as the equation of motion for a homogeneous , isotropic, elastic solid. Aki and Richards (1980) substitute the solution form $\mathbf{u} = \mathbf{u}(t - \mathbf{s}\bullet\mathbf{x})$, where $\mathbf{s}$ is the slowness vector, into the above equations and rearrange to obtain two decoupled wave equations:

$$\begin{aligned}
&\left(\rho - \mu s^2\right)\ddot{\mathbf{u}} \times \mathbf{s} = 0 \\
&\left(\rho - (\lambda+2\mu)s^2\right)\ddot{\mathbf{u}} \bullet \mathbf{s} = 0
\end{aligned} \tag{2.8}$$

The two basic types of elastic waves are easily derived from this formulation. Either $\ddot{\mathbf{u}} \times \mathbf{s} = 0$, producing a compressional or P-wave in the direction of propagation, or $\ddot{\mathbf{u}} \bullet \mathbf{s} = 0$, produing a shear or S-wave transverse to the direction of propagation. Since the

slowness vector is the inverse of the velocity vector **c**, or in scalar terms: $s^2=1/c^2$. Substituting this into the equation 2.8 gives the wave velocities respectively as:

$$c_p = \sqrt{\frac{(\lambda+2\mu)}{\rho}} = \sqrt{\frac{B+\frac{4}{3}\mu}{\rho}}$$
$$c_s = \sqrt{\frac{\mu}{\rho}} \qquad (2.9)$$

where c is the wave velocity, B is the bulk modulus, and μ is the shear modulus.

The general solution for the elastic displacement equations (equations 2.7) for a monochromatic wave of frequency, *f*, is:

$$u(f,\mathbf{x}) = u_0 e^{i(\mathbf{k}\bullet\mathbf{x}-2\pi ft)} \qquad (2.10)$$

where u_0 is the initial amplitude, **k** is the wavenumber vector, and **x** is the location vector. In an attenuating medium with a wave traveling in one direction *x*, equation 2.10 can be written as:

$$u(f,x) = u_0 e^{\left(-\frac{2\pi fx}{Qc}\right)} \qquad (2.11)$$

where Q is the quality factor, and c the wave speed. The quality factor is a measure of energy loss per wavecycle. It serves as a useful standardized measure for comparison between experiments.

2.3 Interface Effects on Seismic Wave Propagation

Seismic wave propagation in purely elastic media provides a basis for understanding wave propagation in microscopically heterogeneous but macroscopically homogeneous media, such as porous rocks. This study is concerned with the processes that occur at granular contacts during the propagation of seismic waves. Each of the following models are one step more refined than the previous model. As a first approximation, the granular contacts can be considered to be planar interfaces. The contact stiffness models approximate a cubic packing of spherical grains. The granular contacts occur in the same plane, but have finite contact area. The discontinuous interface models approximate the mechanical properties of grain contacts with springs and dashpots that represent the specific stiffness and specific viscosity.

2.3.1 Contact Stiffness Models

Three different contact stiffness models are presented here. They are presented in order of increasing complexity. Contact stiffness models assume that the seismic wavelength is much longer than the interface. Therefore, the interface thickness can be neglected and the frequency equals zero. Two of the models use velocities to calculate the contact stiffnesses; one model uses the mean stress.

2.3.1.1 Effective Modulus Contact Stiffness Model

The first contact stiffness model is based on the effective modulus equation, a zero frequency of long-wavelength approximation. Consider the volume of beads. In the cubic packing, the granular contacts can be represented as a set of n planar, non-interacting interfaces, each having the same stiffness K, as shown in Figure 2.2. The strain energy

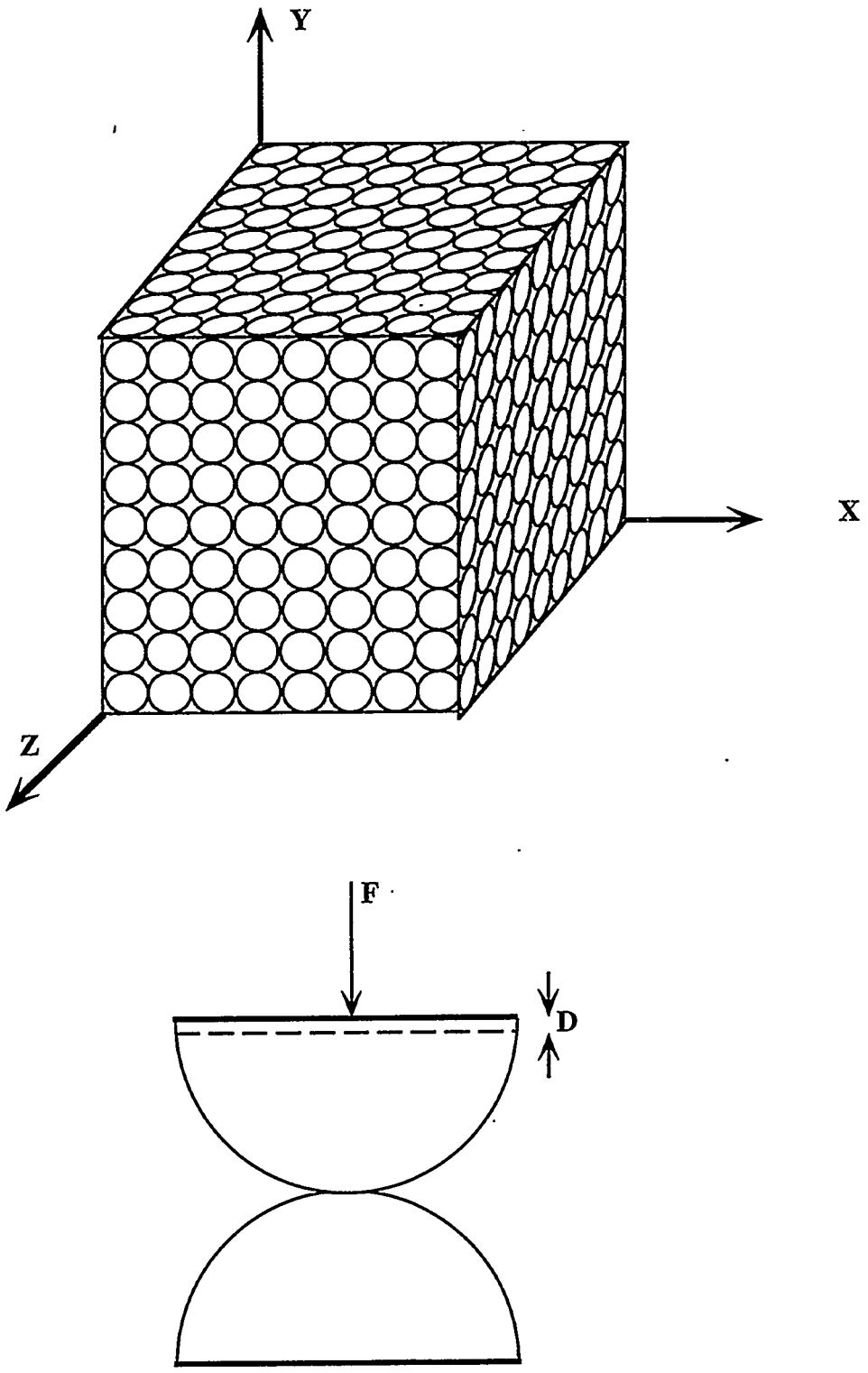

Figure 2.2: (a) A cubic packed volume of beads. (b) An individual bead contact.

for the specimen has been derived by many authors (Jaeger and Cook, 1969; Pyrak-Nolte *et. al.*, 1987):

$$\frac{\sigma^2}{2E'} = \frac{\sigma^2}{2E} + \frac{n\sigma^2}{2K} \tag{2.12}$$

where σ is the stress, E' the effective modulus, and E the solid modulus. Reduction of this equation, by removal of like terms, gives the Reuss effective modulus equation:

$$\frac{1}{E'} = \frac{1}{E} + \frac{n}{K} \tag{2.13}$$

Rearranging to isolate the stiffness produces:

$$K = \frac{nE'E}{E - E'} \tag{2.14}$$

This equation can be put into terms of measurable parameters by substituting for E' and n. A generalized form of equation 2.9 can be used to replace the effective modulus E' with density ρ, porosity ϕ, and velocity c as follows:

$$c = \sqrt{\frac{E'}{\rho'}} \quad \Rightarrow \quad E' = \rho' c^2 \qquad E' = \rho(1-\phi)c^2 \tag{2.15}$$

where ρ' is the effective density. For plane waves, E' is the uniaxial strain modulus. The number of interfaces can be replaced by the diameter of the grains by considering a unit-length column of grains. The number of interfaces in this column is inversely related to the diameter of the grains or twice the radius:

$$n = \frac{1}{\text{diameter}} = \frac{1}{2R} \tag{2.16}$$

Substituting equations 2.15 and 2.16 into 2.14 gives:

$$K = \frac{\rho(1-\phi)c^2 E}{2R\left[E - \rho(1-\phi)c^2\right]} \tag{2.17}$$

Equation 2.17 expresses the incremental stiffness per planar interface. To change this into a grain-to-grain incremental contact stiffness assume that each grain occupies a square area with side equal to the grain diameter. The number of contacts per plane is the inverse of contact area, and the individual contact stiffness is equal to the planar stiffness divided by the number of contacts per plane:

$$K_c = \frac{K}{1/(2R)^2} = \frac{2R\rho(1-\phi)c^2 E}{\left[E - \rho(1-\phi)c^2\right]} \tag{2.18}$$

2.3.1.2 Hertzian Contact Stiffness

The second contact stiffness model focuses on the individual grain-to-grain contacts. Hertz theory estimates the elastic behavior of spherical particles in contact under normal loads. The theory accounts for changes in contact area upon loading. The relationship between force and displacement for Hertz contacts is non-linear, as shown in Figure 2.3. However, the stress in a seismic wave is small and can, therefore, be approximated as a small linear increment. The relevant contact stiffness for a Hertz contact then becomes the tangent to the force-displacement curve. The incremental stiffness of spherical contacts has been calculated by White (1983) as:

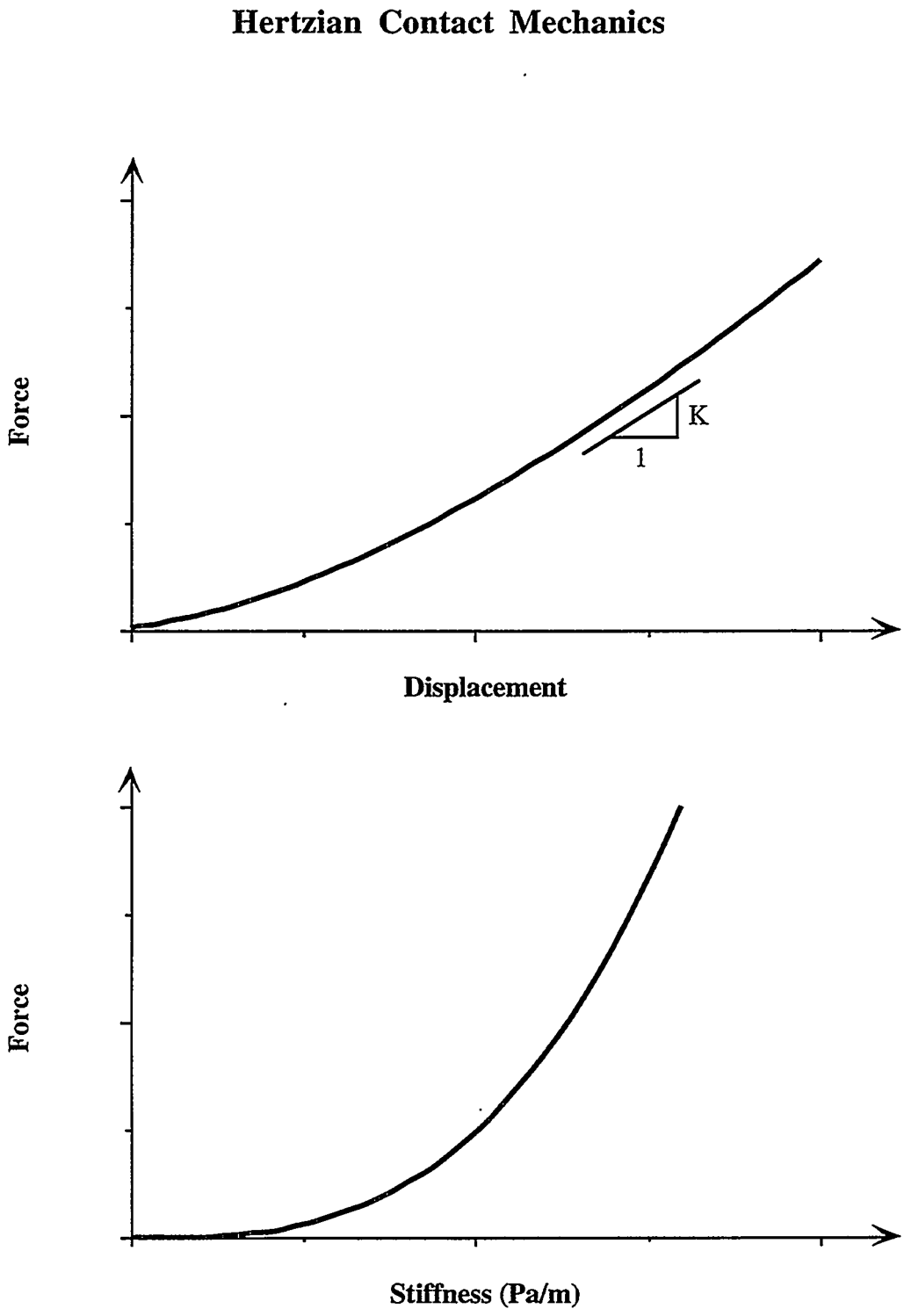

Figure 2.3: (a) Force versus displacement and (b) force versus stiffness for a Hertzian contact where spheres are in point-to-point contact.

$$K_c = \left[\frac{3E^2RF}{4\left(1-\nu^2\right)^2} \right]^{1/3} \tag{2.19}$$

where F is the normal force and ν the Poisson's ratio of the solid spheres. This force can be changed into a stress by considering a column of spheres. Given a mean hydrostatic stress σ on the column, the force is related to this mean stress by:

$$F = 4R^2\sigma \tag{2.20}$$

By substitution into equation 2.19, the contact stiffness equation becomes:

$$K_c = \left[\frac{3E^2R\left(4R^2\sigma\right)}{4\left(1-\nu^2\right)^2} \right]^{1/3} = \left[\frac{3E^2\sigma}{\left(1-\nu^2\right)^2} \right]^{1/3} \cdot R \tag{2.21}$$

This formulation ignores tangential forces on the spheres (Wang and Nur, 1992).

2.3.1.3 Modified Effective Modulus Contact Stiffness

The final contact model modifies the effective modulus to account for random spherical particle contacts. This first requires the calculation of the incremental strain energy per contact associated with the propagation of small amplitude sesimic waves in a medium under static stress. The strain energy is the work done by the applied force F when displacing the material by an amount D. The incremental relationship is linear and governed by the incremental (tangent) contact stiffness. Therefore, the strain energy per contact SE_C is equal to:

$$SE_c = \frac{FD}{2} = \frac{F^2}{2K_c} \tag{2.22}$$

since for elastic contacts the contact stiffness K_C is defined as the incremental force divided by the displacement. Stress can be substituted for the force by a careful consideration of the applied area. Force that is transmitted to the point contact is applied over an area πR^2. However, over any planar area in the sample that bisects the beads, only $(1-\phi)$ area is bead surfaces. Therefore:

$$F = \sigma \bullet A = \sigma \bullet \frac{\pi R^2}{1-\phi} \tag{2.23}$$

where A is the area over which the stress is applied. Substituting into equation 2.22 gives:

$$SE_c = \frac{F^2}{2K_c} = \frac{1}{2K_c}\left[\frac{\sigma \pi R^2}{1-\phi}\right]^2 = \frac{\pi^2 R^4 \sigma^2}{2K_c(1-\phi)^2} \tag{2.24}$$

This equation gives the incremental strain energy per contact. The overall strain energy SE is equal to the product of the strain energy per contact SE_C times the effective number of contacts N_e as follows:

$$SE = SE_c \bullet N_e = \frac{N_e \pi^2 R^4 \sigma^2}{2K_c(1-\phi)^2} \tag{2.25}$$

When this equation (2.25) is substituted into the strain energy equation (2.12) and then reduced, the modified effective modulus equation is produced:

$$\frac{\sigma^2}{2E'} = \frac{\sigma^2}{2E} + SE = \frac{\sigma^2}{2E} + \frac{N_e \pi^2 R^4 \sigma^2}{2K_c(1-\phi)^2}$$
$$\frac{1}{E'} = \frac{1}{E} + \frac{N_e \pi^2 R^4}{K_c(1-\phi)^2} \qquad (2.26)$$

The effective number of contacts can be determined by first considering the number of particles in a unit volume. The number of particles N_p can be found by dividing the solid volume V_S by the volume per particle V_p. For a unit volume:

$$N_p = \frac{V_S}{V_p} = \frac{(1-\phi)}{\frac{4}{3}\pi R^3} \qquad (2.27)$$

The number of contacts per particle is related to the coordination number C. Table 2.1 presents coordination numbers for a range of spherical grain packings. Since each of these contacts is associated with another particle, only half can be assigned to a single particle. Also, not all contacts are equally involved in seismic displacements. Under uniaxial strain, only ~1/3 of the number of contacts undergo displacement N_d. Thus the effective number of contacts can be estimated as:

$$N_e = N_p \bullet \tfrac{1}{2} C \bullet N_d = \frac{(1-\phi)}{\frac{4}{3}\pi R^3} \bullet \tfrac{1}{2} C \bullet \frac{1}{3} = \frac{(1-\phi)C}{8\pi R^3} \qquad (2.28)$$

Substituting this into 2.26 gives:

$$\frac{1}{E'} = \frac{1}{E} + \frac{N_e \pi^2 R^4}{K_c(1-\phi)^2} = \frac{1}{E} + \frac{\pi^2 R^4}{K_c(1-\phi)^2} \bullet \frac{(1-\phi)C}{8\pi R^3} = \frac{1}{E} + \frac{\pi R C}{8(1-\phi)K_c} \qquad (2.29)$$

Packing Type	Pore Structure	Porosity (%)	Coordination Number
Cubic	cubic void	47.6	6
Simple Hexagonal	Simple rhombus void	39.6	8
Compact Hexagonal	Tetrahedral void	25.9	12
Random	varied	~36	~9

Table 2.1: Characteristics of different types of packings of spherical particles. Based on Bourbie *et. al.* (1987).

Rearranging 2.29 to solve for K_C yields:

$$K_c = \frac{\pi RC}{8(1-\phi)} \bullet \frac{E'E}{E-E'} \tag{2.30}$$

For uniaxial strain, the P-wave velocity can be used to calculate the effective modulus. Replacing E' with equation 2.15 gives K_C into directly measurable parameters:

$$K_c = \frac{\pi RC}{8(1-\phi)} \bullet \frac{E'E}{E-E'} = \frac{\pi RC}{8(1-\phi)} \bullet \frac{\left[\rho(1-\phi){c_p}^2\right]E}{E-\left[\rho(1-\phi){c_p}^2\right]} = \frac{\pi RC\rho{c_p}^2 E}{8\left(E-\rho(1-\phi){c_p}^2\right)} \tag{2.31}$$

For triaxial strain, the bulk modulus B can be used to find the incremental interface stiffness. All the contacts are involved, thus:

$$\begin{aligned} N_e &= N_p \bullet \tfrac{1}{2}C \bullet N_d = \frac{(1-\phi)}{\frac{4}{3}\pi R^3} \bullet \tfrac{1}{2}C \bullet 1 = \frac{3(1-\phi)C}{8\pi R^3} \\ \frac{1}{B'} &= \frac{1}{B} + \frac{N_e \pi^2 R^4}{K_c(1-\phi)^2} = \frac{1}{B} + \frac{\pi^2 R^4}{K_c(1-\phi)^2} \bullet \frac{3(1-\phi)C}{8\pi R^3} = \frac{1}{B} + \frac{3\pi RC}{8(1-\phi)K_c} \end{aligned} \tag{2.32}$$

The effective bulk modulus B' can be found from:

$$B' = \rho\left({c_p}^2 - \tfrac{4}{3}{c_s}^2\right) \tag{2.33}$$

Rearranging equation 2.32 and then substituting in into equation 2.33 gives:

$$K_c = \frac{3\pi RC}{8(1-\phi)} \bullet \frac{B'B}{B-B'} = \frac{3\pi RC}{8(1-\phi)} \bullet \frac{\left[\rho\left({c_p}^2 - \frac{4}{3}{c_s}^2\right)\right]B}{B-\left[\rho\left({c_p}^2 - \frac{4}{3}{c_s}^2\right)\right]} \tag{2.34}$$

2.3.1.4 Contact Models Application

Equations 2.18, 2.21, 2.31, and 2.34 will be used in section 4.3 to estimate the effect of stress on contact properties. The seismic velocities measured in the laboratory for the various specimens will be used to calculate the contact stiffnesses.

2.3.2 Discontinuous Interface Models

Discontinuous interface models account for attenuation losses at interfaces in addition to elasticity effects. There are two primary interface models: discontinuous displacement and discontinuous velocity. These can be combined in through a variety of rheologic models. The following sections detail each discontinuity and discuss their combination.

2.3.2.1 Discontinuous Displacement Interfaces

A displacement discontinuity interface occurs when an interface is more compliant than the matrix. This introduces a constant difference in the displacements on the two sides of the interface. Under these conditions, the interface is often termed an elastic non-welded interface. Figure 2.4 presents a model of such an interface. Schoenberg (1980) presented a formal relationship between the discontinuous displacement and interface properties:

$$\begin{aligned} u_2 - u_1 &= \frac{1}{K_{sp}}\sigma \\ \sigma_2 &= \sigma_1 \end{aligned} \qquad (2.35)$$

where u is the displacement, K_{sp} is the specific stiffness, and σ is the applied stress. Subscripts 1 and 2 refer to above and below the interface respectively. These relationships are

Displacement Discontinuity

$$K_{sp}(u_2 - u_1) = \sigma$$
$$\sigma_1 = \sigma_2$$

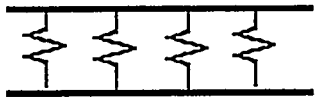

Hooke Model
$K_r = K_{sp}$, $K_i = 0$

Velocity Discontinuity

$$\eta_{sp}\left(\frac{\partial u_1}{\partial t} - \frac{\partial u_2}{\partial t}\right) = \sigma$$
$$\sigma_1 = \sigma_2$$

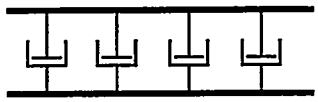

Newton Model
$K_r = 0$, $K_i = \eta_{sp}$

Displacement and Velocity Discontinuity

$$K_{sp}(u_2 - u_1) + \eta_{sp}\left(\frac{\partial u_1}{\partial t} - \frac{\partial u_2}{\partial t}\right) = \sigma$$
$$\sigma_1 = \sigma_2$$

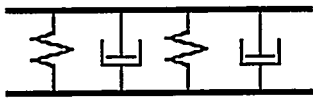

Kelvin-Voight Model
$K_r = K_{sp}$, $K_i = \eta_{sp}$

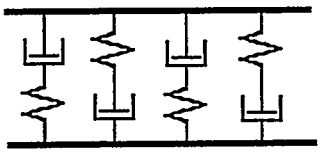

Maxwell Model

$$K_r = \frac{K_{sp}(2\pi f)^2\eta_{sp}^2}{K_{sp}^2 + (2\pi f)^2\eta_{sp}^2}$$

$$K_i = \frac{K^2(2\pi f)\eta}{K_{sp}^2 + (2\pi f)^2\eta_{sp}^2}$$

Figure 2.4: Discontinuity models, associated mechanical (spring and dashpot) descriptions, and associated rheological models.

the limiting case of an interface layer between two substrates. Rohklin and Wang (1991) have shown that for thin layers, where the wavenumber-layer thickness product is much less than one, the general interface equations reduce to equation 2.35. The relationships are assumed to hold at all frequencies, though the specific stiffness may vary with frequency. Pyrak-Nolte et al (1987, 1990) have shown that these conditions act as a low pass filter and introduce a group time delay into the displacement propagation. The time delay depends on both the ratio of specific stiffness to matrix impedance and the frequency. At zero frequency the group time delay results in a group velocity that coincides with that given by the effective modulus solution.

A displacement discontinuity can be modeled by the Hooke rheologic model (Sperry, 1964). The interface region is represented as a spring, with the spring constant equal to the specific stiffness, as shown in Figure 2.4. The springs may be normal or transverse to the interface, depending on the wave motion. Angel and Achenbach (1985) have verified the model by comparing theoretical and model transmission and reflection coefficients for an array of equally spaced coplanar cracks. The coefficients were similar when the wavelength was much larger than the crack spacing. Models of welds and bonds have used the discontinuous displacement model with good agreement (Rohklin and Wang, 1991b). Laboratory studies on single interfaces have proven the validity of this model for seismic wave propagation in rock. Pyrak-Nolte et al. (1990) measured compressional propagation across a single natural fracture in granite and found that a displacement discontinuity model accurately captured the changes in spectral amplitude.

2.3.2.2 Discontinuous Velocity Interfaces

A velocity discontinuity arises when a thin, viscous liquid fills an interface. The fluid can support shear wave propagation due to its viscosity. However, energy is

dissipated. This has been referred to as both a viscous and a slip interface (Suárez-Rivera, 1992; Schoenberg, 1980; Pyrak-Nolte *et. al.*, 1990). Figure 2.4 presents a schematic diagram of these interfaces. The formal relationships were given by Pyrak-Nolte (1987):

$$\begin{aligned} (\dot{u}_2 - \dot{u}_1) &= \frac{1}{\eta_{sp}}\sigma \\ \sigma_2 &= \sigma_1 \end{aligned} \tag{2.36}$$

where η_{sp} is the specific viscosity. When the wavelength is much greater than the thickness of the interface, the wave propagates through the interface without group time delay. Pyrak-Nolte et al (1990) note that a viscous interface acts as a frequency-independent attenuator and does not produce a group time delay.

For a viscous interface, the contact mechanics can be represented by the Newton model, where the interfaces are coupled by a dashpot with viscosity equal to the specific viscosity. It has been used to simulate experiments on shear wave transmission through liquid films. Polar liquids were well matched by the theory (Suárez-Rivera, 1992).

2.3.2.3 Discontinuous Displacement and Discontinuous Velocity Interfaces

Interfaces may be a combination of both the discontinuous displacement and discontinuous velocity interfaces. These interfaces may be termed visco-elastic interfaces, and are shown in Figure 2.4. Formal equations for this model have been presented by Pyrak-Nolte (1990), where the specific stiffness and specific viscosity have moved to the left-hand side of the equation:

$$\begin{aligned} K_{sp}(u_2 - u_1) + \eta_{sp}(\dot{u}_2 - \dot{u}_1) &= \sigma \\ \sigma_2 &= \sigma_1 \end{aligned} \tag{2.37}$$

The combined discontinuity interface can be modeled as a combination of springs and dashpots. By taking the derivative of the seismic displacement equation (2.10), it is evident that equations 2.36 can be satisfied by allowing the interface stiffness to become complex:

$$\dot{u} = i2\pi f \bullet \left(u_o e^{i(\mathbf{k} \bullet \mathbf{x} - 2\pi f t)} \right)$$
$$K = K_r + i2\pi f K_i \tag{2.38}$$

where K_r is the real stiffness and K_i is the imaginary stiffness. A variety of rheologic models can be used to calculate the complex stiffness from the specific stiffness and specific viscosity (Sperry, 1964). The two most common are the Kelvin-Voight and Maxwell rheologies as shown in Figure 2.4. For a Kelvin-Voight representation, the real modulus is equivalent to specific stiffness and the complex modulus is equivalent to specific viscosity. Suárez-Rivera (1992) noted that a Maxwell formulation for complex stiffness will be dominated by the most compliant parameter. Thus, the model will predict elastic behavior when the specific viscosity is large. The Kelvin-Voight formulation will predict elastic behavior when the specific viscosity is small.

The combined discontinuous displacement and discontinuous velocity model has been applied to laboratory shear wave experiments with good agreement. Pyrak-Nolte (1990) found that shear waves normal to a dry and saturated natural fracture in a granite were well modeled by the combined discontinuity model. The model also correctly predicted the amplitudes and frequency shifts for shear wave transmission and reflection on a clay-coated planar fracture with a variety of absorbed fluid types and amounts (Suárez-Rivera, 1992).

2.3.2.4 Attenuation in Discontinuity Models

The discontinuous displacement, discontinuous velocity, and combined discontinuity models all can be used to determine the attenuation through the derivation of analytical expressions for transmission coefficients, T(f). For waves at normal incidence to the interface, the discontinuous displacement and discontinuous velocity models coefficients are (Pyrak-Nolte *et. al.*, 1987; Suárez-Rivera, 1992):

$$T(f)=\left[\frac{1}{1+(\pi f)^2\left(\frac{K_{sp}}{Z}\right)^2}\right]^{1/2}$$
$$T(f)=\left[\frac{1}{1+(\pi f)^2\left(Z\eta_{sp}\right)^2}\right]^{1/2} \qquad (2.39)$$

respectively. For combined displacement and velocity discontinuous interfaces, the coefficients will depend on the rheologic model chosen for the interface (see Suárez-Rivera, 1992). Once these coefficients are calculated for single interfaces, the effects of multiple interfaces can be found by multiplying the appropriate transmission and reflection parameters. To simplify the calculations multiple reflections are frequently neglected. If all n interfaces are identical, then the transmitted signal is simply the initial signal multiplied by the transmission coefficient to the power n.

2.3.3 Summary of Interface Models

The effective modulus models are zero frequency, long-wavelength approximations that account for the changes in elastic moduli due to an interface. The effective moduli can be calculated from contact stiffnesses. The incremental contact stiffness determines the

seismic velocity. The total stiffness gives changes in velocity with confining stress. Discontinuous interface models are equivalent to effective moduli models at zero frequency, but can account for attenuation due to both scattering and dissipation at finite frequencies.

2.4 Clay Swelling Mechanisms

Clay swelling is the change in mixture volume as clay absorbs fluid. It is a very complicated thermodynamic process that requires calculation of the Gibb's free energy of the system and the osmotic swelling pressures (Mitchell, 1991; Sposito, 1984; van Olphen, 1977). This section is intended only to review this process. A detailed description can be found in van Olphen (1977).

Clay swelling results from the structural and chemical properties of clays. The structure of montmorillonite, a clay that experiences significant swelling, is shown in Figure 2.5. The tetrahedryl shapes are composed of silicon trioxide joined into a tetraheydral shape. When silicon trioxide joins with with aluminum or magnesium cations, it forms an octrahedral shape as shown by the squares. The particular basic tetraheydral-octaheydral-tetraheydral unit of montmorillonite is termed a 2:1 mineral structure.

During formation of clays, there are typically not enough of the proper cations nearby to form the ideal structures. Other cations are substituted in a process termed isomorphous substitution. This leads to a negative charge at the particle surface. The charge imbalance is satisfied by a number of methods, including hydroxyl-oxygen bonding, hydrogen bonds with water, and cation attraction. For montmorillonite, water and cations bond to the negative particle surfaces. These form weak, inter-layer bonds.

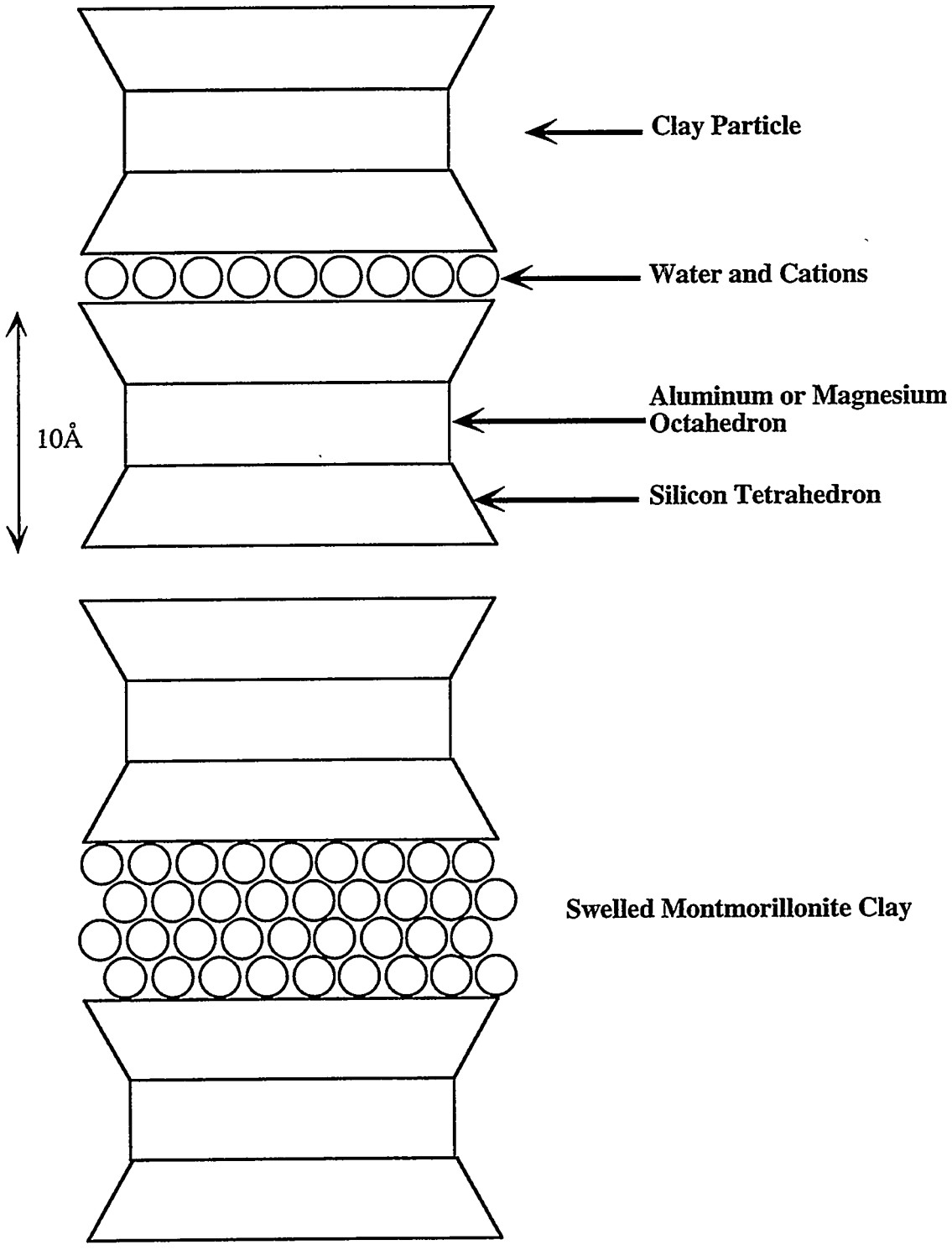

Figure 2.5: Montmorillonite clay particles in the dry and swelled state.

Two ranges of swelling have been identified. The first stage is due to short-range particle interactions, sometimes termed intracrystalline swelling. As water is initially absorbed into the clay, it moves into the inter-layer bonding region where it hydrogen bonds with the particle surface. This decreases the surface hydration energy. Because of the weakness of the inital inter-layer bonds for montmorillonite, significant monolayers can be incorporated into this inter-layer region. Each successive monolayer increases the distance between the clay particles, causing an increase in mixture volume.

The second stage is due to long-range particle interactions, termed either osmotic swelling or electrical double-layer repulsion. These become important after adsoprtion of approximately four monomolecular layers, where surface hydration energy has significantly decreased and a true water layer forms. The cations previously bonded to the particle surfaces try to diffuse through the water layer to equalize the concentration. This leads to a distribution of charge, that decays in an exponential function from one surface. Interaction between the the charge distributions from two adjacent surfaces, such as the clay particles, is called a double-layer. This is mathematically described in the Guoy-Chapman theory for a diffuse double layer as:

$$\frac{1}{K_{DL}} = \sqrt{\frac{\varepsilon_o D_c k_B T}{2 n_o e^2 v^2}} \tag{2.40}$$

where $1/K_{DL}$ is the thickness of the double layer, ε_O the static permittivity of a vacuum, D_c the dielectric constant of the medium, k_B the Boltzmann constant, T the temperature, n_O the cation concentration, e the electronic charge, and v the cation valence. An increase in the double layer thickness increases the volume of the mixture. Thus, any variations in dielectic constant, temperature, cation concentration, or cation valence may increase the clay swelling.

Chapter 3.0 Experimental Procedures

3.1 Introduction

Research has shown that seismic wave propagation in granular material is a function of density (Geertsma, 1961), grain size (Prasad and Meissner, 1992), compaction (Murphy, 1982a), clay content (Han *et. al.*, 1988), cementation (Dvorkin *et. al.*, 1991), pore fluid saturation (Domenico, 1974), and pore fluid type (Tittman *et. al.*, 1980). These properties can vary in unconsolidated glass bead specimens. Therefore, precise control was required during sample fabrication to ensure reproducibility. Sample preparation methods were carefully designed to generate a standard base. The following chapter details the experimental methods used in the laboratory investigation. Results from tests to check the procedures are also presented.

3.2 Sample Preparation

3.2.1 Sample Matrix

Soda-lime glass beads were chosen for the matrix material. The beads were inspected under an optical microscope and found to be primarily spherical in shape (Figure 3.1a). Therefore, the grain-to-grain contacts in the random matrix were Hertzian (point-to-point) contacts. The standard nature of the grain contacts facilitated analysis and modeling.

The use of glass beads also allowed for grain size selection. The majority of granular consolidated and unconsolidated materials are comprised of silt and sand-size particles, 20-5000 μm (Mitchell 1991). The bead diameters were chosen to span the

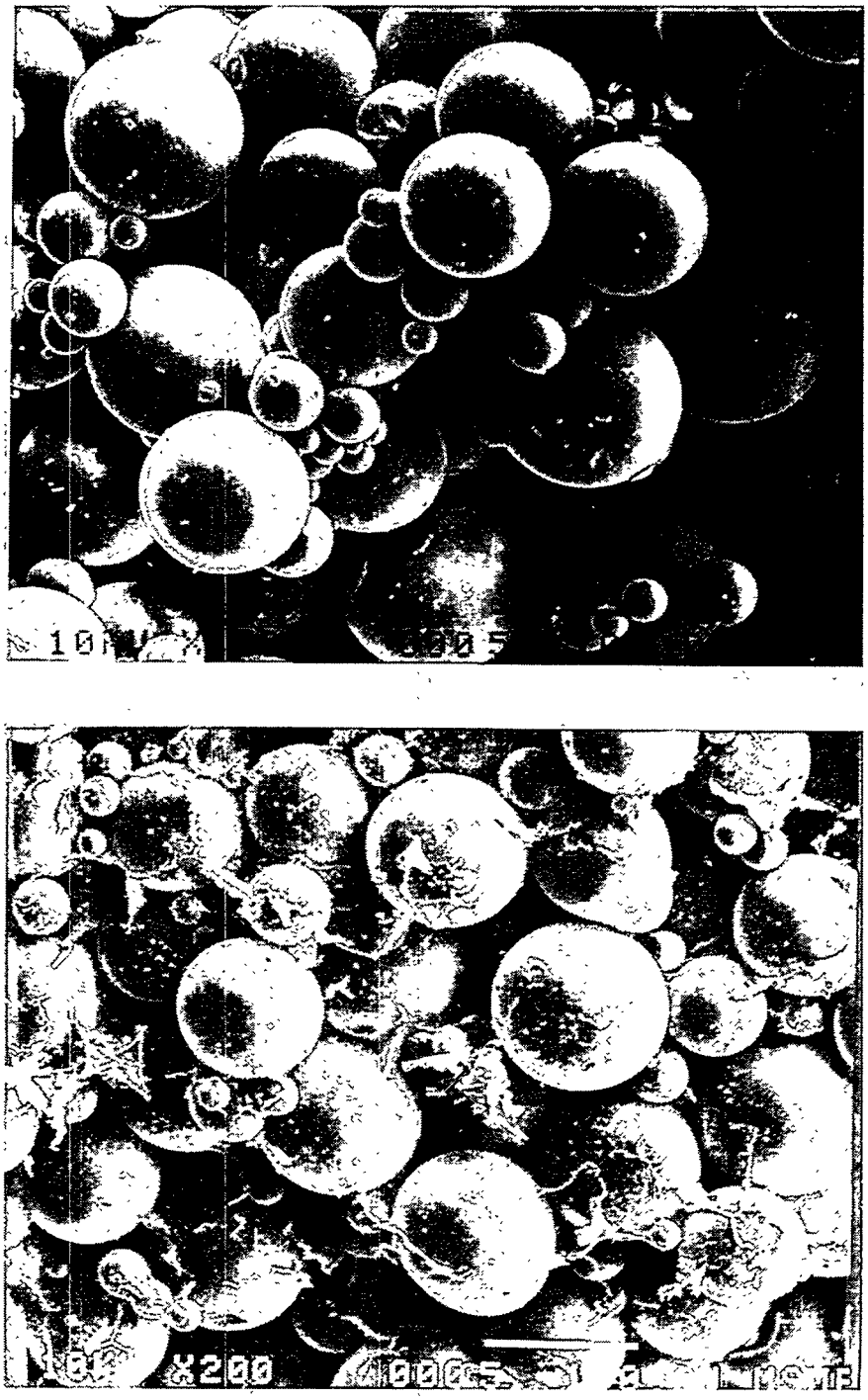

Figure 3.1: Scanning electron microscope photographs of (a) clean glass beads and (b) clay-coated, desiccator-dry glass beads. The scale is the same for both photos and is given in the lower right corner of lower photo; the bar is 100 microns long.

lower extent of sand-size particle classification. Three different diameter size distributions were tested: 53 to 106 microns, 106 to 212 microns, and 212 to 425 microns.

The uniform composition of the glass beads insured that each grain in the matrix had similar elastic and seismic properties. These properties are listed in Table 3.1.

3.2.2 Sample Clay-Coating

To produce a clay film on the beads, a clay solution was mixed with clean beads and then the mixture was dried. A clay film was produced over the entire surface of the beads. This ensured that upon assembly for seismic testing, the clay film would be present at the grain-to-grain contacts.

Sodium-Montmorillonite was used as the clay. It was chosen based on its reactive properties. Extensive isomorphous substitution during formation results in a mineral with significant surface charge. This allows it to react with charged cations and polar molecules. Because of these interactions, montmorillonite can typically absorb up to 400 percent of its weight in water before losing cohesion.

3.2.2.1 Clay Solution Preparation

The clay solution was prepared by stirring 45 grams of sodium-Montmorillonite (Wyoming type SWy-2) into 1.0 liter of distilled water. This slurry was mixed for 10 minutes in a blender at highest speed, then poured into a flask and magnetically stirred for at least two hours. These steps insured that the clay was fully dispersed in the water.

Young's Modulus	E_y	6.28×10^{10} Pa
Bulk Modulus	B	3.75×10^{10} Pa
Shear Modulus	μ	2.57×10^{10} Pa
Density	ρ	2480 kg/m^3
Poisson's Ratio	ν	0.22
Compressional Velocity	c_p	5380 m/sec
Shear Velocity	c_s	3220 m/sec

Table 3.1: Seismic properties of soda-lime glass beads.

After mixing, the clay solution was allowed to settle for three days to remove the trace amounts of sand-size particles present in the initial dry clay. The clay-containing viscous mixture was transferred by pipette into a storage flask. The solution was tested and found to have a pH of 9.0 and a clay concentration of 3.95 $x10^{-3}$ kg-clay/kg-water.

Clay solution for individual sample preparations was obtained by vigorously swirling the flask for approximately 20 seconds before decanting. A more intensive dispersal was not required since the clay solution showed no signs of settling in the storage flask.

3.2.2.2 Clay Coating

Repeatable clay films were produced by slowly adding 100.00 grams of glass beads into 20.20 ml of clay solution. The clay solution volume was chosen to equal the pore volume at saturation, based on a porosity of ~38 percent. The surface tension of the clay solution inhibited its infiltration into the pore space of the beads. Therefore, a small amount of distilled water was added and the sample was stirred to complete the mixing.

The sample was then dried to deposit the clay onto the surfaces of the glass beads. Initially, this was accomplished by placing the sample in an oven at approximately 120 °C for at least 24 hours. Later, the sample was dried by placing it in a vacuum chamber for approximately four hours then in a sealed chamber with Drierite ® desiccant for approximately 5 days. This second procedure yielded specimens with residual clay water contents of 5 percent (wt.-water/wt.-clay). Both procedures resulted in specimen clay contents of 0.8 percent (wt.-clay/wt.-specimen) and average surface densities of approximately 2.5 $x10^{-3}$ kg/m^2.

Figure 3.1b shows the clay-coated beads after desiccation-drying. The evaporation process resulted in distributed, as opposed to uniform, clay films on the beads. This is consistent with the effect capillary suction should have in pulling the clay solution from pores to the region proximate to the bead-to-bead contacts.

3.2.2.3 Clay-Coating Analysis

Scanning Electron Microscopy (SEM) and X-Ray diffraction analysis were used to investigate the extent of clay deposition onto the glass bead surfaces. The samples were covered with a 40 nm carbon layer then bombarded with X-rays at 10 keV to excite the atoms. Peaks in the energy emitted by the excited atoms can be used to identify the elemental composition. Ten keV input voltage is too large to detect oxygen's emissions, but is more accurate in detecting the higher-weight atoms, such as aluminum, that can be used to distinguish the presence of clays.

Table 3.2 gives elemental weight percentages interpolated from K-line emissions. The values are only a relative measurement, since the procedure assumes a 100 percent content for identified elements. They are thus useful only for comparative assessments.

Figures 3.2, 3.3, and 3.4 present the SEM photographs and X-ray emissions spectra and for clean dry glass beads, clay-coated desiccator-dry beads, and clay-coated oven-dry beads, respectively. From the photographs it appears that the dessicator-dry clay has a greater surface area than the oven-dry clay. Indeed, structural changes upon oven drying can be used to classify clays. The thermogram curve for montmorillonite is given in Figure 3.5. Near 100°C, montmorillonite begins to change to a more collapsed structural spacing as exhibited by the endothermic reaction. The long exposure time may have facilitated the structural change in the tested clays.

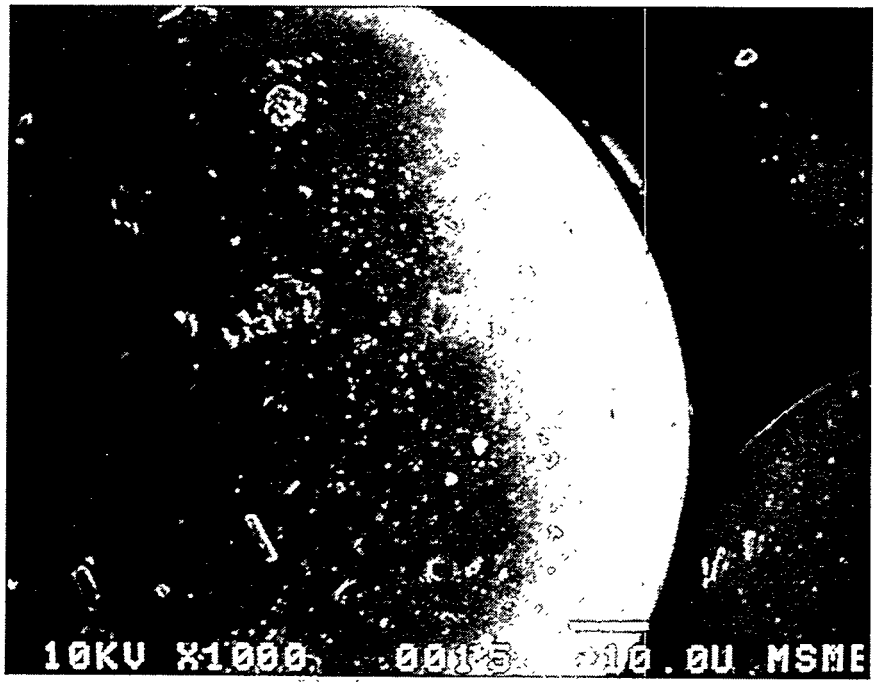

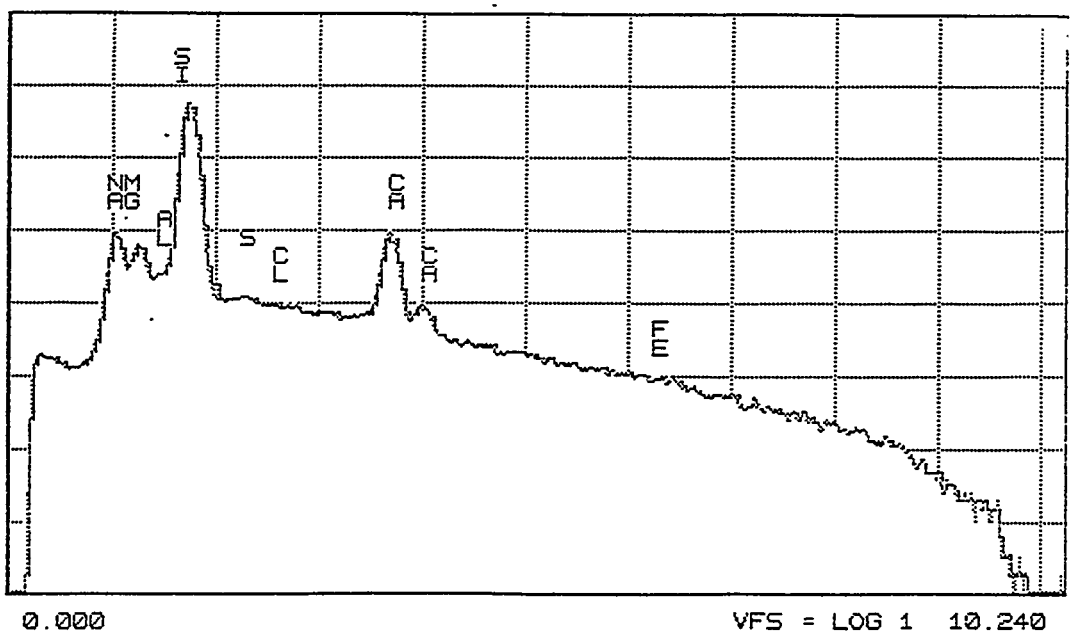

Figure 3.2: The (a) clean, dry glass beads as viewed under the Scanning Electron Microscope and (b) emitted X-ray diffraction spectra. The vertical scale on the spectra is logarithmic. Clean dry beads have only trace amounts of aluminum, chloride, iron, and sulfur.

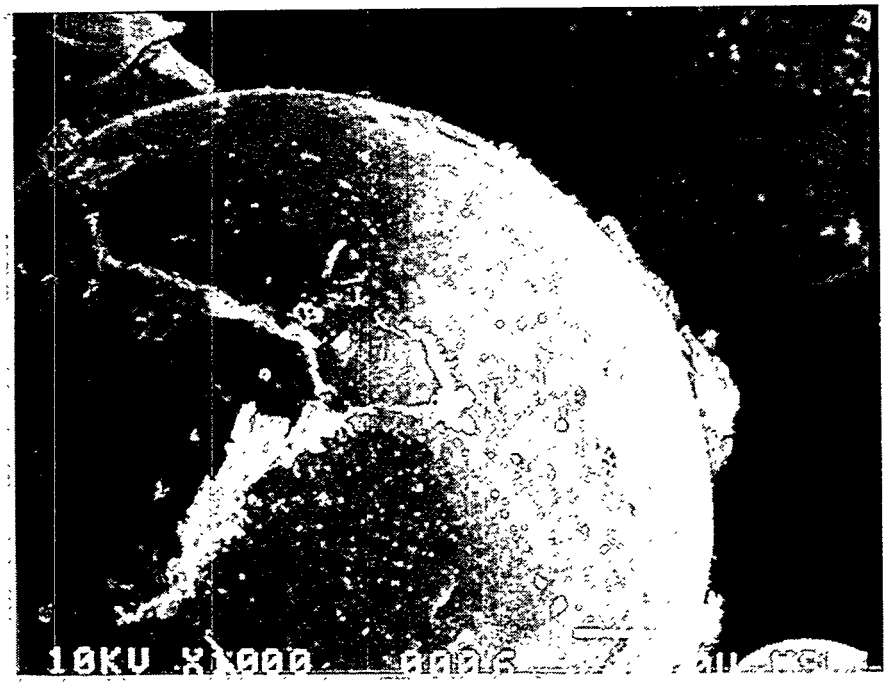

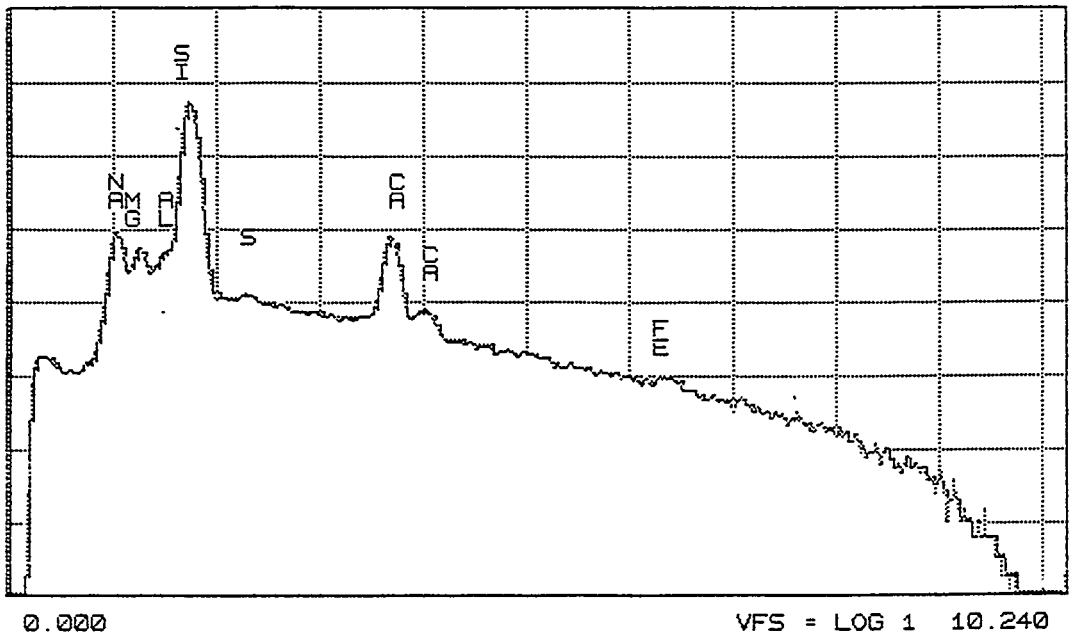

Figure 3.3: The (a) clay-coated, desiccator-dry glass beads as viewed under the Scanning Electron Microscope and (b) emitted X-ray diffraction spectra. The vertical scale on the spectra is logarithmic. Desiccator-dry clay-coated beads have significant amounts of aluminum, iron, and sulfur and only trace amounts of chloride.

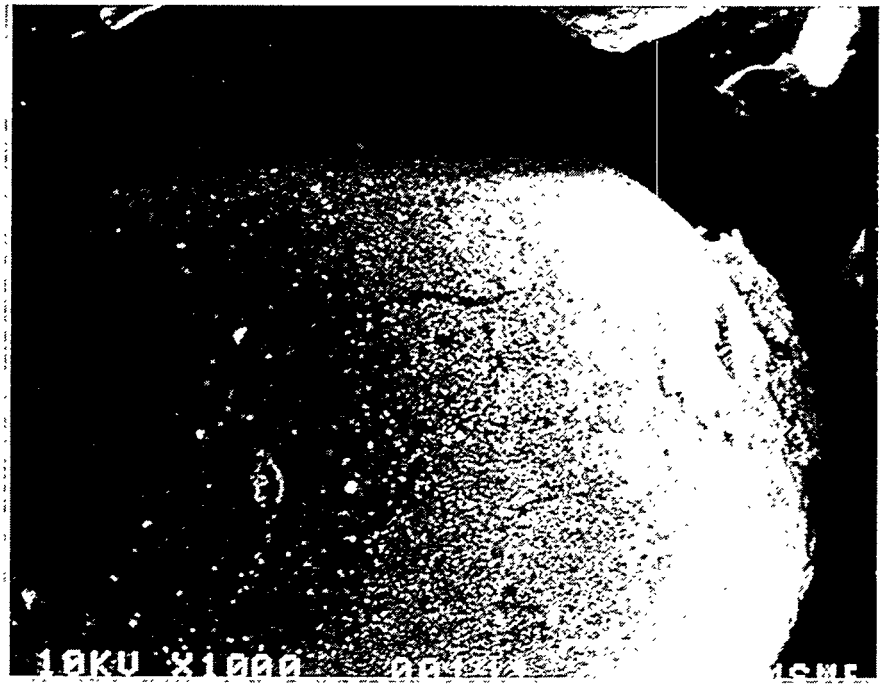

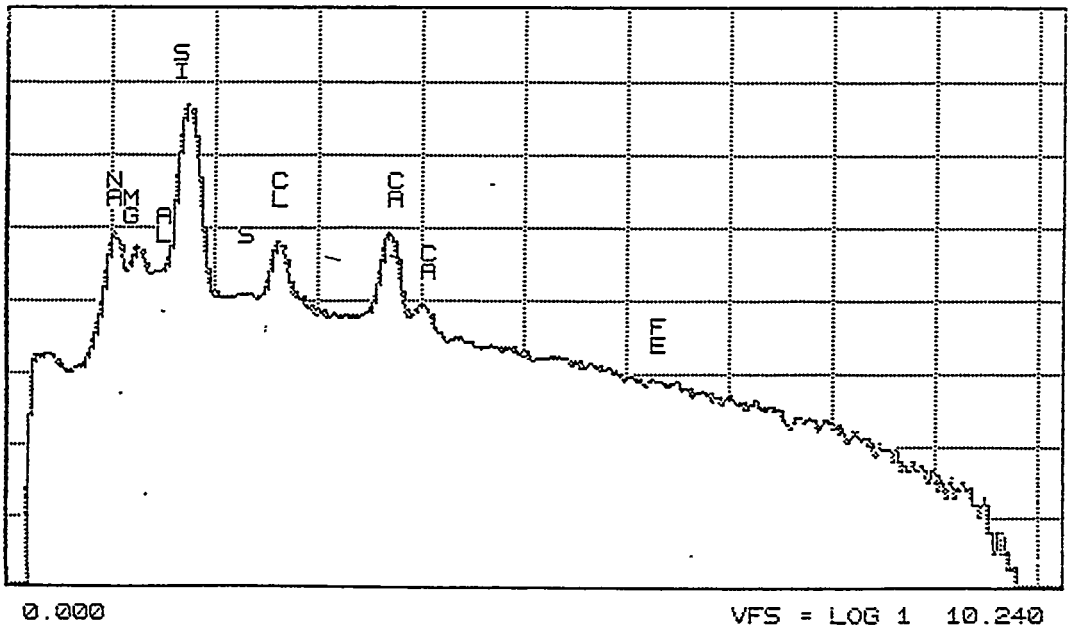

Figure 3.4: The (a) clay-coated, oven-dry glass beads as viewed under the Scanning Electron Microscope and (b) emitted X-ray diffraction spectra. The vertical scale on the spectra is logarithmic. Oven-dry clay-coated beads have significant amounts of aluminum and chloride and only trace amounts of sulfur.

Thermogram for Montmorillonite Clay

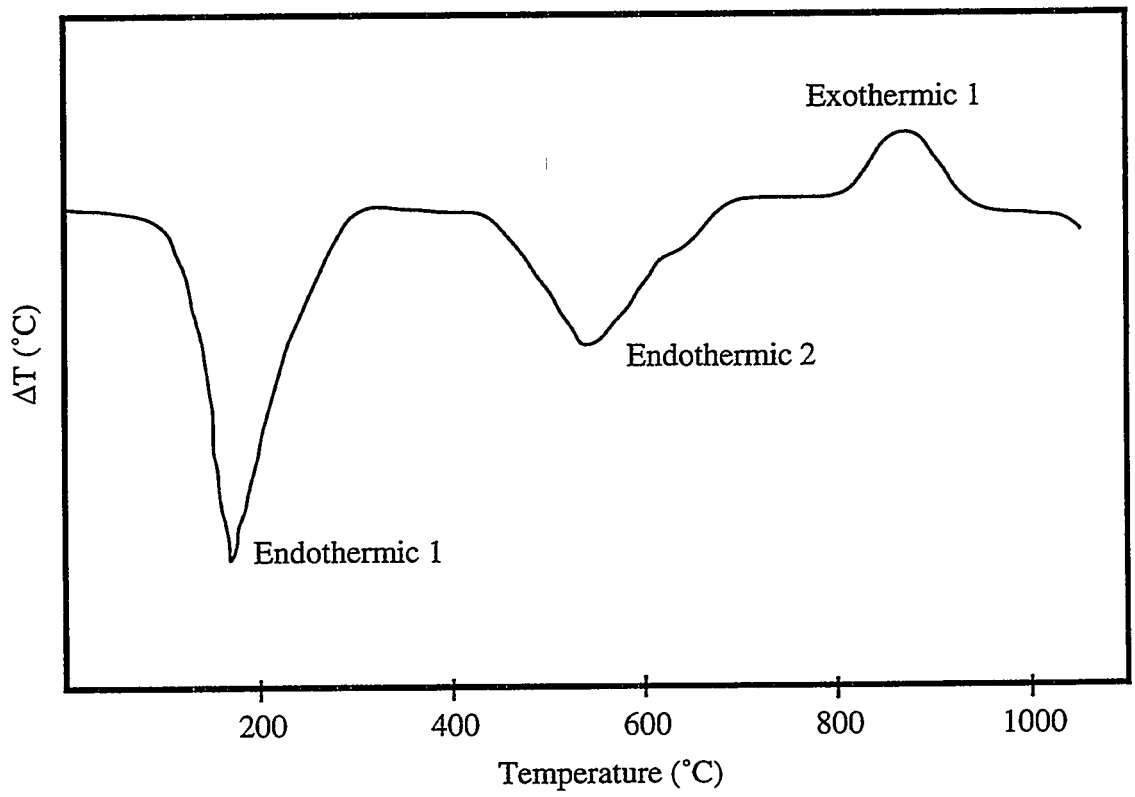

Figure 3.5: Schematic diagram of thermogram for montmorillonite clay. Temperature trends are based on van Olphen, 1977 and Mitchell, 1991. Clay begins first change in structure near 100°C.

The three sets of dry beads have different emissions spectra. Clean dry glass beads are composed mainly of silicon, calcium, and sodium consistent with their soda-lime composition: 75 percent SiO_2, 15 percent Na_2O, and 10 percent CaO. Desiccation-dry clay-coated beads show additional peaks for aluminum and iron consistent with the presence of montmorillonite clay. Montmorillonite clay is defined as $Al_2Si_4O_{10}(OH)_2x\ H_2O$. Iron-rich forms, with Fe^3 commonly substituting for Al, are termed nontronites. When the clay-coated beads are oven-dried instead of desiccation-dried, the aluminum peak disappears and a chloride peak appears. Because of the high amount of chloride, it was unclear whether the film seen on the measured surface was a salt or clay film.

Clay solution, plain beads, and desiccation-dry beads were dried in the oven and then analyzed to investigate the appearance of the chloride peak in oven-dry samples. The spectra and associated photographs are given in Figures 3.6, 3.7, and 3.8 respectively and the interpolated weight percentages are in Table 3.2. Dry clay alone has elevated levels of aluminum, calcium, iron, and sulfur. Dry beads alone show an elevated level of chloride and do not have aluminum and iron peaks. Oven-dried, desiccated clay-coated beads show aluminum, chloride, and iron peaks.

Three conclusions have been reached from this analysis. First, the lack of chloride peak in the oven-dry clay indicates that the chloride did not originate in the clay. The elevated level in oven-dry plain beads suggests that the increased temperature caused reactions within the beads themselves that released chloride. Second, the aluminum and iron peaks in all clay-coated samples show that their presence can be used to identify the presence of clay. Third, the distributed films seen in the photographs of clay-coated beads, but not in the clean beads, suggests that film seen in the photographs is a clay film that is distributed across the surfaces of the beads. The large clay clumps are the result of more clay deposition on the bead surfaces adjacent to pores.

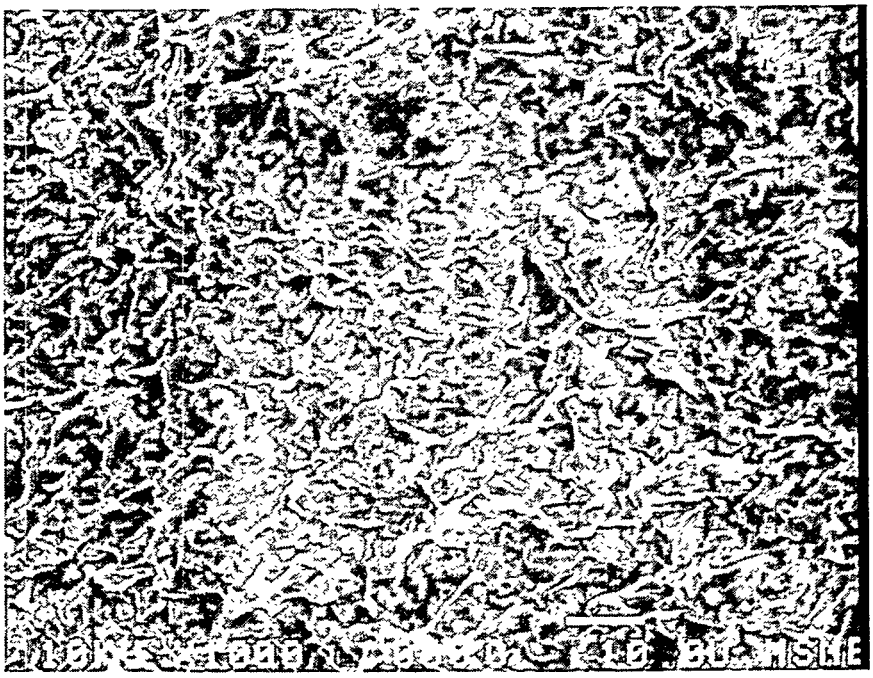

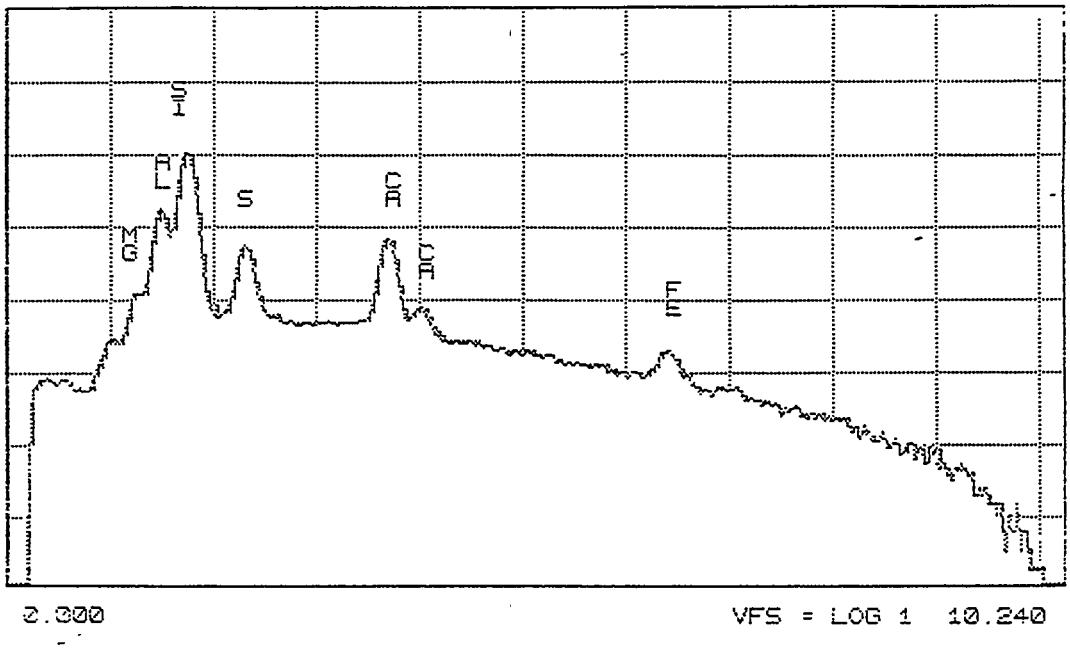

Figure 3.6: The (a) oven-dried montmorillonite clay as viewed under the Scanning Electron Microscope and (b) emitted X-ray diffraction spectra. The vertical scale on the spectra is logarithmic. The clay has significant amounts of aluminum, iron, and sulfur indicating that their peaks can be used to identify clay.

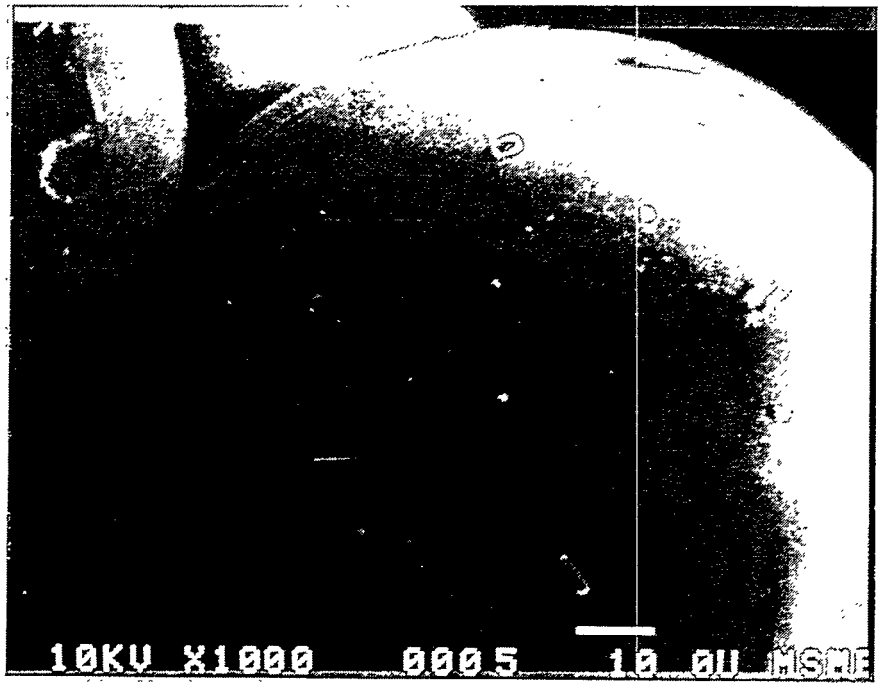

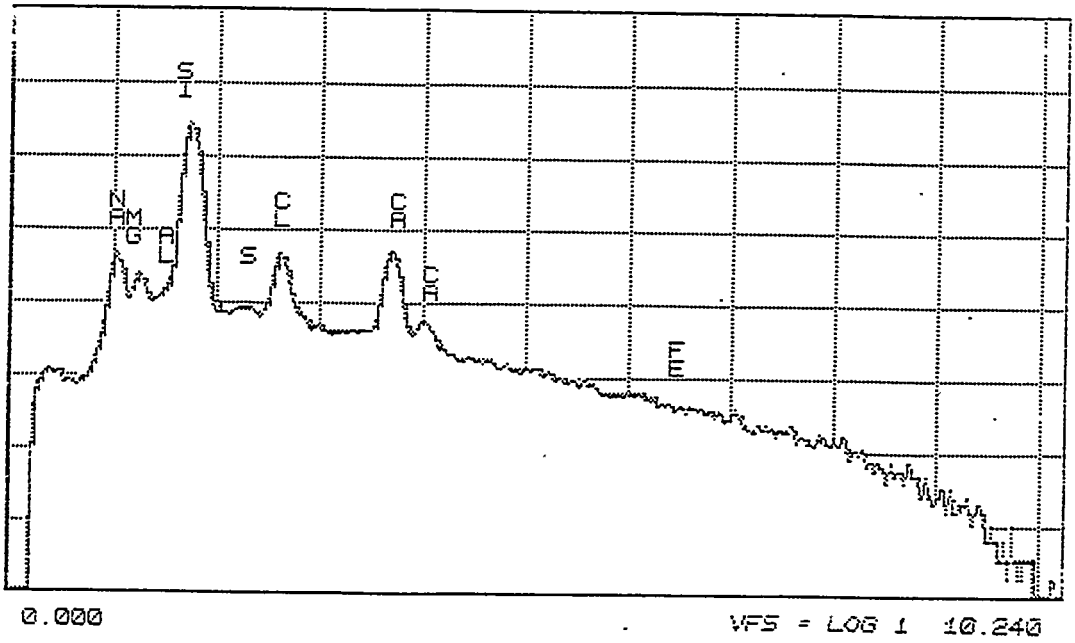

Figure 3.7: The (a) oven-dried clean glass beads as viewed under the Scanning Electron Microscope and (b) emitted X-ray diffraction spectra. The vertical scale on the spectra is logarithmic. The clean oven-dried beads have little aluminum, iron, and sulfur but significant amounts of chloride suggesting that the chloride comes from the beads themsevles.

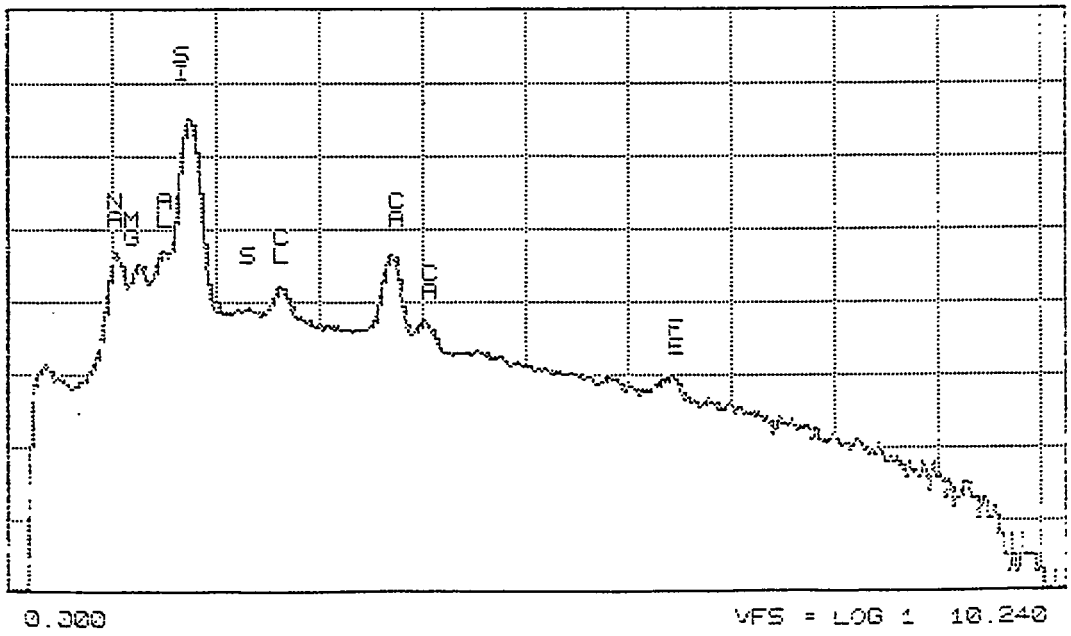

Figure 3.8: The (a) clay-coated, desiccator-dry glass beads that were further dried in the oven, as viewed under the Scanning Electron Microscope and (b) emitted X-ray diffraction spectra. The vertical scale on the spectra is logarithmic. The beads have significant amounts of aluminum, chloride, iron, and sulfur.

Test	Al	Ca	Cl	Fe	Mg	Si	Na	S
Plain Beads	0.00	13.8	0.23	0.40	4.01	70.07	10.81	0.68
Desiccation-Dry Clay Beads	0.99	13.12	NM	1.21	2.71	70.28	11.13	0.56
Oven-Dry Clay Beads	0.00	13.29	6.47	1.40	2.74	65.79	10.00	0.32
Oven-Dry Clay	12.95	20.80	0.48	7.51	1.14	46.41	NM	10.71
Oven-Dry Plain Beads	0.00	16.51	9.27	0.00	1.67	71.81	NM	0.73
Oven-Dry Desiccated Clay Beads	1.55	14.16	3.29	4.04	1.22	75.06	NM	0.68

Table 3.2: X-ray interopolated weight percentages of indicated elements for the tested glass bead samples.

3.2.3 Fluid Addition

Three fluids were investigated: distilled water, ethyl alcohol, and hexadecane. They were chosen for their ability to interact with clay. The polar fluids are expected to have a greater interactions than the non-polar fluid. The fluid properties are given in Table 3.3. Unlike experiments with clean surfaces, i.e. not clay-coated, the seismic properties of fluids are not directly important. The properties of the clay-fluid mixture will control the mechanical behavior of the specimen. Therefore, the important properties are those that govern the clay-fluid interactions, as given by equation 2.40.

The fluids were added to the specimen by vapor deposition in a sealed clean box. The fluids placed in a contained inside the sealed box, then evaporated by applying heat to the container. Evaporated fluid condensed on the colder, clay-coated beads. To facilitate fluid adsorption, the beads were mechanically separated before insertion in the box and spread into thin layers in five petri dishes. The fluid content of the clay was controlled by regulating the vapor pressure and exposure time. The fluid content was measured by weighing a mixed sample of the prepared beads before and after drying in a 120°C oven for at least 24 hours.

3.2.4 Sample Assembly

After fluid saturation, the prepared beads were transferred into a cylindrical polyethylene jacket. Between the addition of beads from each petri dish, the beads were compacted using an aluminum slug. General specimen dimensions were either 0.0429 m (1.69") or 0.0254 m (1.00") in length and 0.0508 m (2.00") in diameter. Samples fluctuated about these dimensions due to variable compaction caused by the changing clay properties. The parameters of all tests conducted are given in Table 3.4.

Fluid	Density (kg/m^3)	Viscosity (cP)	Molecular Polarity	Molecular Radius (Å)	Dipole Moment (Debyes)
Water	998.2	1.002	Polar	3.1	1.85
Ethyl Alcohol	789.3	1.200	Polar	4.6	1.69
Hexadecane	773.3	3.340	Non-Polar	12.3	-

Table 3.3: Fluid properties for the fluids absorbed into the clay-coating.

Test Name	Bead Condition	Bead Size (μm)	Fluid	Clay Fluid Content	Specimen Fluid Content	Length (m)
GBD1	Dry, Clean	212-425	none	-	0 %	0.0429
GBD2	Dry, Clean	106-212	none	-	0 %	0.0429
GBD3	Dry, Clean	53-106	none	-	0 %	0.0429
GBD7	Dry, Clean	53-106	none	0 %	0 %	0.0254
GBW1	Clean	53-106	water	-	100 %	0.0280
GBE2	Clean	53-106	ethyl alcohol	-	100 %	0.0259
GBH1	Clean	53-106	hexadecane	-	100 %	0.0271
GBDC1	Dry, Oven-Dry Clay	53-106	none	0 %	0 %	0.0254
GBDC4	Dry, Desiccator-Dry Clay	53-106	none	5%	0.04%	0.0251
GBW2	Clean	53-106	water	(300 %)	2.40%	0.0254
GBCW4	Clay-coated	53-106	water	60 %	0.48 %	0.0254
GBCW6	Clay-coated	53-106	water	80 %	0.64 %	0.0256
GBCW5	Clay-coated	53-106	water	140 %	1.12 %	0.0277
GBCW7	Clay-coated	53-106	water	200 %	1.60 %	0.0269
GBCW3	Clay-coated	53-106	water	300 %	2.40 %	0.0274
GBCW8	Clay-coated	53-106	water	-	100%	0.0235
GBCE3	Clay-coated	53-106	ethyl alcohol	200 %	1.60 %	0.0236
GBCH1	Clay-coated	53-106	hexadecane	50 %	0.40 %	0.0261

Table 3.4: Parameters for glass bead specimen tests.

The larger number of interfaces suggested that minor contamination by air-borne dust would not significantly effect the transmissions. Therefore, samples with water were assembled outside the clean box. Ethyl and hexadecane-containing samples were assembled inside the clean box to prevent water absorption.

3.3 Seismic Testing

The semi-compacted specimens were placed into the load frame for seismic testing in the apparatus shown in Figure 3.9. Axial stress on the specimen was controlled by a deadweight pump (Ashcroft portable gauge tester). Confining stress was controlled by a screw pump connected to the water-filled confining cell. Stresses were maintained at hydrostatic conditions to minimize breakage of the glass beads and cycled three times prior to testing to further enhance specimen compaction before seismic waves were propagated. Mean stresses ranged from 2.4 to 14.8 MPa (~2150 psi).

Two similar transducers were used to perform the seismic wave propagation tests. A cross-sectional diagram of a transducer is given in Figure 3.10. The transducers consist of two piezoelectric crystals located between three electrodes. A rubber spacer at the top of the transducers separates the top electrode from the casing, used as the bottom electrode. This rubber spacer is pressurized to couple the crystal and aluminum electrode surfaces.

Ultrasonic waves were generated by applying an ~1000 volt, 640 nanosecond pulse across the piezoelectric crystal. Compressional (P) waves were generated by connecting Port 2 to the voltage pulse, and grounding the other two electrodes. The peak frequency of the generated P-wave was ~800 kHz. Shear (S) waves were generated by connecting Port 3 to the voltage pulse, and grounding Port 1. Port 2 was not grounded

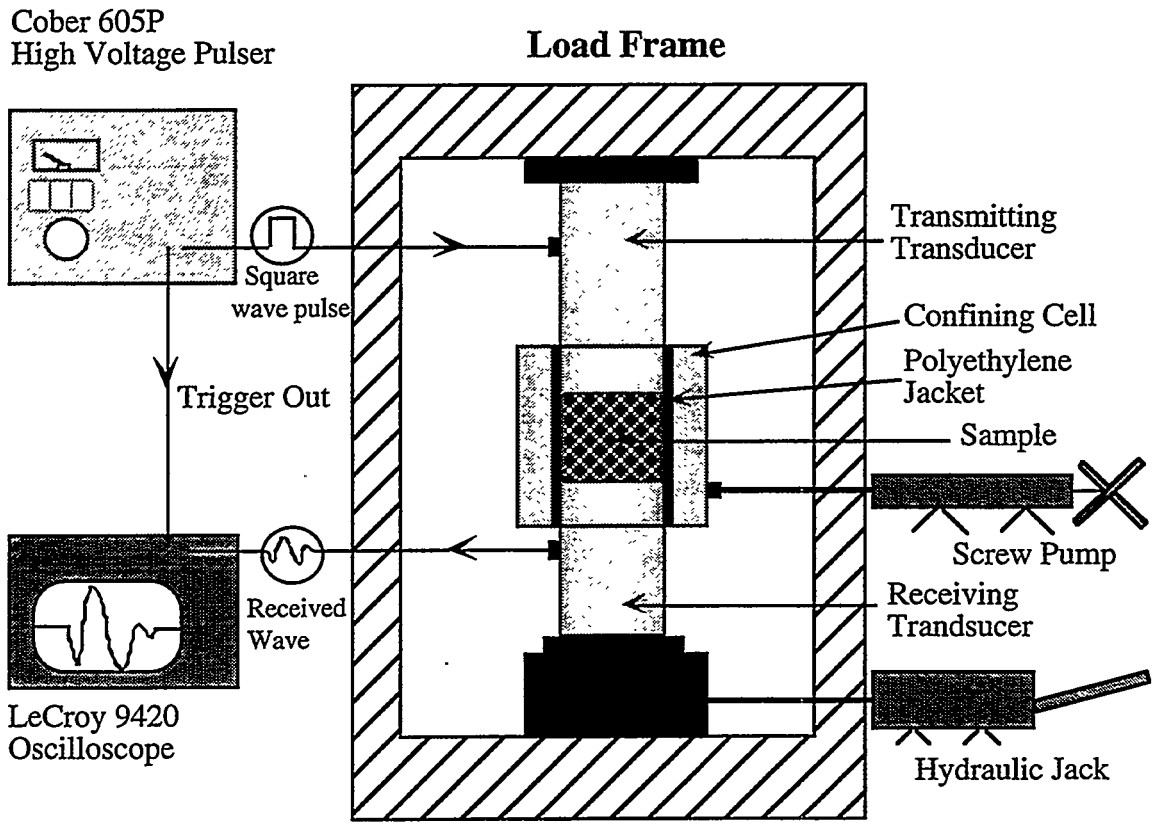

Figure 3.9: Schematic diagram of the laboratory equipment used in the experiments.

Schematic Diagram of a Seismic Transducer

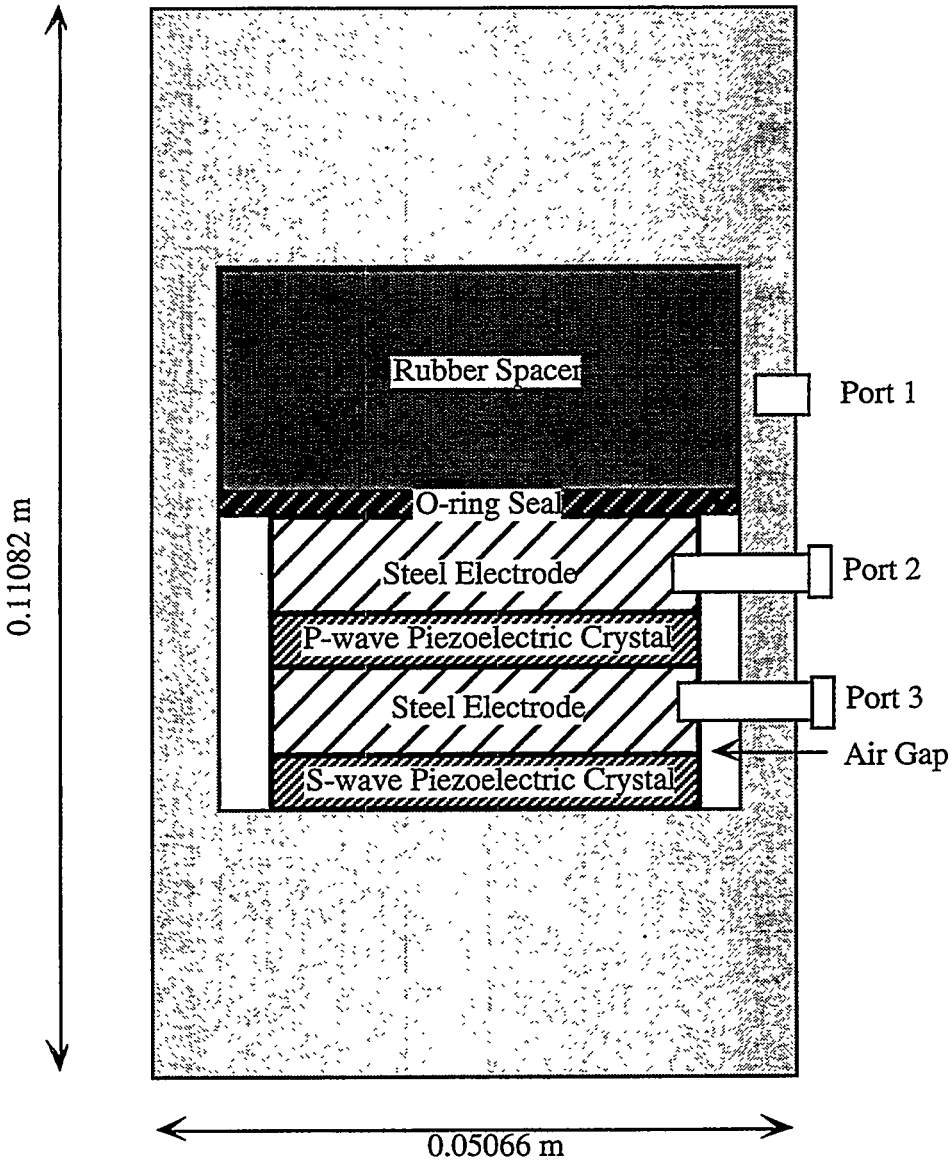

Figure 3.10: Schematic diagram of seismic transducers used in the laboratory testing. The seismic waves are generated by excitation of piezoelectric crystals. P-waves require voltage into Port 2, with Ports 1 and 3 grounded. S-waves require voltage into Port 3, with Port 1 grounded.

during S-wave testing to minimize the generation of P-waves. The peak frequency of the generated S-wave was ~525 kHz. The transmitted ultrasonic waves were measured in the receiving transducer using wire connections similar to the transmitting transducer. However, in the receiving transducers the measuring electrode port was connected to a LeCroy Digital Oscilloscope ® instead of the pulse generator.

Ultrasonic waves were transmitted upon loading and unloading the sample during the fourth stress cycle. Loading stresses ranged from 2.5 to 14.8 MPa in steps of ~1.2 MPa. Unloading stresses ranged from 14.8 to 2.5 MPa in steps of ~2.4 MPa. For each wave, 200 individual transmissions were conducted at each stress. These transmissions were stacked to reduce noise, and the resulting trace stored on the LeCroy Oscilloscope for further analysis.

After the seismic tests were completed, the wave traces were inspected on the oscilloscope to measure the arrival time and the peak-to-peak voltage. The traces were then transferred to a Macintosh IIci ® computer using the Labview ® application, and stored on High Density floppy disks for permanent storage. The Matlab ® application was used to analyze the frequency content of the transmitted waves. This allowed the peak frequencies, attenuation coefficients, and quality factors to be calculated.

When possible, aluminum calibration tests were conducted immediately after the specimen test. This preserved the effects of minor changes in input signal voltage and also captured the effects of environmental conditions, such as temperature and humidity, on the testing apparatus. These calibrations were used in calculations of the attenuation coefficients and quality factors.

3.4 Calibration Tests

Four different sets of tests were performed to check the sample preparation procedures. These tests included checks on compaction, repeatability, bead size scattering, and specimen length.

3.4.1 Compaction Test

To insure repeatable grain matrix configurations, it was necessary to compact the beads. This was done in two separate steps. First, the beads were compacted by tamping the beads after adding each petri dish during assembly of the specimen. Second, the specimen was subjected to stress cycling in the load frame before measuring seismic wave propagation.

A test was conducted to measure the effect of compaction during stress cycling on seismic wave propagation in clean, dry beads. Seismic propagation measurements were made at 1.2 MPa intervals as the specimen was loaded and unloaded from 2.4 to 14.8 MPa during four stress cycle loadings. The P and S-wave traces at the highest stress are shown in Figure 3.11. For both wave types, the first arrival times changed little as the sample is cycled but the S-wave traces showed a shift in frequency as the compaction increased. There is also a notable change in the transmitted amplitudes. These changes decrease after the third stress cycle. Both velocity, amplitude, and frequency variations are much less than changes expected for differences in stress level and composition.

Another test examined the effect of compaction as stress was held constant. Both clean, dry beads and clay-coated, dry beads were investigated. The specimens were

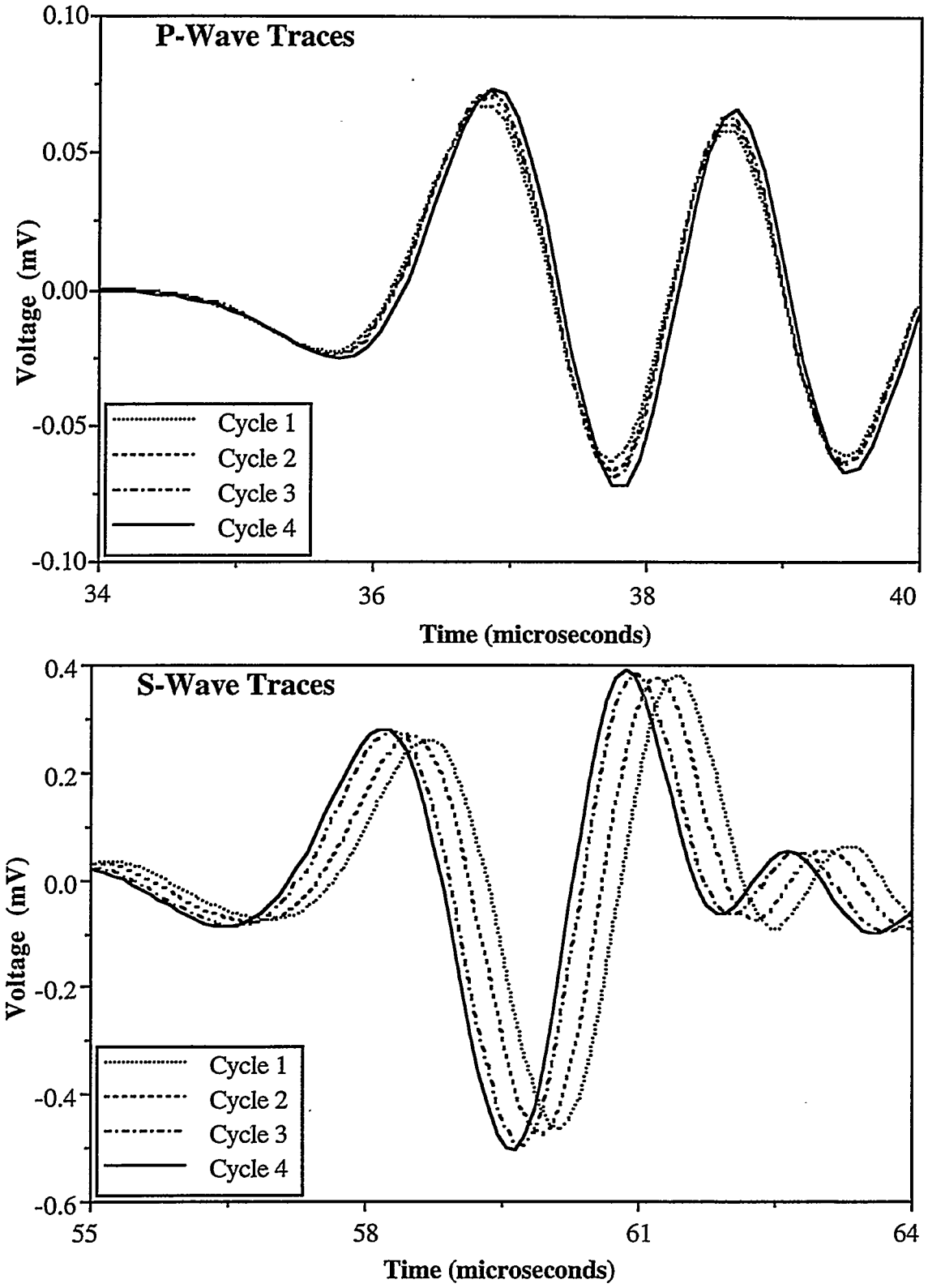

Figure 3.11: The (a) P-wave and (b) S-wave traces at 14.8 MPa for clean dry beads as stress is cycled. Cycling the stress improves the transmission, with changes tapering off by the fourth stress cycle.

cycled three times, then held at the highest stress, 14.8 MPa, for 1800 seconds (30 minutes) while seismic propagation measurements were conducted. The stresses were then lowered to 7.4 MPa and the seismic measurements repeated over 30 minutes. The peak-to-peak amplitudes are shown in Figure 3.12 For both clean and clay-coated beads, the amplitudes increased slightly during the first 500 seconds. They then remained constant for the duration of the test. Measurements at the lower mean stress showed no significant change with time.

Based on these tests, a standard procedure was established to compact the specimens. The specimen was stress cycled three times before seismic testing was started. It was believed that further stress cycling would not improve compaction and could lead to damage of the specimen. During the third stress cycle, the highest stress was maintained for at least 10 minutes to minimize the effects of constant stress creep. Seismic measurements began immediately upon returning to the lowest stress.

3.4.2 Repeatability Test

Tests were conducted with dry glass beads to insure that preparation procedures generated samples with repeatable seismic signatures. It proved surprisingly difficult to produce directly repeatable samples. Seismic measurements proved to be very sensitive to instrumental variations, including source strength and source-to-sample bonding. To overcome these difficulties, the signals were matched on the LeCroy before testing, lead foil couplers were punched at the same time, and identical weight beads were tested.

Comparable tests were confirmed by repeatable dry bead tests measured 15 days apart. The S-wave traces from these tests are shown in Figure 3.13. These measurements

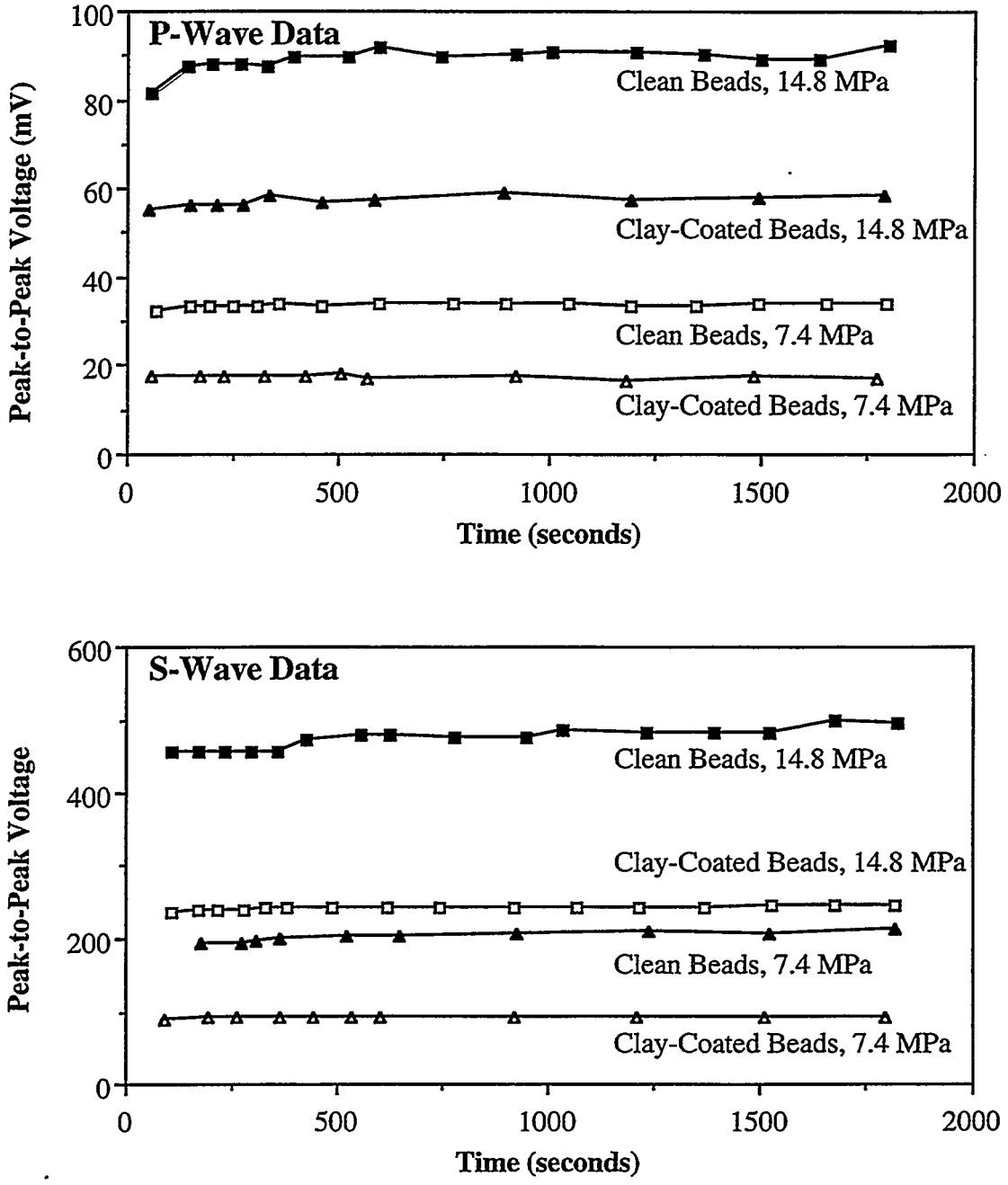

Figure 3.12: (a) P-wave and (b) S-wave peak-to-peak amplitudes over time as stress is held constant. Results for dry clean beads and dry clay-coated beads at two different stress levels are presented. Changes due to compaction are evident during the first 600 seconds (10 minutes). The velocities for the tests exhibited no changes.

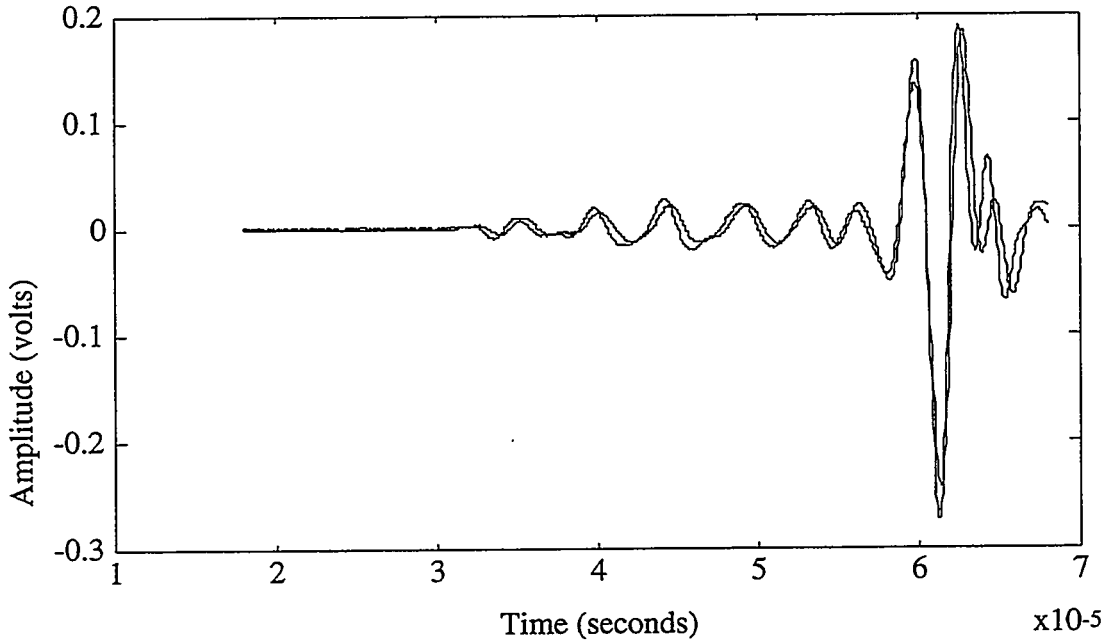

Figure 3.13: S-wave traces from two different dry glass bead samples measured 15 days apart. The close agreement in velocities and amplitudes indicates that sample procedures can produce repeatable samples.

were made at 14.8 MPa for samples lengths of 0.0254 m (1.00"). The traces are very similar. The timing of the seismic events are in good agreement. The magnitudes of the seismic events vary slightly. This can be attributed to slight variations in sample lengths, matrix configurations, or transducer-to-sample bonding.

3.4.3 Bead Size Test

The determination of the proper bead size for the experimental tests was governed by the relationship between sensitivity and attenuation. Sensitivity is the need to have a sufficient number of interfaces to accurately measure their effects on seismic wave propagation. However, a large number of interfaces may also cause significant attenuation. There needs to be sufficient amplitude transmitted to accurately detect the variations in clay.

Three bead sizes were tested to determine the most appropriate size for experimental measurements. Specimens, 0.0429 m (1.69") in length, were prepared using clean, dry beads. The seismic traces at the highest stresses are shown in Figure 3.14. First arrival times vary only slightly between the bead sizes. Amplitudes are significantly different. For both P and S-wave transmission, the amplitudes are inversely related to size: the smallest beads have the most amplitude transmission and the largest beads have the least amplitude transmission. Peak-to-peak amplitudes are inversely related to attenuation. Thus, attenuation is directly related to bead size. Although not presented, Fourier transforms of the first wave cycle for each bead size confirm this trend.

Seismic wave scattering occurs by two mechanisms. Seismic waves can be scattered off an interface. Therefore, an increase in number of interfaces may increase scattering and thus attenuation. Because the 53-106 μm glass beads are smaller in size,

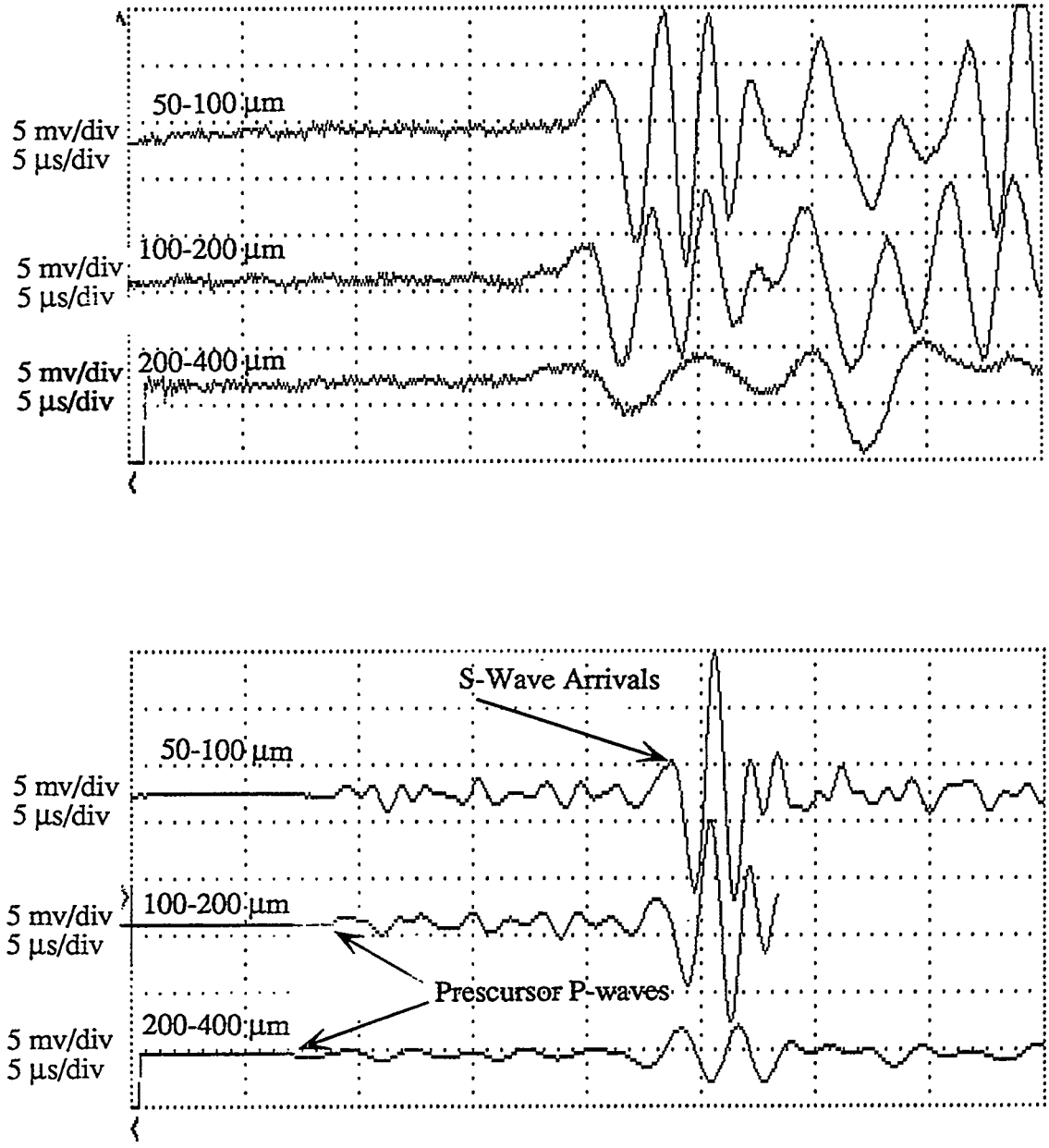

Figure 3.14: Traces for three different grain distribution sizes for (a) P-waves and (b) S-waves. The smallest beads, 50 to 100 microns in diameter, transmit the most energy. The specimen lengths are 0.043 m (1.69").

they have more interfaces for equal volumes. However, when grain size is within an order of magnitude of the seismic wavelength, the waves can be strongly attenuated by Mie scattering. The number of beads per wavelength for the dry propagation specimens are shown in Table 3.5. The glass beads in the 106-212 and 212-425 μm size distributions are both in the range of strong scattering ($\lambda \approx 10$ beads). Because the largest beads had the smallest amplitude transmission, and thus largest attenuation, in these experiments the grain size effect causes more scattering than the interface effect. It is fortuitous that the beads with the most sensitivity (the most interfaces) have the least attenuation. The beads in the range 53-106 μm will be used in the subsequent tests.

3.4.4 Specimen Length Test

The small amplitudes, and thus high attenuations, in the 0.0430 m length bead specimens suggested that at this length it might be difficult to observe significant differences in specimens. The addition of clay was expected to increase attenuation and therefore exacerbate the difficulty in quantifying differences. To increase transmitted amplitudes, and thus the magnitude of differences between the various specimens, the specimen length was decreased from .0430 (1.69") to .0254 m (1.00").

As expected, changing the length did not affect the velocities. Decreasing the specimen length did affect the peak frequency and spectral amplitudes for both wave types. P and S-wave traces spectra at the two different lengths are compared in Figure 3.15. For the P-wave transmissions, decreasing the length increased the peak frequency by 58 percent, from 235 to 372 kHz, and the spectral amplitude by 110 percent, from .2743 to .5749 mV/1024 points. For the S-wave transmissions, decreasing the length increased the peak frequency by 7 percent, from 293 to 313 kHz, and the spectral amplitudes by 142 percent, from 4.3745 to 10.5708 mV/1024 points.

Bead Size (μm)	P-wave velocity (m/sec)	P-wave λ (μm)	# beads per λ	S-wave velocity (m/sec)	S-wave λ (μm)	# beads per λ
53-106	1368	1666	21.0	760	1440	24.2
106-212	1373	1672	10.5	747	1415	8.9
212-425	1277	1555	4.9	749	1420	4.5

Table 3.5: Parameters for seismic waves in the different size dry glass beads.

Frequency Spectra for Length Comparison

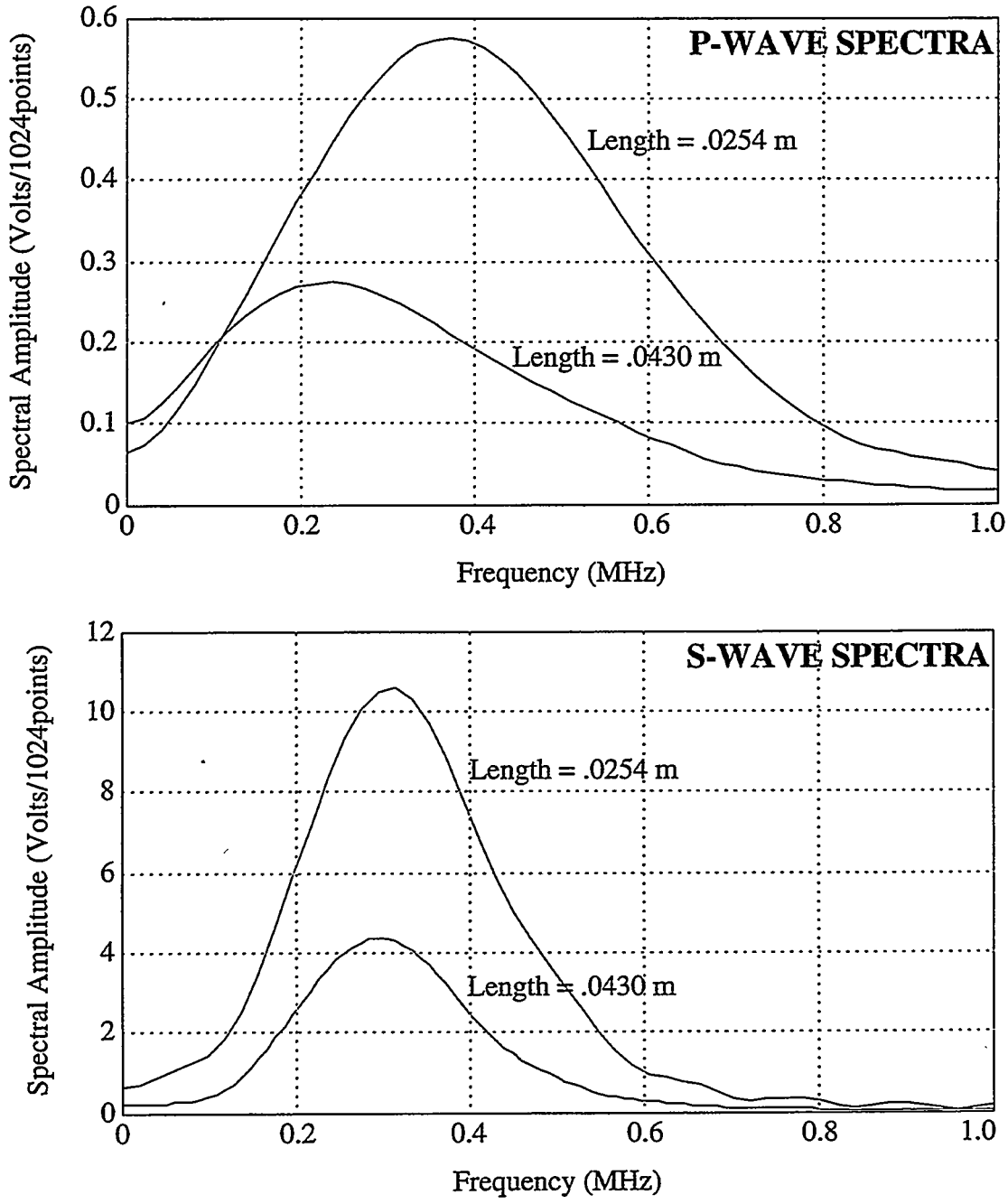

Figure 3.15: Spectral amplitudes for (a) P-waves and (b) S-waves for specimen lengths of 0.043 and 0.025 m. Spectral amplitudes and the P-wave peak frequency are larger for the shorter specimens.

4.0 Effects of Mineralogy, Fluid Chemistry, and Fluid Content

4.1 Introduction

The purpose of this investigation was to compare the seismic behavior of granular materials with different contact rheologies. Contact rheologies were varied by altering the chemistry and content of fluid absorbed into a clay layer coating individual spherical glass beads. Variations in the clay properties were expected to change the rheologic conditions at grain-to-grain contacts. It was anticipated that rheologic changes would affect seismic propagation. Eleven experiments were conducted; the parameters for these experiments are given in Table 3.4.

An example of the seismic traces is shown in Figure 4.1 for P-waves and Figure 4.2 for S-waves. The S-wave traces shows a smaller, pre-cursive P-wave arrival that results from conversion of the S-wave at the upper sample boundary. Due to the arrangement of the crystals, both wave types arrive by breaking in the down direction. The traces vary in arrival time, peak-to-peak amplitude, and spectral frequency content. The changes are investigated using quantitative analysis techniques.

4.2 Analysis Techniques

The response of the seismic traces was investigated by examining group velocities, spectral amplitudes, frequency contents, and quality factor data. Examination of the changes in these parameters provides a basis for determining the mechanisms that control seismic behavior.

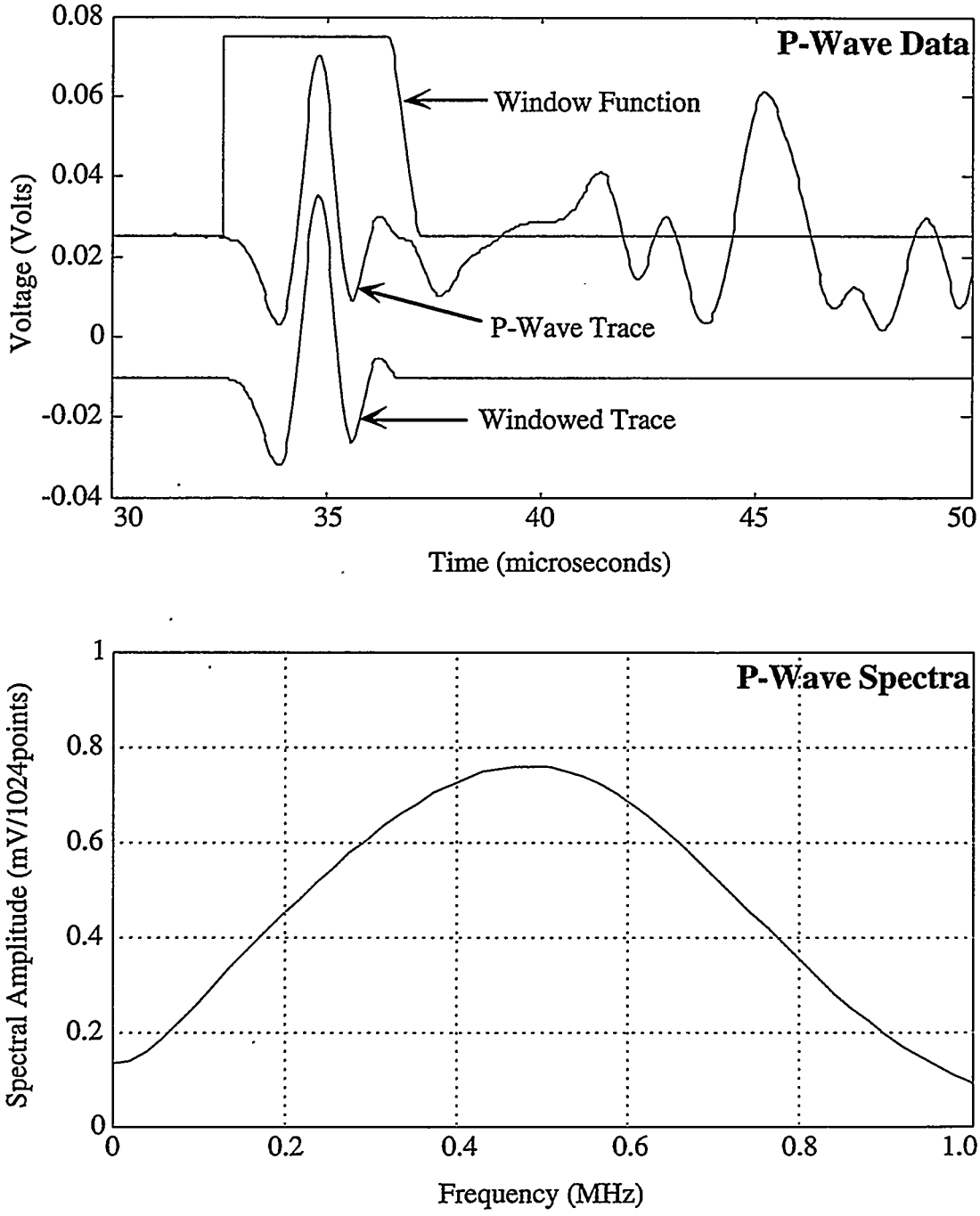

Figure 4.1: Calculation of P-wave frequency spectra from trace data. Graph (a) shows the actual trace, the window function, and the windowed trace. Graph (b) shows the frequency spectra of the windowed trace. The trace is from the 80 percent clay water content experiment at 14.7 MPa.

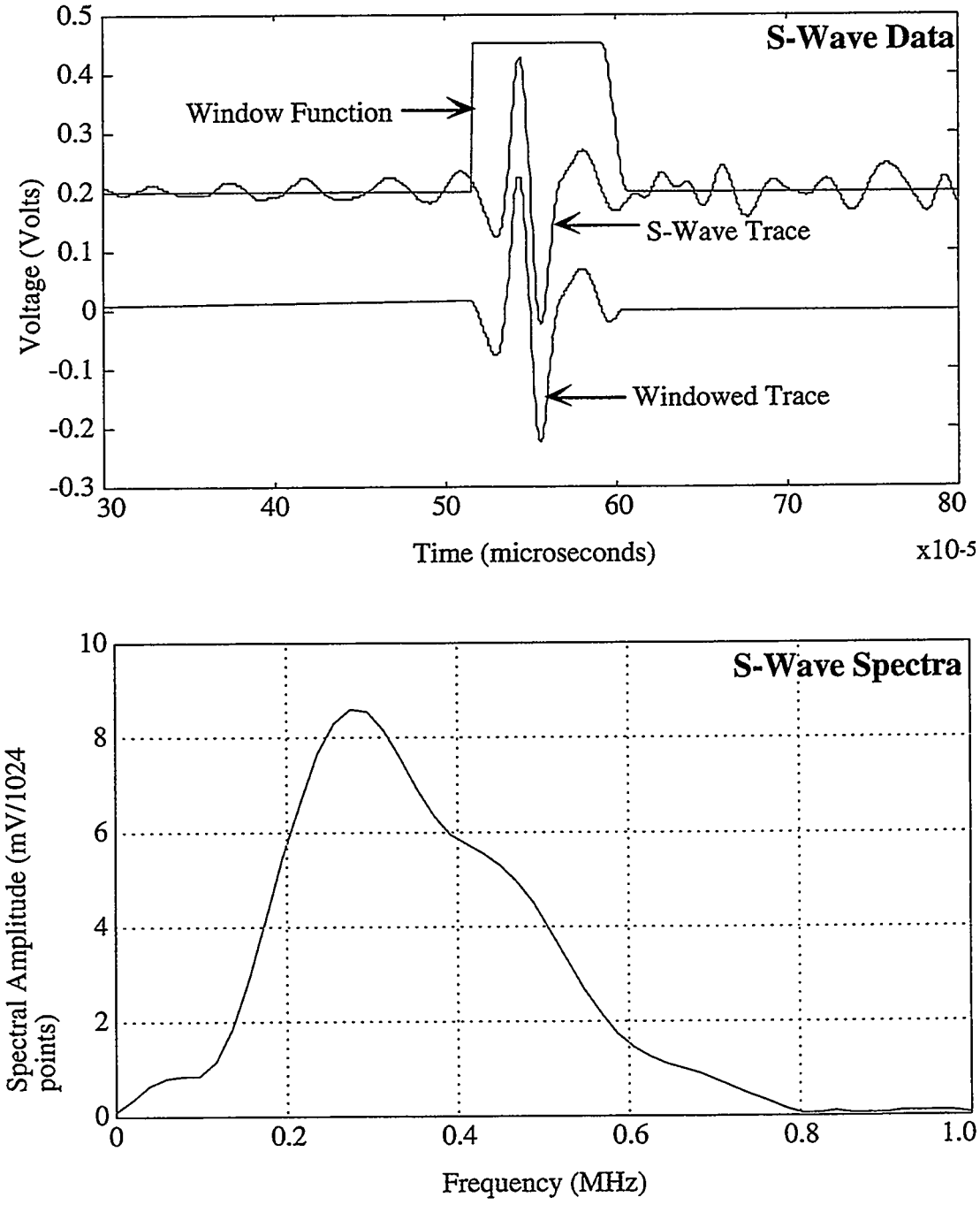

Figure 4.2: Calculation of S-wave frequency spectra from trace data. Graph (a) shows the actual trace, the window function, and the windowed trace. Graph (b) shows the frequency spectra of the windowed trace. The trace is from the 80 percent clay water content experiment at 14.7 MPa.

The first-break arrival time was measured and used to calculate group velocity. For further analysis, the wave train was fast-Fourier transformed to obtain the spectral amplitude versus frequency data. This procedure is shown in Figures 4.1 and 4.2 for representative P-wave and S-wave traces respectively. The full seismic trace was windowed to insure that only the directly arriving wave was transformed. This window was of the form of a modified boxcar function. The first part of the window is a boxcar function, with values set equal to unity. The end of the window is a half Hanning Function, with values decreasing to zero in a cosine decay. The cosine tail smoothed the effect of the incoming coda and also reduced spectral leakage. The window was applied starting at the first break arrival time. The time length of this window was held constant between the tests to guarantee that repeatable energy quantities were compared between the specimens. The resulting windowed trace, x(n), was padded with zeros to 1024 points, and then Fourier Transformed to obtain the spectral frequency data, X(f), as follows:

$$X(f) = \sum_{n=1}^{N} x(n+1) \bullet (e^{-j(2\pi/N)})^{fn} \qquad (4.1)$$

where n are the data point time steps and k are the frequencies.

Peak frequencies were measured directly from the spectral data. They are listed in Tables 4.1 and 4.2 for P-waves and S-waves respectively. Values at all measured stress levels are presented, with units of kilohertz. Frequency resolution is ~20 kHz. For comparison, the peak frequencies of the input signals were ~800 kHz and ~525 kHz for P-waves and S-waves respectively. Peak frequencies that appear to be higher at the lowest stress as opposed to the middle stresses are presumed to be artifacts of low signal to noise ratios at low stresses. P-wave peak frequencies show some variability between specimens

Test	2.46	3.69	4.92	6.15	7.38	8.61	9.84	11.07	12.3	13.53	14.76
Clean, Dry	351.91	351.91	195.5	244.38	293.26	322.58	351.91	381.23	420.33	430.11	459.43
Clay-coated, Oven-dry	449.66	195.5	234.6	254.15	293.26	312.81	391.01	430.11	391.01	430.11	488.76
Clay-coated, Desiccator-Dry	195.5	175.95	195.5	215.05	254.15	234.6	254.15	251.15	293.26	391.01	449.66
Clay-coated, 50% water-content	175.95	195.5	215.05	234.6	273.7	293.26	332.36	410.56	430.56	410.56	449.66
Clay-coated, 80% water-content	175.95	58.651	195.5	175.95	195.5	215.05	215.05	215.05	234.6	254.15	273.7
Clay-coated, 140% water-content	-	156.4	175.95	175.95	195.5	175.95	195.5	195.5	195.5	195.5	215.05
Clay-coated, 200% water-content	156.4	175.95	195.5	215.05	215.15	273.7	-	312.81	351.91	410.56	430.11
Clay-coated, 300% water-content	-	195.5	195.5	215.05	215.05	254.15	293.26	312.81	332.36	332.36	371.46
Clean, 2.4% water-content	332.36	332.36	332.36	136.85	195.5	215.05	234.6	273.7	273.7	273.7	293.26
Clay-coated, 50% hexadecane-content	293.26	215.05	215.05	195.5	234.6	234.6	273.7	273.7	312.81	351.91	371.46
Clay-coated, 200% ethyl alcohol-content	-	215.05	175.95	215.05	215.05	234.6	234.6	273.7	312.81	371.46	391.01

Table 4.1: P-wave peak frequency data for seismic tests on glass bead specimens. Data are given in units of kiloHertz, with resolution of ~20 kHz.

Test	2.46	3.69	4.92	6.15	7.38	8.61	9.84	11.07	12.3	13.53	14.76
Clean, Dry	391.01	234.6	234.6	273.7	283.48	293.26	303.03	312.81	322.58	322.58	312.81
Clay-coated, Oven-dry	332.36	215.05	234.6	234.6	234.6	254.15	254.15	273.7	273.7	273.7	273.7
Clay-coated, Desiccator-Dry	175.95	234.6	254.15	254.15	273.7	273.7	273.7	293.26	293.26	293.26	293.26
Clay-coated, 50% water-content	215.05	234.6	254.15	254.15	254.15	273.7	273.7	273.7	273.7	273.7	273.7
Clay-coated, 80% water-content	205.28	215.05	234.6	234.6	234.6	234.6	254.15	254.15	254.15	254.15	273.7
Clay-coated, 140% water-content	175.95	205.28	215.05	215.05	234.6	254.15	234.6	234.6	254.15	254.15	254.15
Clay-coated, 200% water-content	215.05	224.83	234.6	254.15	254.15	254.15	254.15	273.7	273.7	-	273.7
Clay-coated, 300% water-content	166.18	215.05	234.6	254.15	234.6	254.15	254.15	254.15	273.7	273.7	273.7
Clean, 2.4% water-content	-	-	-	283.48	234.6	234.6	234.6	234.6	254.15	273.7	273.7
Clay-coated, 50% hexadecane-content	185.73	195.5	215.05	215.05	234.6	234.6	254.15	254.15	254.15	273.7	273.7
Clay-coated, 200% ethyl alcohol-content	175.95	234.6	234.6	254.15	254.15	254.15	254.15	273.7	273.7	273.7	273.7

Table 4.2: S-wave peak frequency data for seismic tests on glass bead specimens. Data are given in units of kiloHertz, with resolution of ~20 kHz.

at constant stress levels. S-wave peak frequencies are very consistent between the specimens at constant stress levels.

Attenuation coefficients and quality factors, measures of the energy loss per unit distance and per cycle respectively, required calculation. Repeatability tests indicated that small changes in source signal strength occurred between tests. Therefore, the method of spectral amplitude ratio comparison between the glass bead specimen and an aluminum standard was chosen (Toksöz et al., 1979; Tang et al., 1990). This method corrects for variations in the source. The data from aluminum standards measured directly after the specimen tests were used in the following equations:

$$\alpha_S(f) = \alpha_{AL}(f) + \frac{1}{L}\ln\left(\frac{|U_{AL}(f)|}{|U_S(f)|}\right) + \frac{1}{L}\ln\left(\frac{|G_S(f)|}{|G_{AL}(f)|}\right) \qquad (4.2)$$

$$Q_S(f) = \frac{\pi f}{\alpha_S C_S}$$

where α is the attenuation coefficient, L the length of the sample, U the spectral amplitude, f the frequency, G the geometrical spreading factor and C the velocity. Subscript S refers to the glass bead specimen; subscript AL the aluminum standard. Geometrical spreading factors were computed using the method of Bass (1958) and found to vary by only 4 percent for the glass bead specimens and aluminum standards in this laboratory work. Since this term is similar to experimental variability, it was neglected in the data reductions.

Quality factors at the individual trace peak frequencies were used in the figures for comparison between the specimens. Quality factors at a single frequency are given in Tables 4.3 and 4.4 for P-waves and S-waves respectively. The frequency for P-waves equaled ~370 kHz, a central peak frequency for the set of spectra at the highest stress, 14.7

Test	2.46 MPa	3.69 MPa	4.92 MPa	6.15 MPa	7.38 MPa	8.61 MPa	9.84 MPa	11.07 MPa	12.30 MPa	13.53 MPa	14.76 MPa
Clean, Dry	6.11	6.64	6.95	10.81	12.12	13.41	15.73	17.73	19.32	20.04	21.86
Clay-coated, Oven-dry		8.46	8.73	9.24	10.03	10.59	11.74	11.87	12.60	12.80	13.17
Clay-coated, Desiccator-Dry	6.56	-	8.42	-	10.4	-	10.9	-	12.14	-	13.6
Clay-coated, 50% water-content	7.24	7.39	8.31	9.00	10.06	10.27	10.52	11.21	11.42	-	-
Clay-coated, 80% water-content	6.19	4.19	6.85	6.38	6.93	7.64	7.77	8.03	8.64	8.92	9.40
Clay-coated, 140% water-content			5.62	5.36	5.79	6.15	6.70	6.46	6.85	7.25	7.65
Clay-coated, 200% water-content	5.83	5.75	7.36	7.81	8.22	9.55	-	10.62	11.13	11.88	12.45
Clay-coated, 300% water-content	-	7.47	6.95	8.16	8.05	9.14	10.25	10.66	11.09	-	-
Clean, 2.4% water-content						8.36	8.01	7.78	8.33	8.91	8.73
Clay-coated, 50% hexadecane-content	6.50	8.27	7.70	8.11	8.30	9.30	10.49	10.39	10.82	11.85	12.40
Clay-coated, 200% ethyl alcohol-content	5.96	6.95	6.16	7.26	7.27	7.69	8.08	8.52	8.99	9.59	10.18

Table 4.3: P-wave quality factor data at a frequency of ~370 kHz for seismic tests on glass bead specimens. The frequency corresponds to a mid-value for the set of tests at the highest frequency.

Test	2.46 MPa	3.69 MPa	4.92 MPa	6.15 MPa	7.38 MPa	8.61 MPa	9.84 MPa	11.07 MPa	12.30 MPa	13.53 MPa	14.76 MPa
Clean, Dry	12.89	17.65	18.30	28.27	34.02	34.09	35.04	36.13	37.62	43.60	43.66
Clay-coated, Oven-dry	7.17	11.00	13.78	15.05	16.07	18.04	19.16	21.54	22.70	25.01	24.96
Clay-coated, Desiccator-Dry	7.47	11.73	15.01	16.64	17.97	20.60	22.17	25.57	27.36	30.90	31.16
Clay-coated, 50% water-content	12.01	13.22	14.45	16.41	16.00	16.44	19.31	20.55	21.25	21.81	22.60
Clay-coated, 80% water-content	9.00	10.35	11.05	11.59	12.83	13.31	14.41	15.58	16.27	17.00	17.98
Clay-coated, 140% water-content	7.42	8.51	9.59	10.73	11.37	11.13	12.75	13.74	14.69	15.54	16.10
Clay-coated, 200% water-content	9.38	10.16	11.90	13.62	14.74	16.14	17.79	19.16	20.00	-	22.84
Clay-coated, 300% water-content	9.24	8.47	7.90	13.26	13.72	15.26	15.90	17.31	18.78	19.72	20.55
Clean, 2.4% water-content				9.27	14.23	15.18	16.30	17.25	18.79	20.01	21.22
Clay-coated, 50% hexadecane-content	7.56	9.65	11.22	12.22	13.73	14.81	16.20	16.85	17.56	18.27	19.40
Clay-coated, 200% ethyl alcohol-content	8.61	9.90	10.69	11.79	12.84	13.84	15.00	15.98	17.08	18.11	19.12

Table 4.4: S-wave quality factor data at a frequency of ~270 kHz for seismic tests on glass bead specimens. The frequency corresponds to a mid-value for the set of tests at the highest frequency.

MPa. The frequency for S-waves equaled ~270 kHz, a central peak frequency for the spectra at the highest stress.

4.3 Effect of Stress

Each glass bead specimen exhibited consistent changes in seismic wave propagation as stress was varied. Figures 4.3 through 4.6 present these changes for a dry, clean bead specimen and a clay-coated specimen with 80 percent water content. The glass bead specimens show considerable variation with stress in comparison to crystalline and consolidated rock samples. Both the velocities and the amplitudes of the transmitted pulse increase as stress increases. In the spectral domain, the peak frequencies and spectral amplitudes also increase as stress increases. The dry, clean bead specimen had larger overall and relative changes than the clay-coated specimen. For both specimens, peak frequency changes for P-waves are larger than for S-waves.

These trends indicate that the specimen is stiffening as stress increases. In granular material at low stresses, this behavior is often attributed to closure of microcracks (Birch and Bancroft, 1938; Gardner *et. al.*, 1964; Gordon and Davis, 1968; Toksöz *et. al.*, 1979). This cannot be the case in this material since few microcracks exist. However, in unconsolidated materials with non-welded contacts, grain-to-grain contacts can be affected by stress. As stress increases so does both the number of contacts and the area of each contact. Both of these changes will lead to higher overall stiffnesses and better seismic wave transmission.

The three contact stiffness models developed in Section 2.3.1 are applied to investigate the effect of stress on grain-to-grain contacts. The effective modulus model

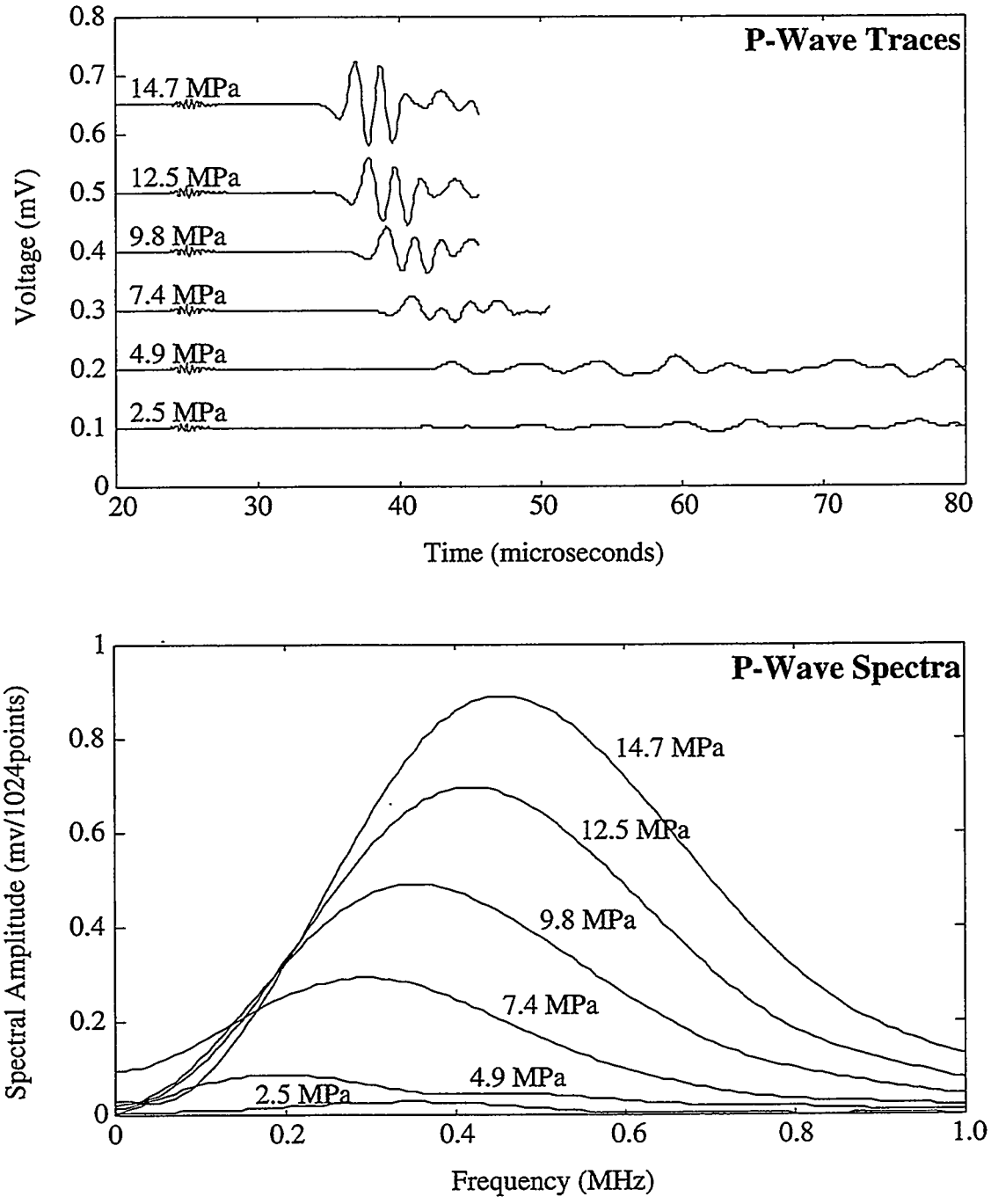

Figure 4.3: P-wave (a) traces and (b) spectra for dry, clean bead specimen. Velocities and magnitudes of the traces increase with increasing stress. Spectral amplitudes and peak frequencies also increase with increasing stress.

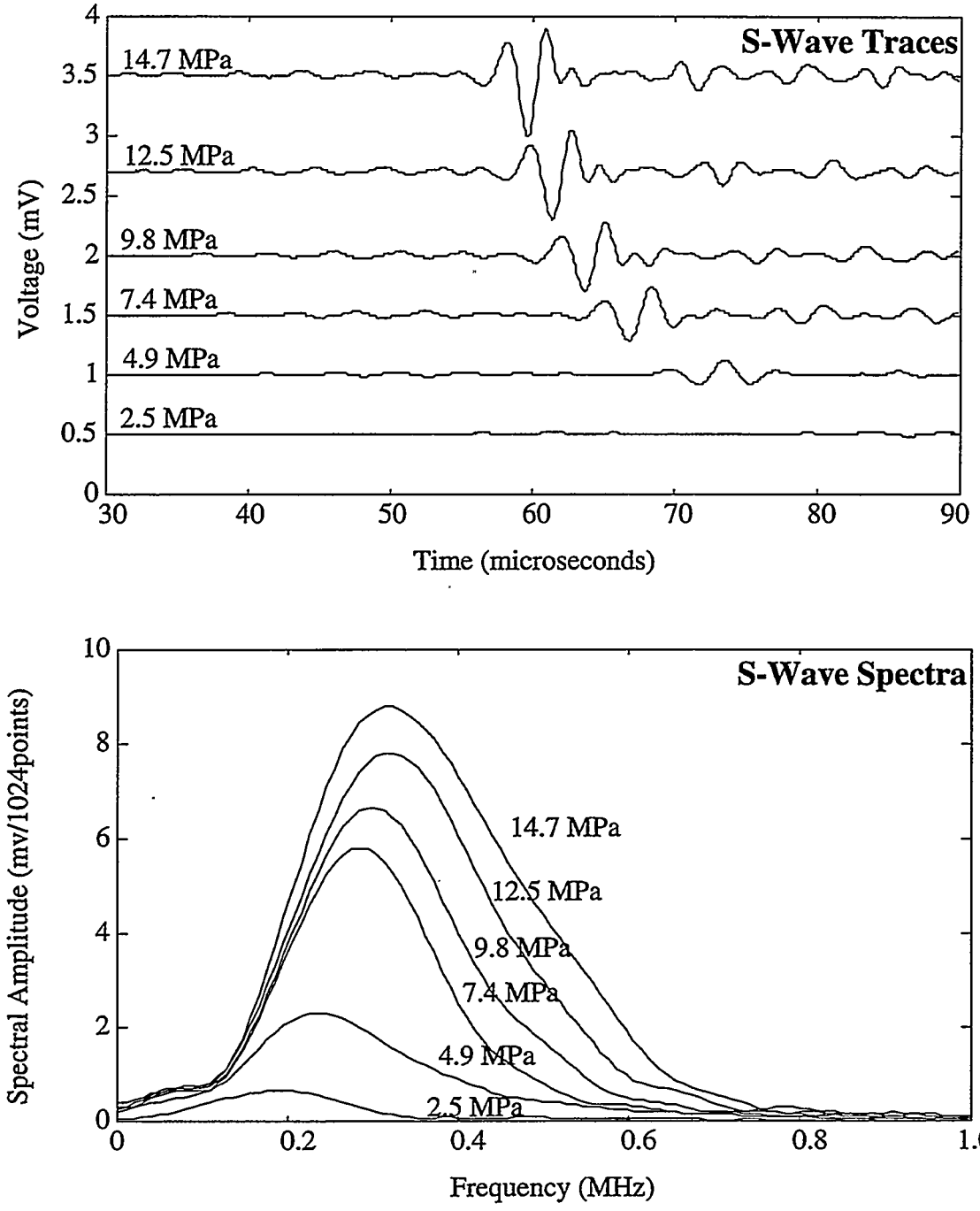

Figure 4.4: S-wave (a) traces and (b) spectra for dry, clean bead specimen. Velocities and magnitudes of the traces increase with increasing stress. Spectral amplitudes and peak frequencies also increase with increasing stress.

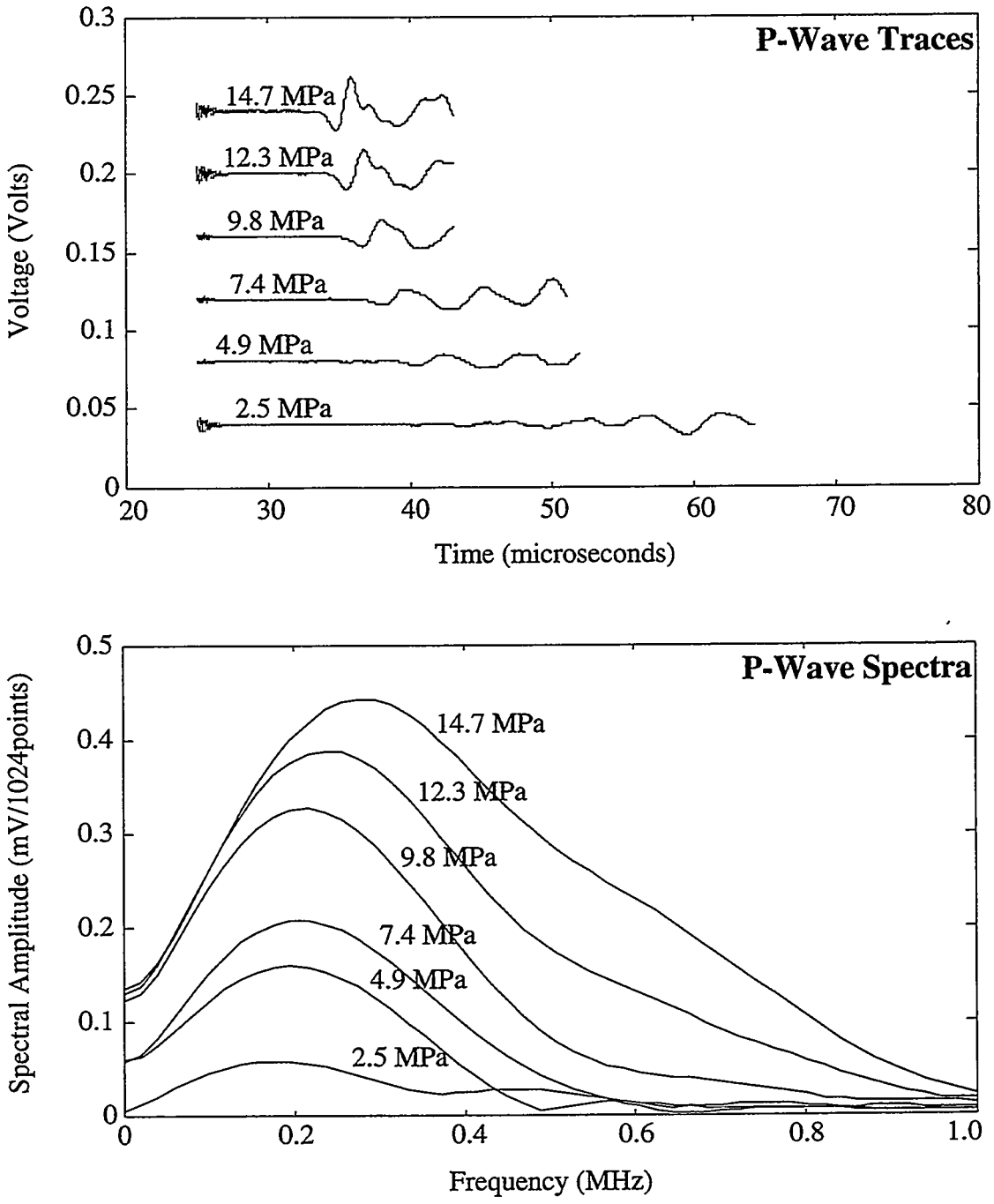

Figure 4.5: P-wave (a) traces and (b) spectra for 80 percent clay water content bead specimen. Velocities and magnitudes of the traces increase with increasing stress. Spectral amplitudes and peak frequencies also increase with increasing stress. Note that the scales are smaller than Figure 4.3.

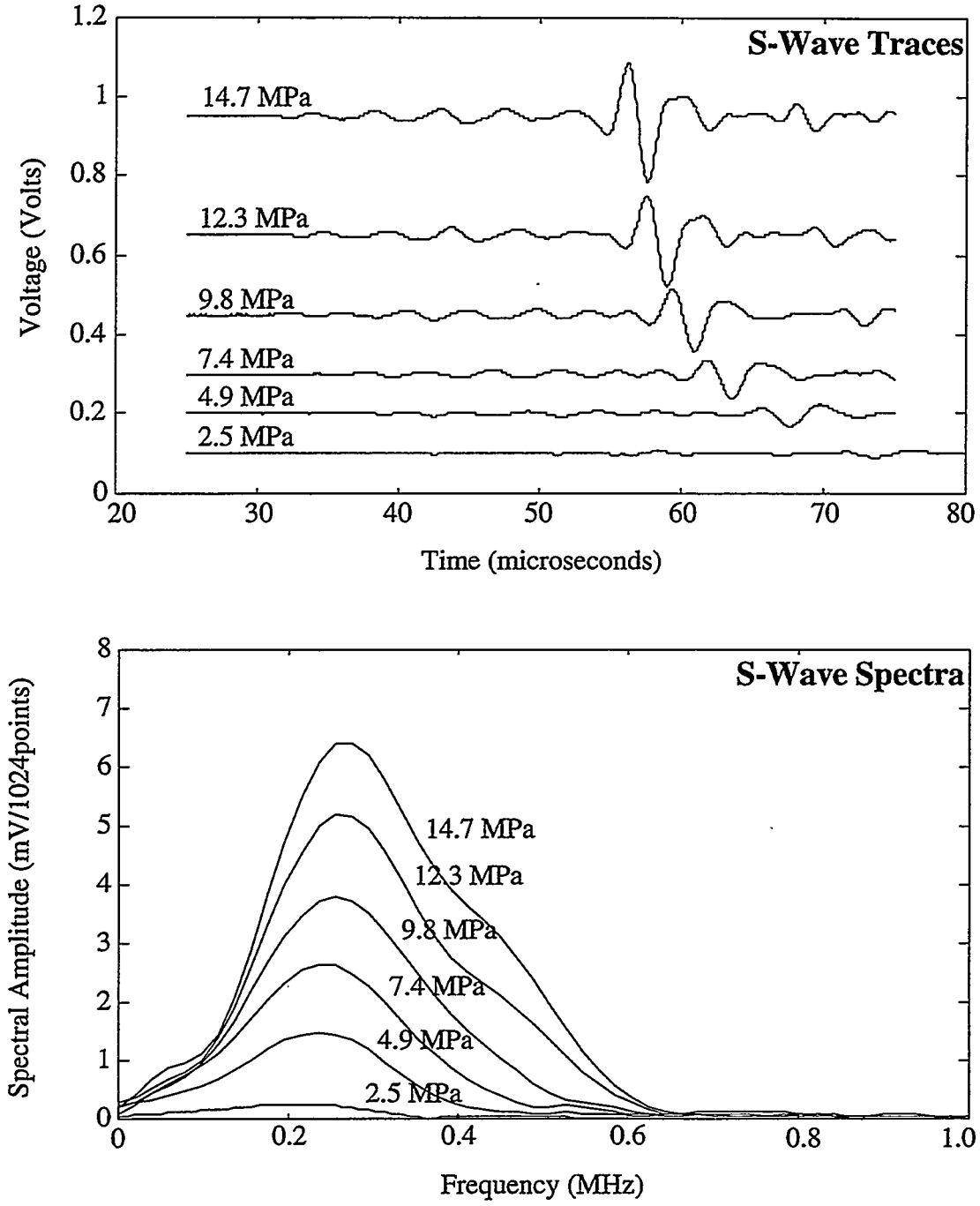

Figure 4.6: S-wave (a) traces and (b) spectra for 80 percent clay water content bead specimen. Velocities and magnitudes of the traces increase with increasing stress. Spectral amplitudes and peak frequencies also increase with increasing stress. Note that the scales are smaller than Figure 4.4.

approximates a set of contacts as a planar interface. P-wave and S-wave velocities are separately input to obtain contact stiffnesses, using equation 2.18. Grain contacts are considered to be perfect spherical contacts in the Hertzian contact model. This model, equation 2.21, depends only on the value of stress. The modified effective modulus model allows for a random number of contacts per grain. For planar motion, the contact stiffnesses are calculated by inputting the P-wave velocities into equation 2.31. Both the P-wave and S-wave velocities are input into equation 2.34 to calculate the contact stiffnesses under triaxial strain.

Data from a clean dry specimen and a clay-coated 80 percent water content specimen are input into the appropriate equations to give the calculated stiffnesses shown in Figure 4.7. For each model, the stiffnesses increase as stress increases. This confirms that stress is increasing the stiffness of the grain contacts. Also, the contact stiffnesses for the clay-coated specimen are slightly higher than for the dry clean specimen, suggesting that clay stiffens the grain contacts.

The calculated stiffness are all within approximately an order of magnitude, but vary depending on model. Stiffnesses increase as the models become more complex. The highest values are for a random number of contacts under triaxial strain. More complex models typically account for fewer contacts, requiring the remaining contacts to have more resistance to motion. Since the number of contacts in the random packing of the specimen is likely to be less than the number in any ordered approximation, the contact stiffnesses in the actual specimens are likely to be larger than the values presented in Figure 4.7. For both specimens, contact stiffnesses are lowest for the effective modulus model with S-wave input indicating that the bead contacts are more compliant under shear motion than under compressional motion. The effective modulus model with P-wave input and

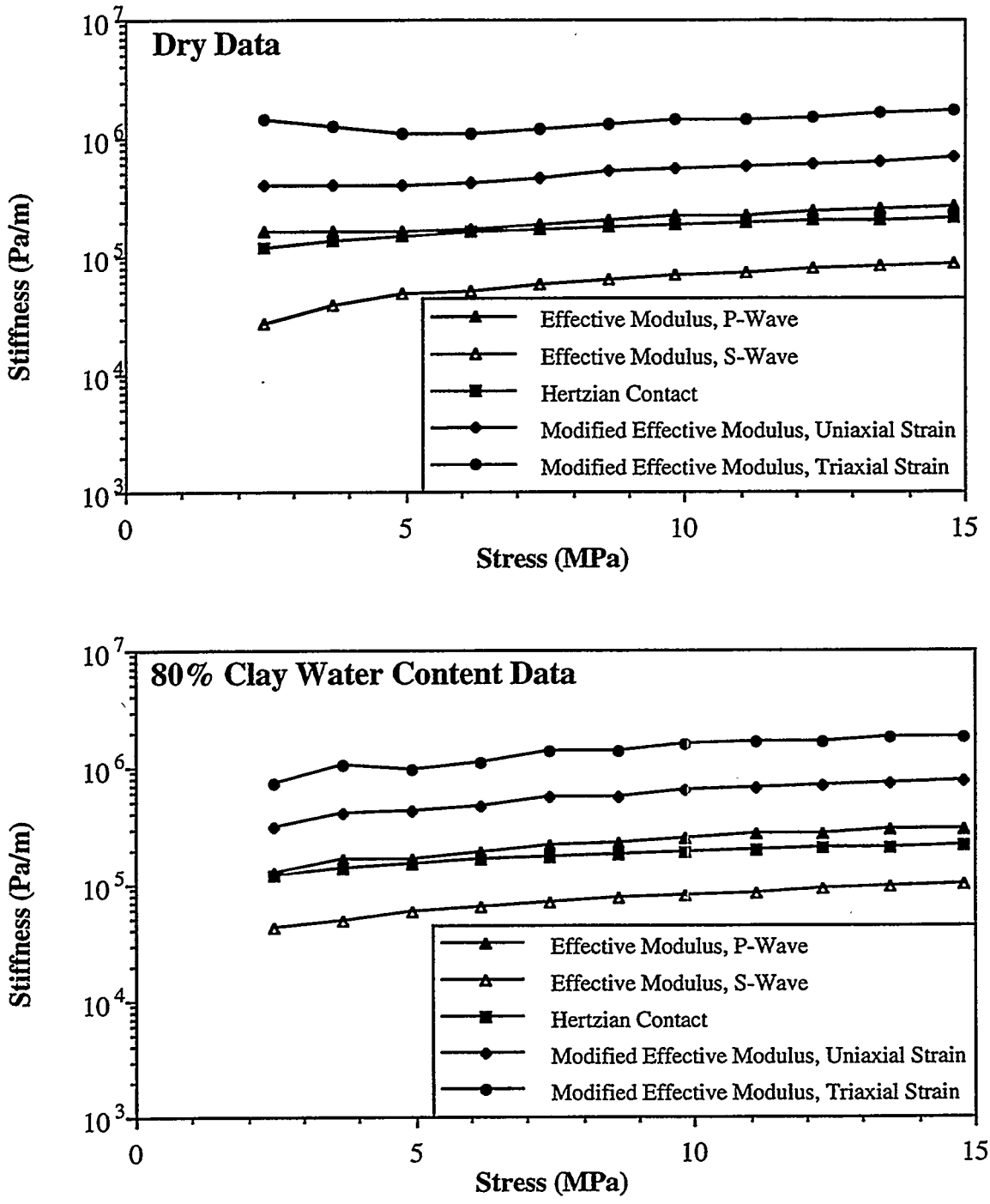

Figure 4.7: Calculated contact stiffnesses calculated for three different models: effective modulus, Hertzian contact, and modified effective modulus. The (a) clean dry and (b) 80% clay water content specimen data are shown. Stiffness increases with stress and with increasing refinements in the models.

Hertzian contact model estimate similar contact stiffnesses. This agreement can be attributed to the assumption of planar contact sets in both models.

Recent conceptual work based on thin sections has suggested that grain contacts can have an important influence on seismic velocities (Anstey, 1991). The data presented here confirm the importance of grain contacts and grain contact stiffnesses to the seismic velocities and attenuation of poorly cemented and unconsolidated materials.

4.4 Effect of Clay-Coating

The preceding data suggests that the presence of clay significantly affects seismic wave propagation. Comparison of the spectra in Figures 4.3 through 4.6 shows that the clean beads have larger spectral amplitudes and peak frequencies than the 50 percent water content clay-coated beads. In addition, the calculated contact stiffnesses were higher for the clay-coated beads in Figure 4.7.

The effect of clay-coating the glass beads is examined rigorously in two sets of tests. Clean and clay-coated beads are first compared under dry conditions. Both oven-dry and desiccator-dry clay-coated specimens are studied. In the second set of tests, clean and clay-coated beads are compared at 2.4 percent specimen water contents. This corresponds to a 300 percent clay water content for the clay-coated specimen.

Figure 4.8 shows the group velocities at dry conditions. The desiccator dry specimen group velocities are larger at nearly all stress levels than the other two specimen group velocities for both P-waves and S-waves. The oven-dry clay-coated group velocities are similar to dry clean group velocities for P-waves, but larger than dry clean beads for S-

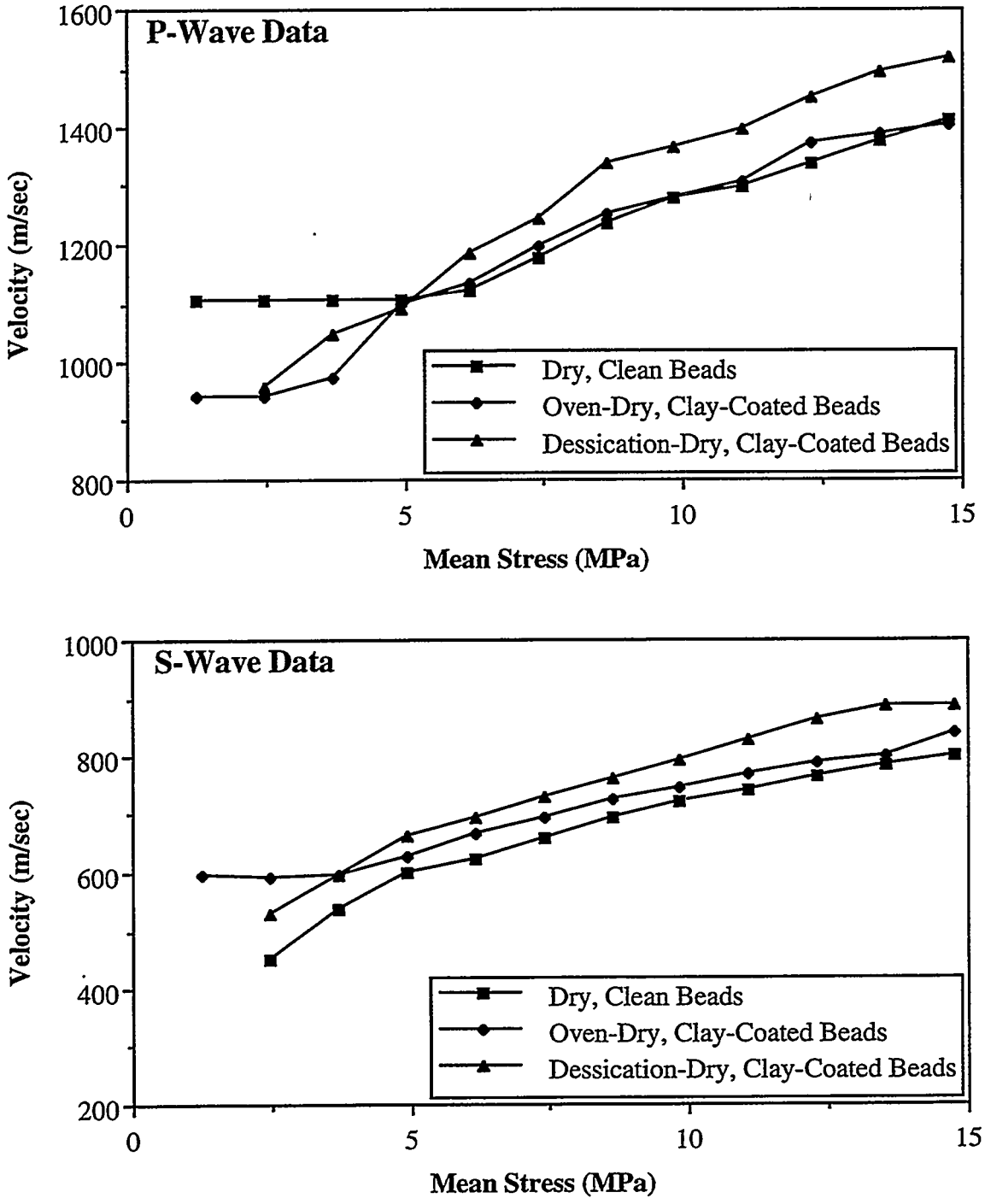

Figure 4.8: (a) P-wave and (b) S-wave velocity data for dry bead specimens with and without clay coatings. It can be seen that the clay coating increases the velocities, indicating that clay adds stiffness to the grain contacts. Desiccator-dry clay has higher shear stiffness than oven-dry clay. This can be attributed to structural changes in the clay during oven drying.

waves. The dry clean P-wave group velocities below 5 MPa and oven-dry clay-coated S-wave group velocities below 3.5 MPa appear to be independent of stress.

The quality factor data at individual spectral peak frequencies for the dry tests are presented in Figure 4.9. For these data, the dry clean beads have significantly larger values at higher stresses than for the other two tests. At and below 5 MPa stress, the clean dry values are smaller for P-waves and only slightly higher for S-waves. At all stresses, oven-dry clay-coated and desiccator-dry clay-coated quality factors are similar for P-waves. For S-waves, the desiccator-dry clay-coated values are larger.

The P-wave peak frequency data, presented in Table 4.1, vary slightly from these trends. In general they are highest for oven-dry clay-coated beads, though there is some interchange with the clean dry beads. The desiccator-dry clay-coated P-wave peak frequencies are lower. The peak frequencies for S-waves, presented in Table 4.2, are largest for the clean dry beads, followed by the desiccator-dry clay-coated and the oven-dry clay coated beads respectively. The S-wave data follow the quality factor trends.

The group velocities for tests at 2.4 percent specimen water content are given in Figure 4.10. Similar to the dry conditions, the specimens with clay have notably larger group velocities for most P-wave stresses and all S-wave stresses. At and below 7.5 MPa, the clean wet P-wave group velocities appear to be independent of stress. In this same range, the wet clay-coated group velocities drop below the clean wet values.

Figure 4.11 presents the quality factors calculated at individual spectral peak frequencies for the 2.4 percent water content specimens. Because of noise, quality factors could not be calculated for the clean wet specimens at low stresses. At higher stresses, the P-wave clean wet values are significantly larger than for the clay-coated specimen. In

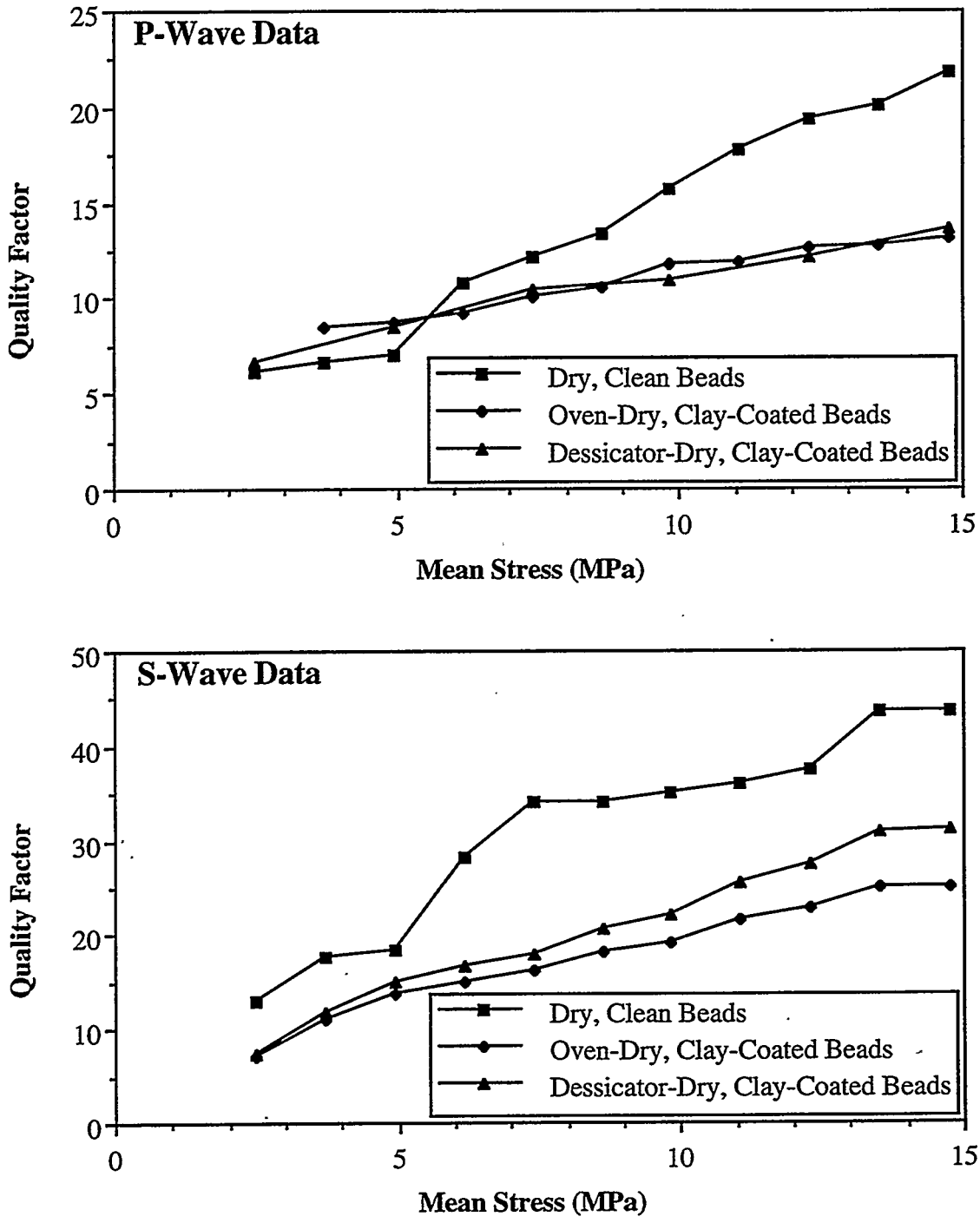

Figure 4.9: P-wave and S-wave quality factor data at individual spectra peak frequencies for dry bead specimens with and without clay coatings. The clay coating decreases the quality factor, with the desiccator-dry clay having higher shear stiffness than oven-dry clay. The difference can be attributed to structural changes in the clay during oven drying.

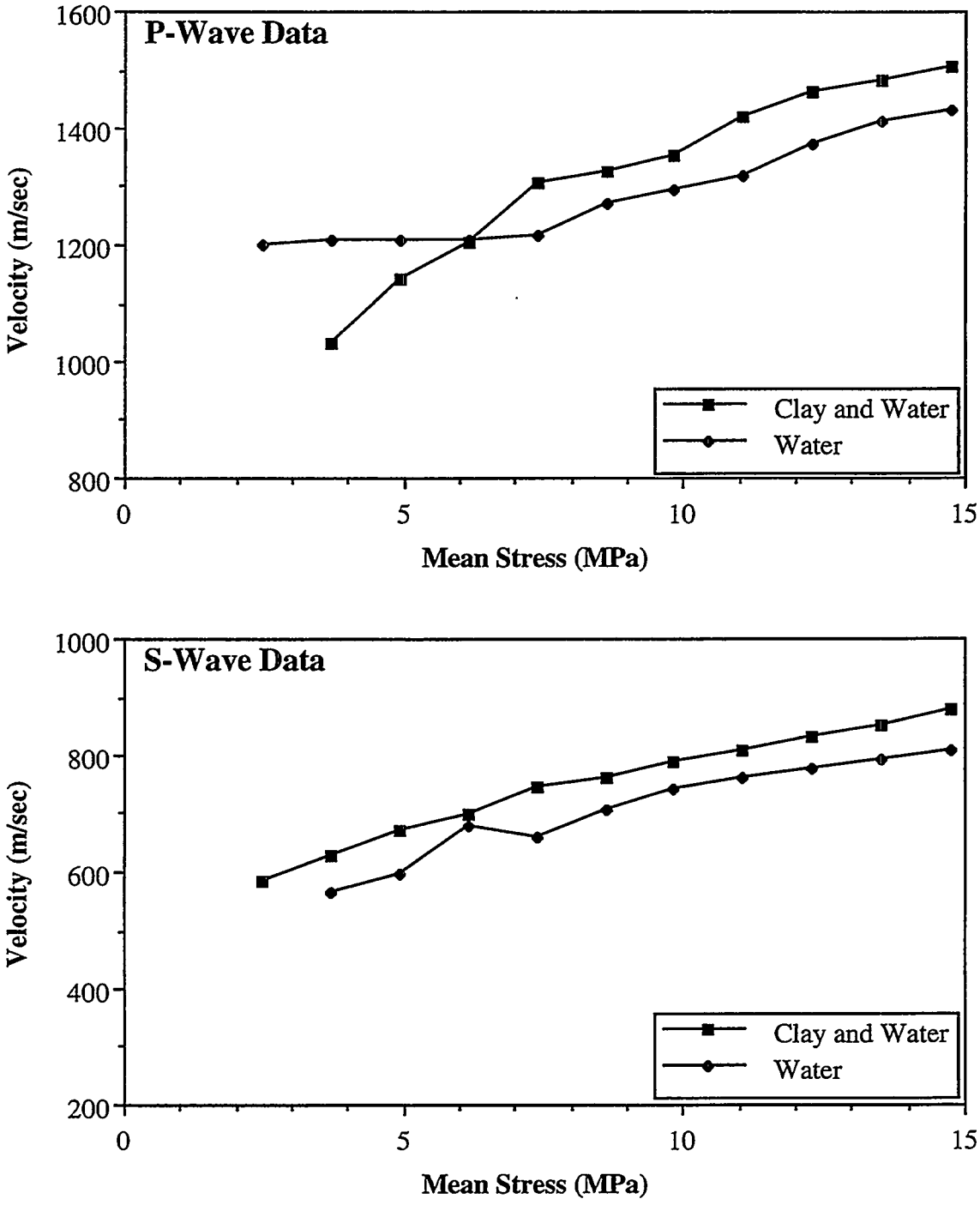

Figure 4.10: (a) P-wave and (b) S-wave velocity data for bead specimens with 2.4 percent specimen water content (weight water/weight specimen), equivalent to 300 percent clay water content (weight water/weight clay). The clay-coating increases the velocities due to the higher stiffness for the clay-water mixture than for water alone.

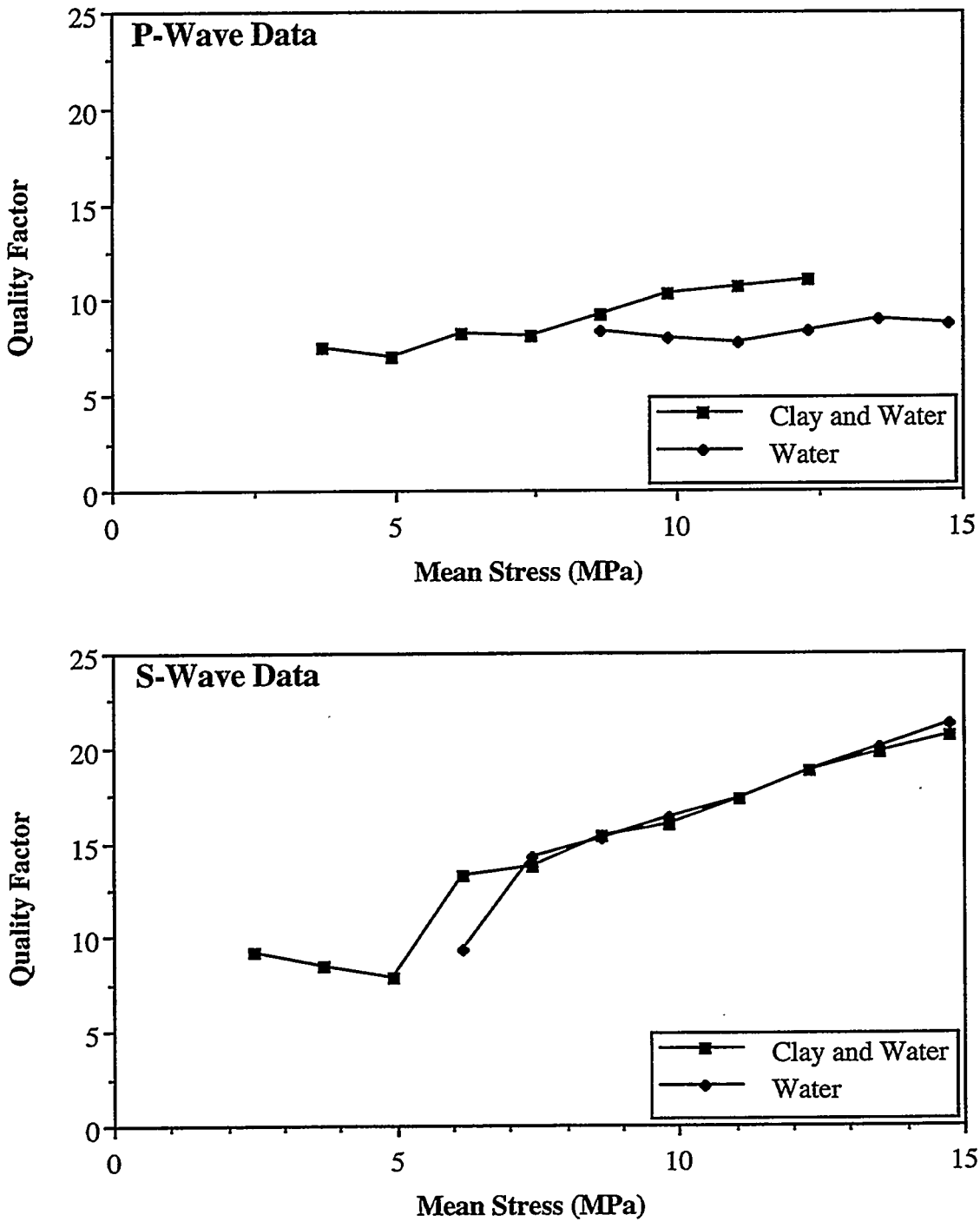

Figure 4.11: (a) P-wave and (b) S-wave quality factor data at individual spectra peak frequencies for bead speciemens with 2.4 percent specimen water content (weight water/weight specimen), equivalent to 300 percent clay water content (weight water/weight clay). The clay-coating increases the P-wave quality factor over just water alone; the S-wave quality factors are equivalent.

contrast to both the wet P-wave, dry P-wave, and dry S-wave trends, the wet S-wave clean bead quality factors are similar to wet clay-coated values at higher stresses. At 7.5 MPa, the S-wave clean wet quality factor is notably lower than clay-coated wet value.

The P-wave peak frequencies, given in Table 4.1, are in contrast to the quality factor trend. The P-wave clay-coated wet peak frequencies are larger than the clean wet peak frequencies. These trends can be attributed to the different viscosities at the grain contacts. Clay has a higher viscosity and therefore transmits higher frequencies but also dissipates more energy. The S-wave peak frequencies (Table 4.2) are similar for the two wet tests in agreement with the quality factor data.

The data clearly show that the presence of clay at grain contacts directly affects seismic wave propagation. At the higher stresses, the addition of clay increases the group velocities and concurrently decreases the quality factors, i.e. increases the attenuation. These trends can be attributed to the rheologic nature of clay. Because of clay's structure, clay at a contact will increase both the stiffness and the viscosity of that contact. The change in stiffness changes the group velocity and attenuation of the propagating seismic wave. A stiffer contact increases the group velocity, decreases the attenuation, and increases the peak frequency of the propagating wave. A change in viscosity does not affect the group velocity, but does change the attenuation of the propagating wave. A more viscous contact converts more energy to heat, thereby increasing the attenuation of the propagating wave.

At the lowest stress levels, the clay in general increases the quality factors or decreases the attenuation of the propagating waves. The simplest interpretation is that the clay is increasing the number of contact by forming links between grains that are separated by small distances at these low stress levels. At higher stresses, these, the grains actually

make contact. The increased number of grains at low stresses facilitates seismic transmission.

The stress independence exhibited at low stresses by clean dry P-wave group velocities, oven-dry S-wave group velocities, and clean wet P-wave group velocities may be explained by three different scenarios. First, the small signal-to-noise ratio at the low stresses make it difficult to distinctly select the first-break arrival times of the directly transmitted waves. Thus, it may be that data is lost in noise and is not stress-independent. However, if the data are truly stress independent it could indicate that the number of contacts is independent of stress at low stresses. It may be that the structure of the glass bead specimens is such that the number of beads in contact does not change at low stresses. That is, beads separated by small distances do not come into contact until higher stresses. Another possibility is that the stress-independence is caused by water condensation. At room conditions, water condenses out of the atmosphere into the grain contacts due to capillary forces. This water may form a bridge or contact between beads separated by small distances; a contact that transmits seismic waves. The number of these water contacts may be constant at the low stresses.

The clay drying procedure has an effect on seismic wave propagation. Desiccation-drying results in faster group velocities for both waves and less S-wave attenuation than oven-drying. These differences appear to be a result of a collapse in clay structure upon oven drying, as discussed in Section 3.2.2.3. The oven-dry collapsed structure provides less stiffness at the contacts than the more dispersed desiccator-dry clay structure.

The agreement between the clean and clay-coated 2.4 percent specimen water content quality factors is in contrast to the trends from the dry tests and wet P-wave data. This is interpreted as an agreement in contact stiffness and viscosity, rather than lack of

effect upon clay addition. The clay in the clay-coated 2.4 percent specimen water content specimen may be hydrated past the liquid limit, which varies between 100 and 900 percent for montmorillonite (Mitchell, 1991). Past this limit, clay behaves more as a liquid than a plastic solid. Therefore, the clay at this high water content may be similar to a liquid coating.

These tests have confirmed that clay at grain contacts affects seismic wave propagation. Because of its structure, clay adds both a stiffness and viscosity to the contacts. In general, this increases the group velocity and also increases the attenuation of a propagating wave.

4.5 Effect of Water Content

Five specimens were prepared to test the effect of varying water content. The clay-coating was fixed at 0.8 percent weight content. The water content of the clay-coating varied from 50 to 300 percent (weight-water/weight-clay). The polar nature of water allows it to interact with the charged clay platelet particles, causing the clay to increase in volume. This swelling was expected to be significant because of the low salt concentration in the clay-water mixture. The changes in clay-coating viscosity as a result of the clay swelling were expected to affect the propagation of seismic waves.

Figure 4.12 shows the changes in group velocities as the water content varied. The variations in group velocities with stress are similar between the specimens, with more variability in the P-wave than the S-wave group velocities. For both P and S-wave group velocities, the 140 percent water content specimen data are consistently at the high end of the range while the 80 percent water content specimen data are at the low end of the range.

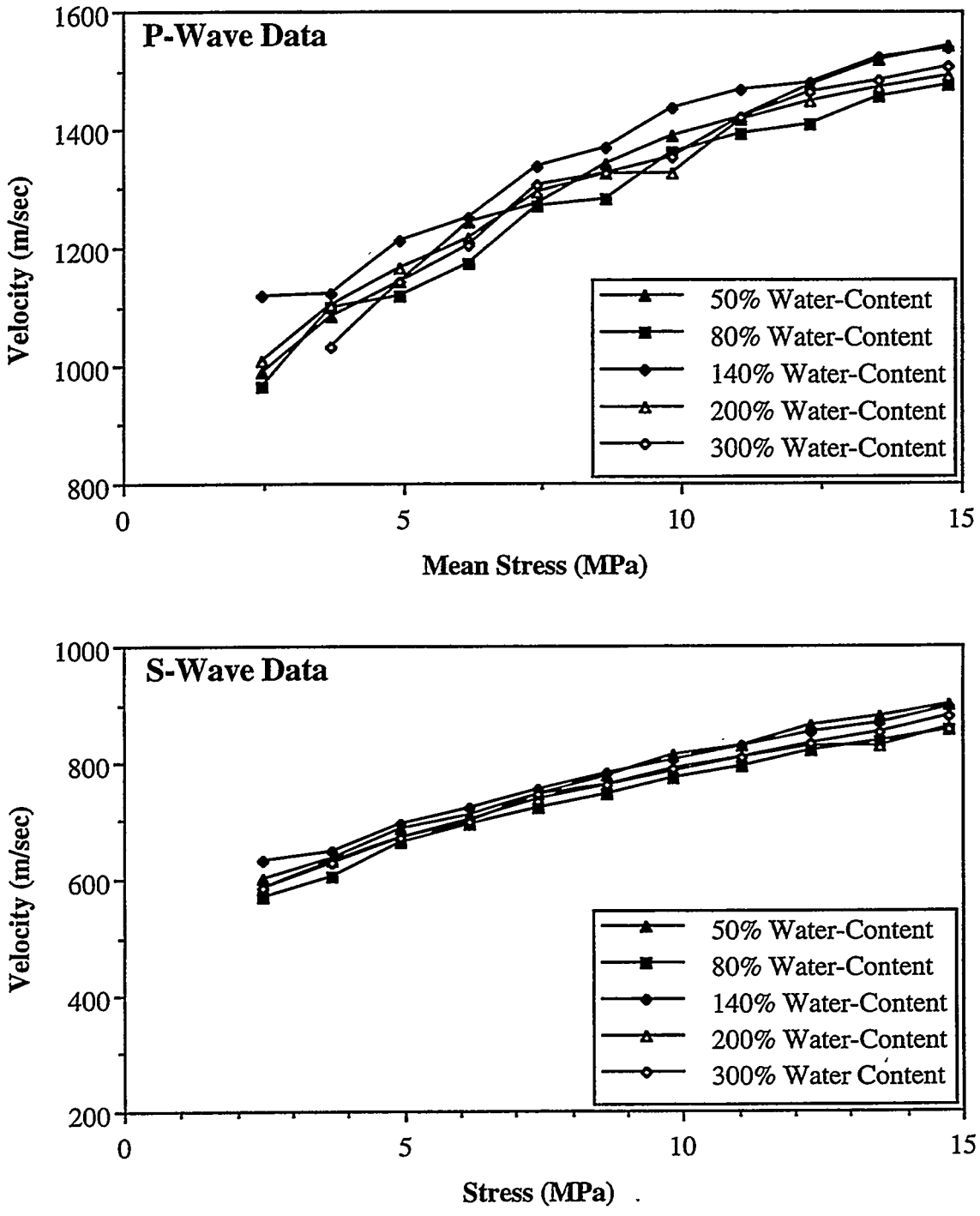

Figure 4.12: (a) P-wave and (b) S-wave velocity data for clay-coated bead specimens with varying clay water contents (weight water/weight clay). Note that the velocity scales are the same, but the ranges differ. The velocities are similar, weith more scatter in the P-wave than in the S-wave data.

These trends do not correlate with any known mechanisms and may indicate experimental variability due to uncertainty in specimen length measurements.

The quality factors calculated at individual spectral peak frequencies for the different water content specimens are shown in Figure 4.13. The data have similar general rankings for the two types of waves. The 50 percent water content specimen quality factors are the highest at all mean stress levels. The lowest water content data are followed by the 200 percent, 300 percent, 80 percent, and 140 percent specimen data respectively. The P-wave peak frequencies (Table 4.1) also follow this same trend. The S-wave peak frequencies (Table 4.2) have little variation between the different water contents.

The trends in the quality factor can be explained in two steps. This is schematically represented in Figure 4.14. First, as the clay water content increases from 50 percent to 80 percent to 140 percent, the clay-coating swells and becomes less viscous. This leads to a more dissipative layer between the grain-to-grain contacts, decreasing the transmitted amplitude. The increased transmission at 200 percent and 300 percent clay water contents can be related to a change in clay cohesion. Scratch tests show that up to 200 percent water content clay retains its structural cohesion and does not migrate when scratched (Figure 4.15). Above 200 percent water content, the clay looses some of its cohesion and flows when scratched. This suggests that at and above 200 percent water content, the clay-coating at the grain-to-grain contacts can flow in response to a force. Therefore, as the sample was stress loaded, localized stresses at the grain-to-grain contacts probably pushed the swelled clay toward the surrounding open pore space. This causes a toroidal clay mass to form around the contact, with a very thin clay-layer remaining at the contact. The larger contact area and smaller distance between grains lead to increased seismic transmission. The slightly lower values for 300 percent as opposed to 200 percent water content may be due to either lower viscosity clay or the presence of free water.

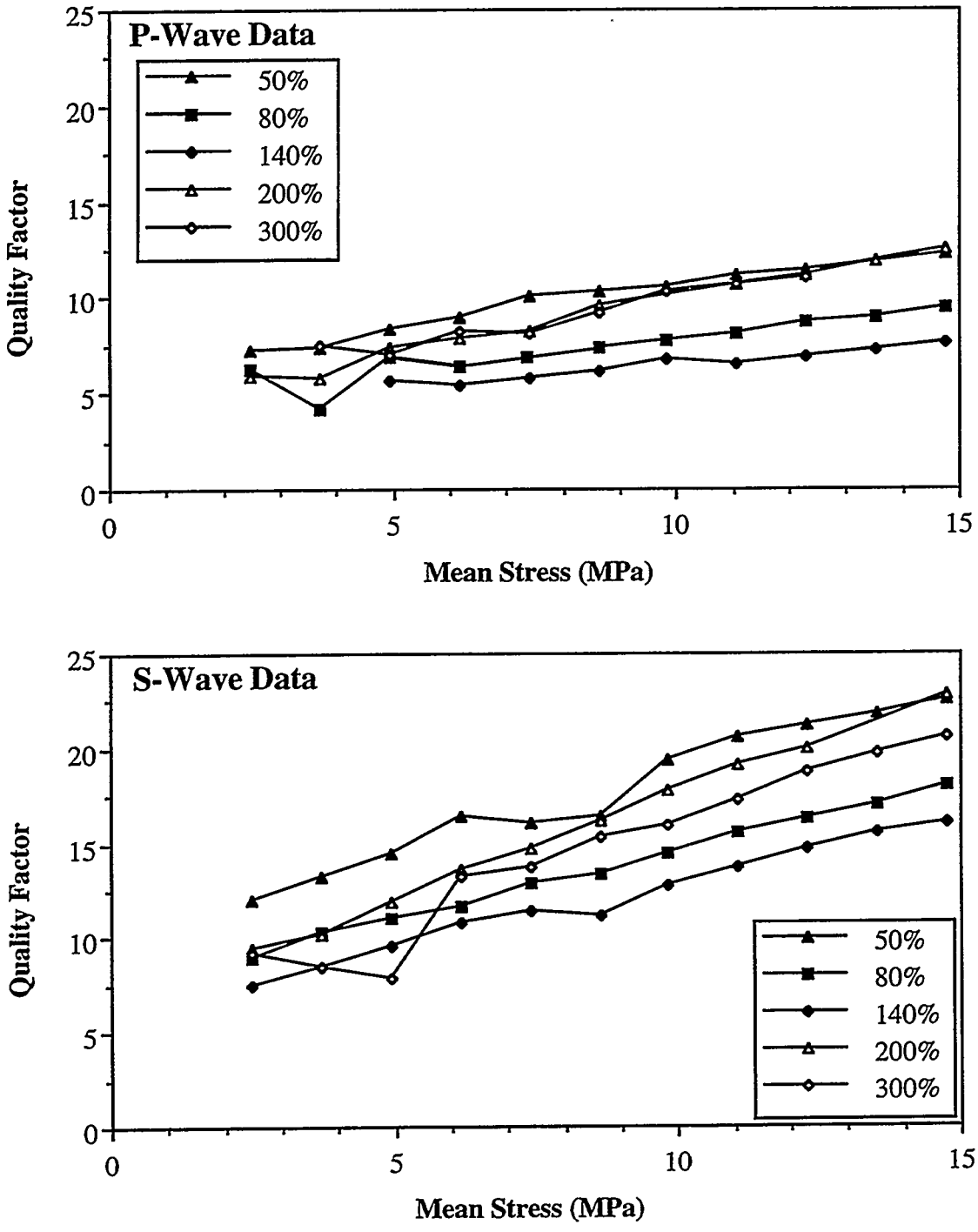

Figure 4.13: (a) P-wave and (b) S-wave quality factor data at individual spectra peak frequencies for clay-coated bead specimens with varying clay water contents (weight water/weight clay). Note that the water contents can be larger than 100 percent since water can absorb up to four times its weight in water. The quality factors initally decrease with increasing water content, then increase.

Proposed Clay-Coating Locations

Dry Clay

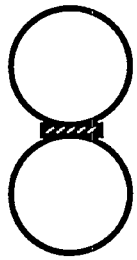

<200% Water Content

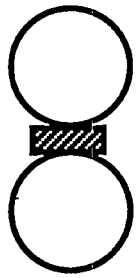

>200% Water Content

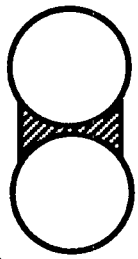

Figure 4.14: Proposed clay-coating locations for dry clay, less than 200 percent clay water content, and greater than 200 percent clay water content. Initially, as the clay absorbs wter it increases in volume, pushing apart the bead-to-bead contacts. Eventually, the clay passes the liquid limit, looses its structural cohesion, and is pushed from the contacts by stress cycling.

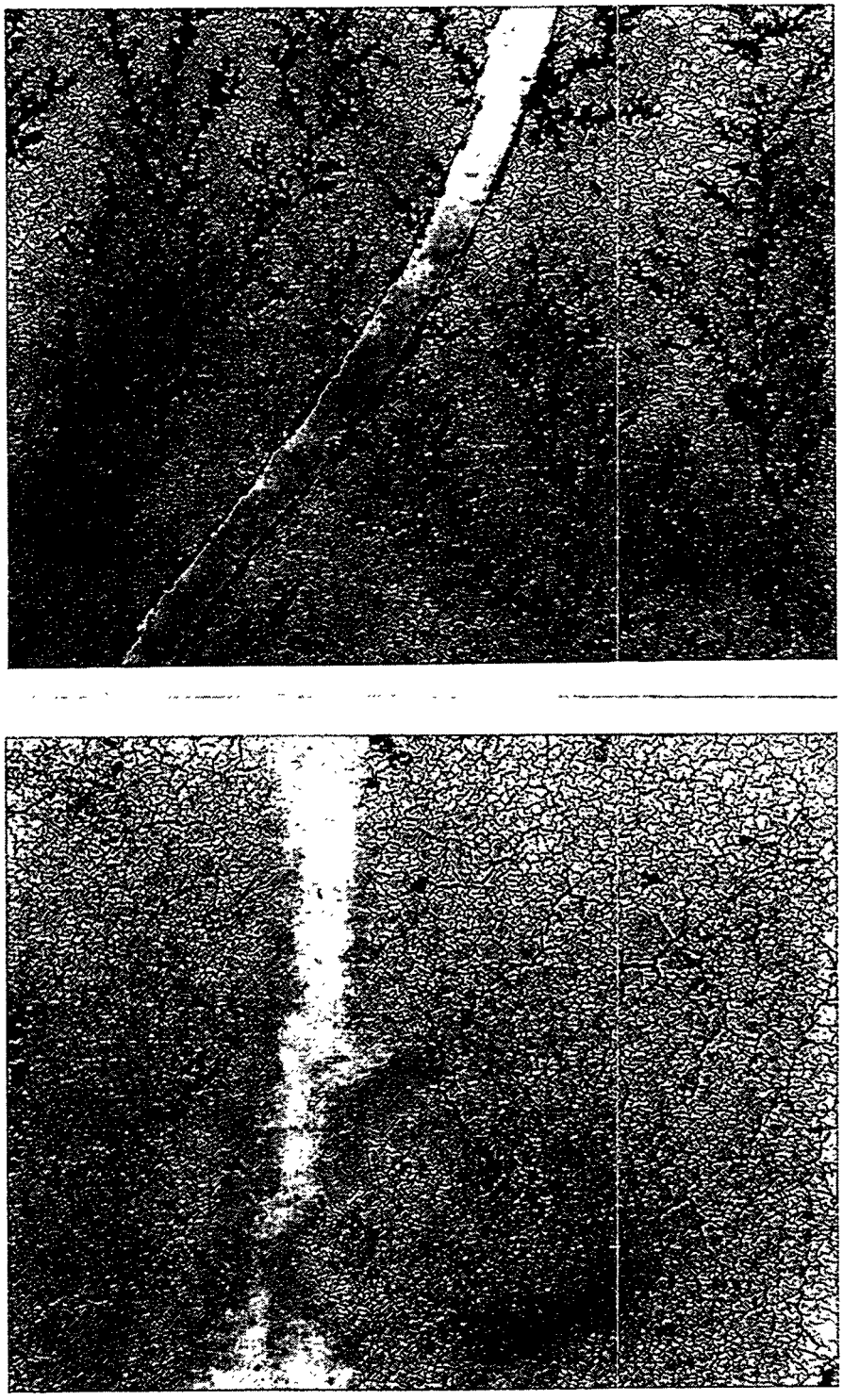

Figure 4.15: Scratch tests for sodium montmorillonite clay layers at (a) 24 percent clay water content and (b) 251 percent water content. The higher amount of water exceeds the plastic limit of clay, therefore it can migrate due to a lack of cohesion.

The similar trends in P-wave and S-wave quality factors may indicate similar loss mechanisms. P-wave losses can be attributed solely to a pumping mechanism, as shown in Figure 4.16a. Pumping losses are due to the visco-elastic movement of the clay at the contact. As the compressional wave moves through clay at the grain contacts in the direction of propagation, the clay can move into and retreat from the surrounding pore space. This pumping motion dissipates energy and attenuates the seismic energy. Pumping attenuation is distinct from squirt flow attenuation in that it is the result of mass deformation, not of fluid flow in response to a pressure gradient.

S-wave losses can be attributed to two mechanisms: viscous damping and pumping losses. As the shear wave moves through clay at the grain contacts in the direction of propagation, plastic movement between the clay platelets will cause viscous damping. Energy is dissipated by plastic movement between platelets, causing attenuation of the seismic wave (Figure 4.16b). The agreement in S-wave peak frequencies between all the specimens indicates that this occurs in all samples.

In addition, the propagating shear wave can also have losses due to the pumping mechanism at contacts off-angle to the direction of motion. Shear forces can be separated into two compressional opposing forces (Jaeger and Cook, 1969):

$$\tau = -\frac{1}{2}(\sigma_1 - \sigma_2)\sin 2\theta$$

where τ is the shear force, σ_i are the principal stress axes, and θ is the angle between the propagation plane and contact plane. Thus, the pure shear motion can be translated into perpendicular compressional tension stresses, each at an angle of 45° to the shear motion.

Attenuation Loss Mechanisms for Contacts in the Seismic Wave Propagation Direction

P-Wave Loss Mechanism: Pumping Loss

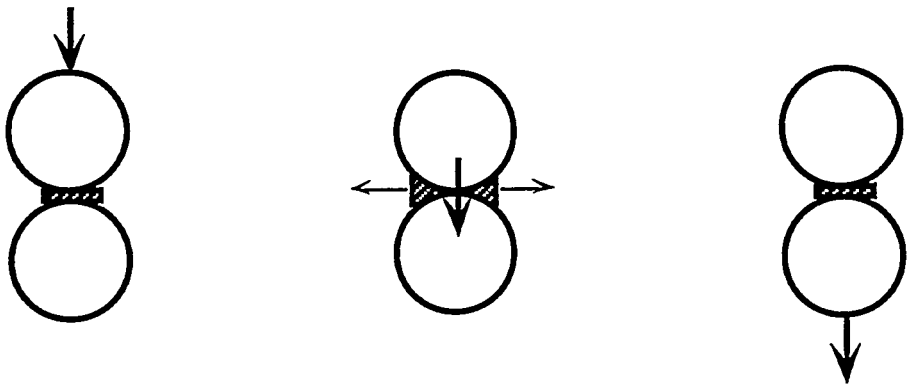

S-Wave Loss Mechanisms: Viscous Losses

Figure 4.16: Proposed attenuation loss mechanisms at contacts in the propagation direction for P-waves and S-waves. The circles represent the glass beads, the hatched areas the clay-coating, the bold arrows the propagating stresses or displacements, and the small arrows the clay motion. P-waves generate pumping losses (a) and S-waves generate viscous losses (b).

These compressional motions give rise to pumping losses at contacts that are at any angle to the direction of propagation, as shown in Figure 4.17.

The P-wave trends for the multiple grain-to-grain clay-coated contacts are in contrast to the results for a single planar clay-coated interface. Single interface results for a clay layer with ~160 percent clay water content are shown in Figure 4.18. The transmitted P-wave peak-to-peak amplitudes, a first order measure of attenuation and quality factor, appear independent of applied stress and have little attenuation. Multiple interface transmitted P-wave quality factors depend on stress and are significantly attenuated (Figure 4.13). The differences can be attributed to varying contact geometry. The planar contacts have a very small surface area perpendicular to wave motion. It is over this area that the clay bulges and retreats due to Poisson expansion during wave propagation, causing attenuation. Thus, pumping losses are very small at planar contacts. At point-to-point contacts, there is a large perpendicular surface area and consequently significant clay movement and pumping losses.

The agreement in the highest stress quality factors for the 50 percent and 200 percent specimens was investigated by examining the windowed traces and spectra. (Figures 4.19 and 4.20). The 50 percent clay water content windowed wave trace amplitudes are notably larger than the 200 percent clay water content amplitudes. The spectral data are in close agreement at the lower range of frequencies. At the higher frequency range, the 50 percent clay water content specimen spectral amplitudes are larger than the 200 percent clay water content specimen spectral amplitudes. This confirms that at the highest stress, the 50 percent specimen seismic transmission is larger than the 200 percent specimen transmission in agreement with the other stress levels.

Attenuation Loss Mechanisms for Contacts at Angles to the Seismic Wave Propagation Direction

Shear motion translation:

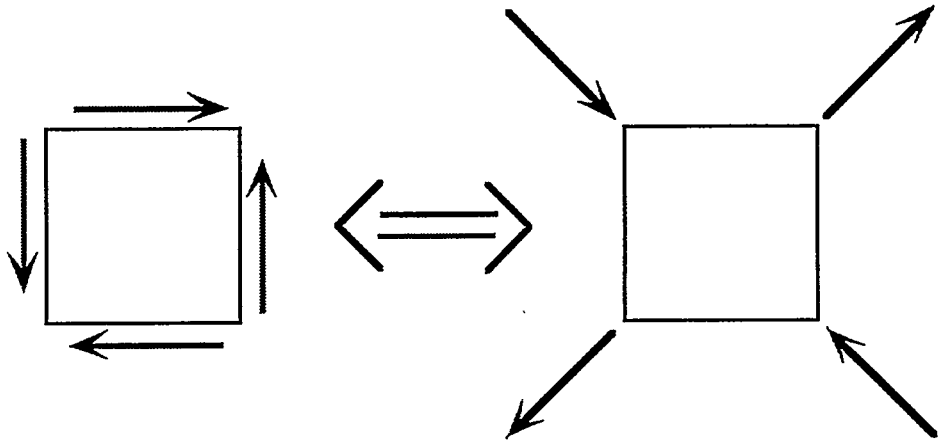

S-Wave Loss Mechanism: Pumping Loss

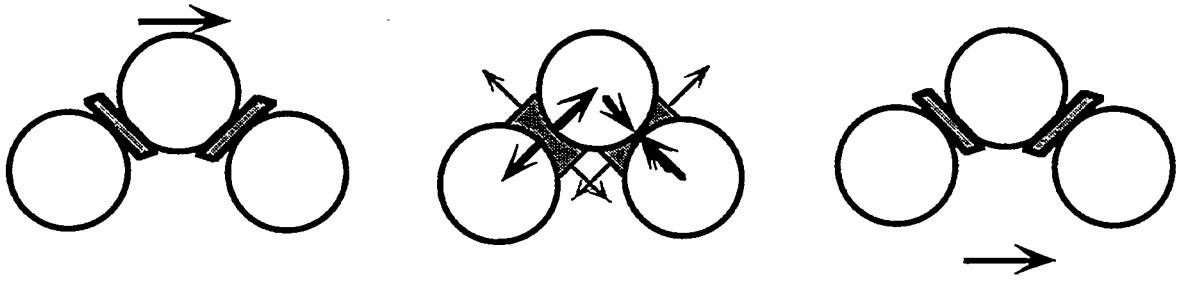

Figure 4.17: Proposed S-wave attenuation loss mechanism for contacts at an angle to the propagation direction. The circles represent the glass beads, the hatched areas the clay-coating, the bold arrows the propagating stresses or displacements, and the small arrows the clay motion. The shear motion can be decomposed into two orthogonal compressional motions, generating pumping losses at off-angle contacts.

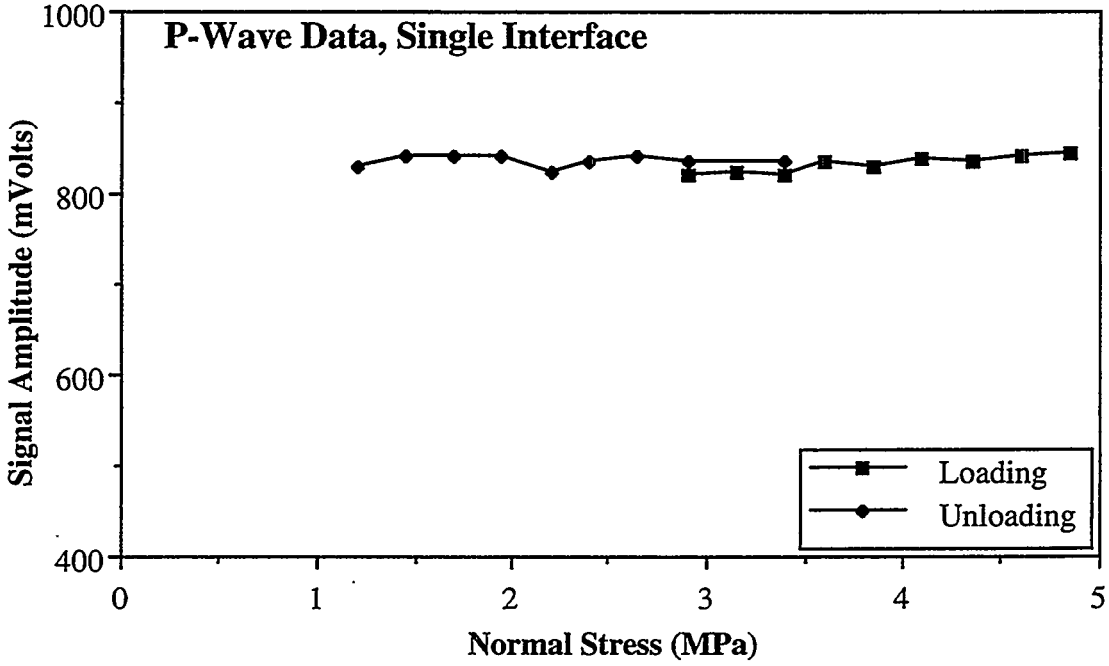

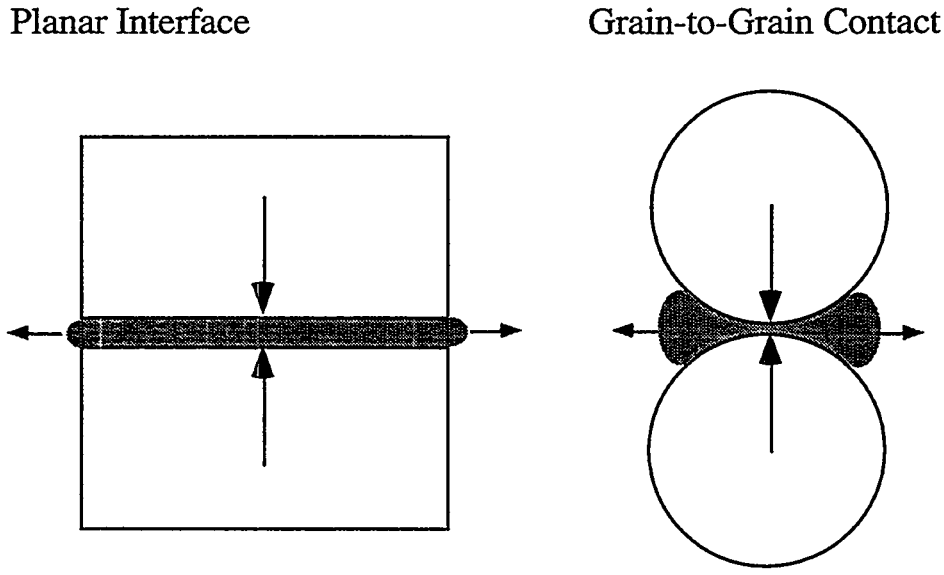

Figure 4.18: (a) Peak-to-peak amplitude data from experiments on a single, planar clay-coated interface, with a clay water content of approximately 160 percent. The data indicate that attenuation is independent of stress at these planar contacts. (b) Differences in clay motion during compressional propagation for planar and point-to-point contact geometries.

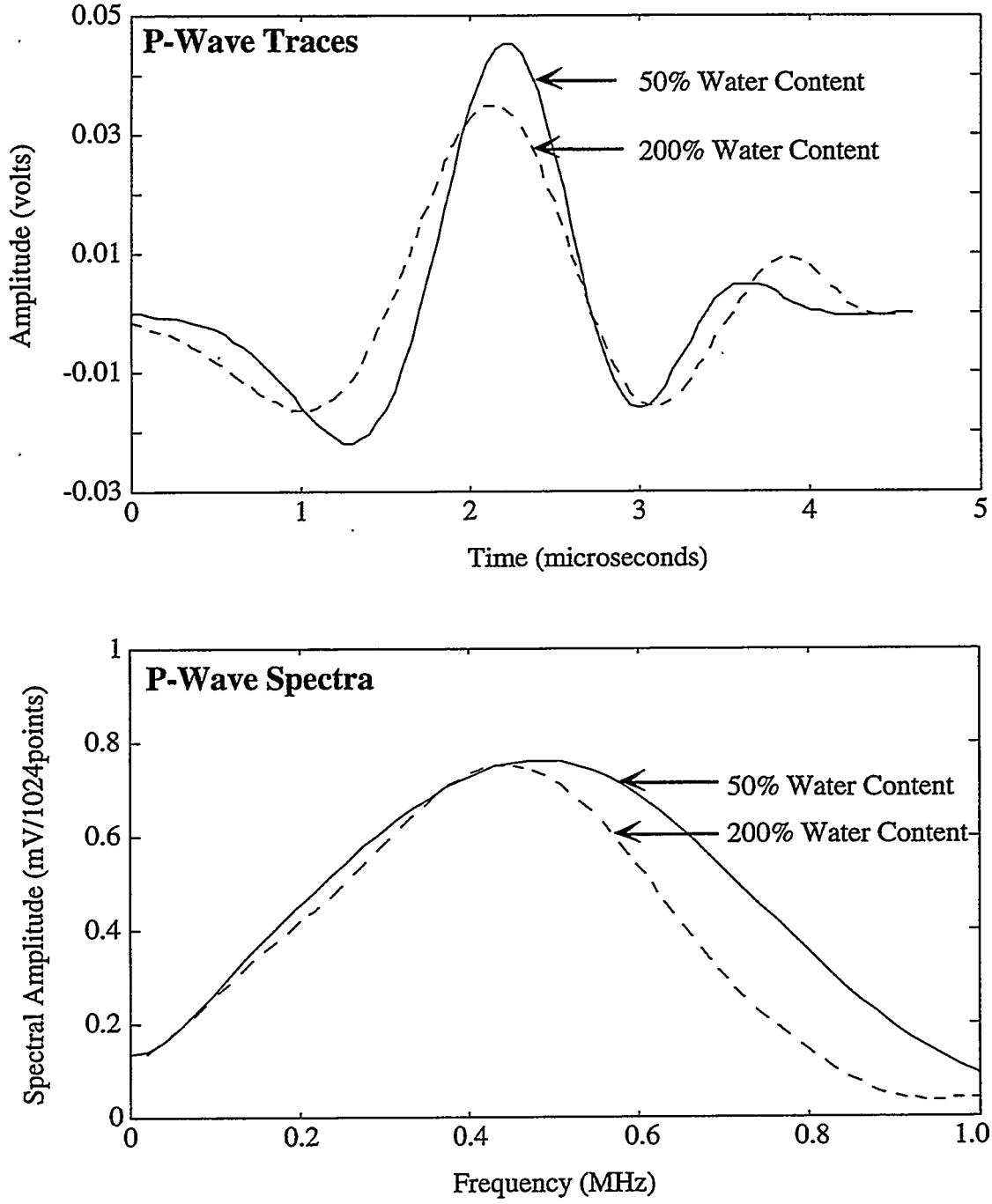

Figure 4.19: P-wave (a) windowed traces and (b) spectra for clay-coated beads at 50 and 200 percent clay water content. The data show distinct energy differences at higher frequencies, although the spectral amplitudes and associated quality factors are similar.

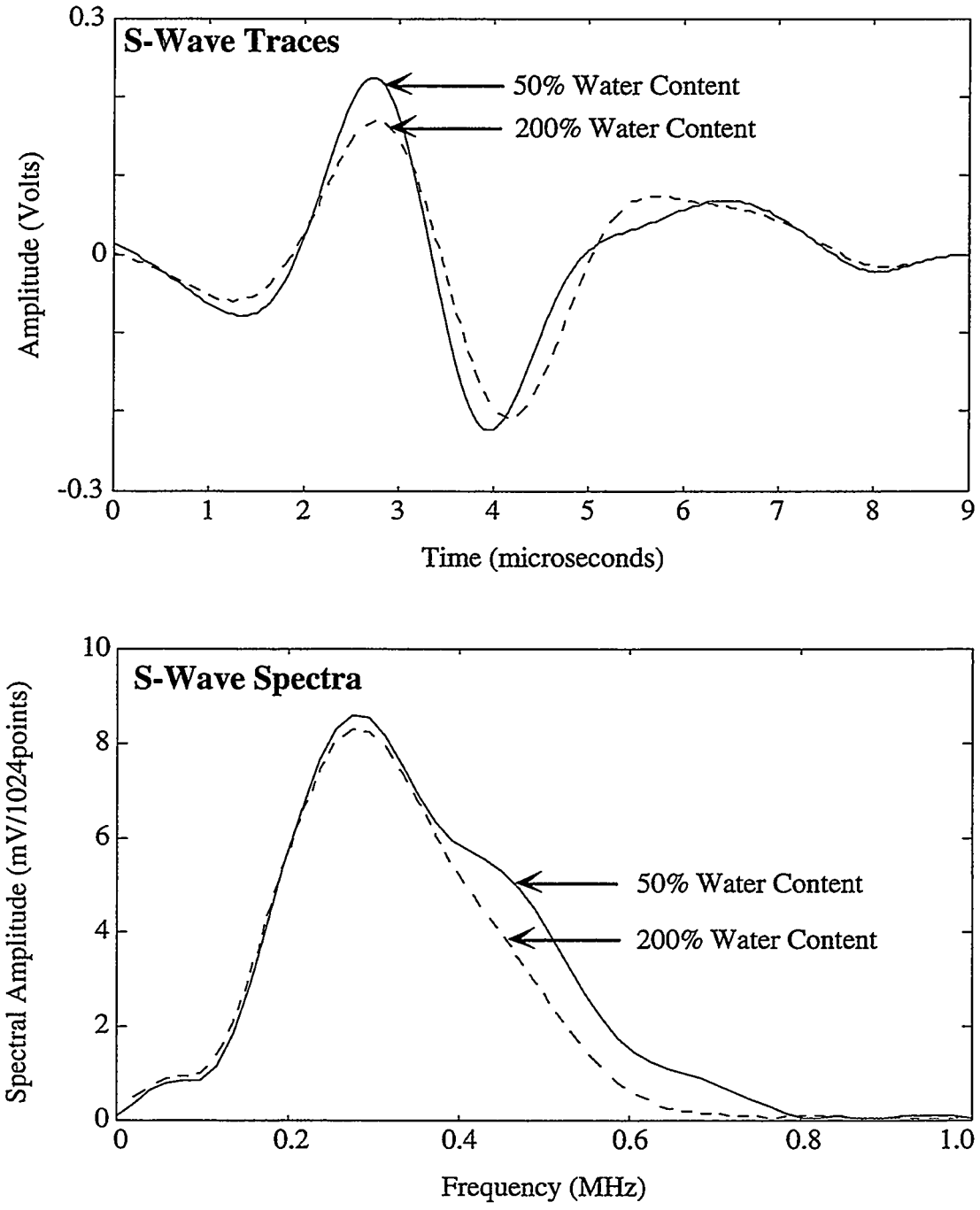

Figure 4.20: S-wave (a) windowed traces and (b) spectra for clay-coated beads at 50 and 200 percent clay water content. The data show distinct energy differences at higher frequencies, although the spectral amplitudes and associated quality factors are similar.

4.6 Effect of Organic Fluids

The effect of fluid type on the seismic properties of clay layers is investigated with specimens using two different organic fluids: hexadecane and ethyl alcohol. The properties of these fluids are given in Table 3.3. Hexadecane is a non-polar molecule that should not chemically interact with the negatively charged clay platelet surfaces. It is not expected to swell clay. When absorbed, it is believed to occupy micropore regions between platelet groups but is not bound to the clay surface. Absorbed hexadecane was thus expected to have a different behavior than absorbed water. Ethyl alcohol is a polar molecule that was expected to swell the clay. Thus, it was expected to behave similarly to water.

The clay fluid content of the specimens with hexadecane and ethyl alcohol was controlled by the maximum absorption in the sealed evaporation vessel. The clay-coated beads absorbed hexadecane to a 50 percent clay fluid content and ethyl alcohol to a 200 percent clay fluid content. These values are much lower than the values of water, and indicate different clay fluid interactions. The differences for hexadecane are attributable to a non-polar nature and larger molecular size. For ethyl alcohol, the differences may be attributable to a weaker polar strength and larger molecular size.

Figure 4.21 presents the group velocities of the 50 percent clay hexadecane content and 200 percent clay ethyl alcohol content specimens. Velocities for corresponding water content data are plotted for comparison. In general, both wave group velocities are similar between the specimens. P-wave hexadecane group velocities are slightly but systematically lower than the three other group velocities. This may be due to the presence of unbound fluid. The unbound molecules may decouple the clay platelet groups during compressional

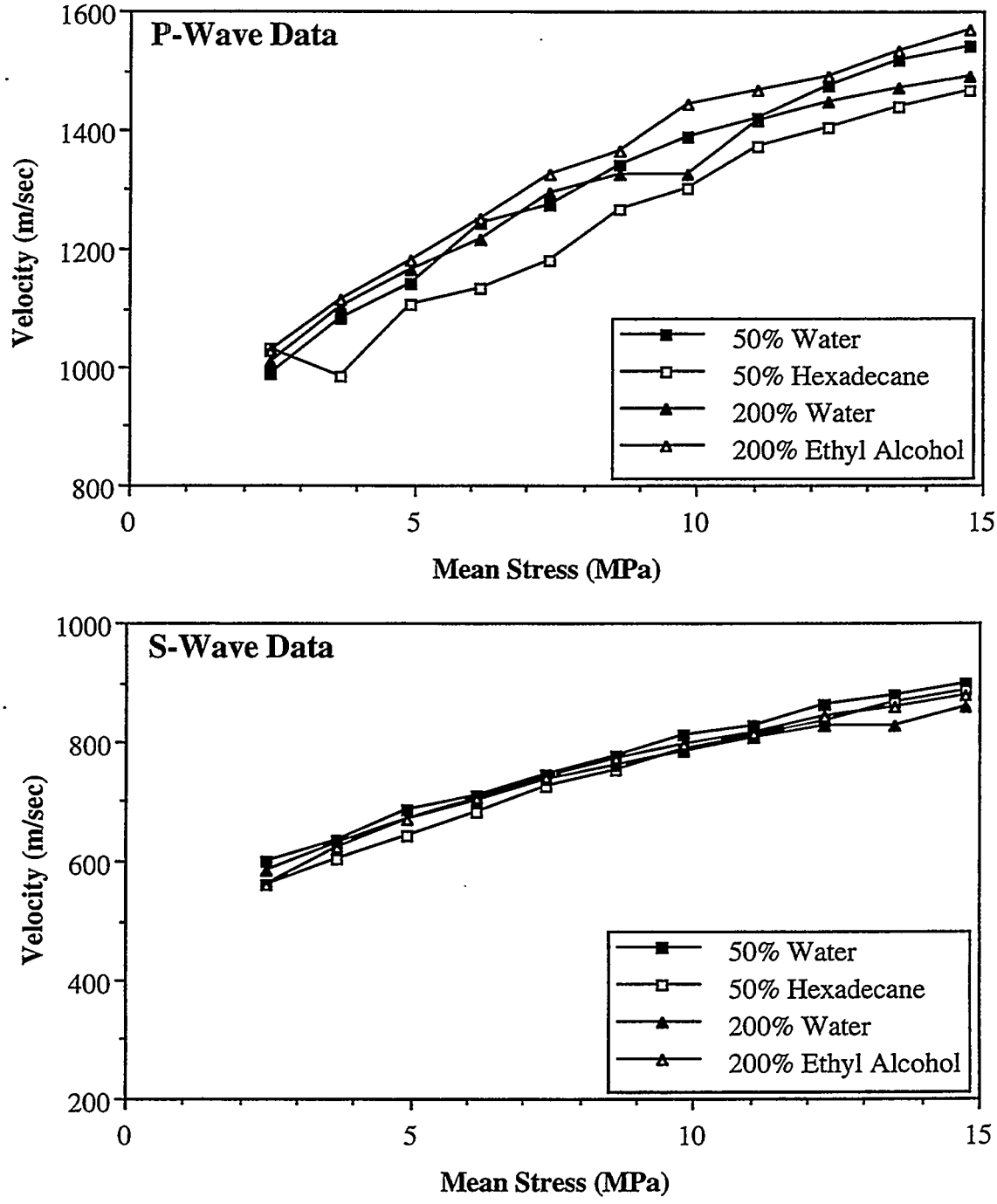

Figure 4.21: (a) P-wave and (b) S-wave velocity data for clay-coated bead specimens with varying organic fluids. The equivalent water content data are plotted for comparison. The velocities are similar, with more scatter in the P-wave than the S-wave data. The P-wave hexadecane velocities are statistically lower than the other velocities, possibly due to the presence of unbound fluid. Note that the velocity scales are the same, but the ranges differ.

motion, leading to decreased group velocity. Shear motion may be carried through the clay matrix, without affecting the micropore fluids.

The 50 percent clay hexadecane and 200 percent clay ethyl alcohol content quality factors are plotted in Figure 4.22. Again, the corresponding water content data are plotted for comparison. In general, the 50 percent clay water specimen quality factors are larger than the 50 percent clay hexadecane specimen quality factors. The three points where hexadecane quality factors are larger than water content factors occur where the data points deviate from the linear trends. At all stress levels, the 200 percent clay water specimen quality factors are significantly larger than the 200 percent ethyl alcohol. In fact, the 200 percent clay ethyl alcohol quality factors consistently have the lowest values. The P-wave peak frequencies follow these same trends; the S-wave peak frequencies show little variation between the four specimens.

Two different factors may cause the 50 percent clay hexadecane quality factors to be lower than 50 percent clay water data. First, the non-polar hexadecane molecules are not bound to the clay. During seismic propagation, there will be movement between the clay matrix and the unbound fluid molecules. This will cause dissipation that lowers the seismic transmission. Second, the clay may be distributed in a manner similar to the clay at higher water contents. This is suggested by the agreement between the P-wave 50 percent clay hexadecane and the 200 percent clay water quality factor data. This agreement may indicate that the clay distribution is similar, e.g. that it is in a toroidal distribution about the grain-to-grain contact. While hexadecane does not cause clay swelling, it can lubricate the platelet aggregates allowing them to move under stress. Therefore, the clay can rearrange to the toroidal distribution, causing similar pumping losses under compression. The lower S-wave quality factors for the 50 percent clay hexadecane specimen as opposed to the 200 percent clay water specimen, would be caused by the presence of unbound fluid molecules.

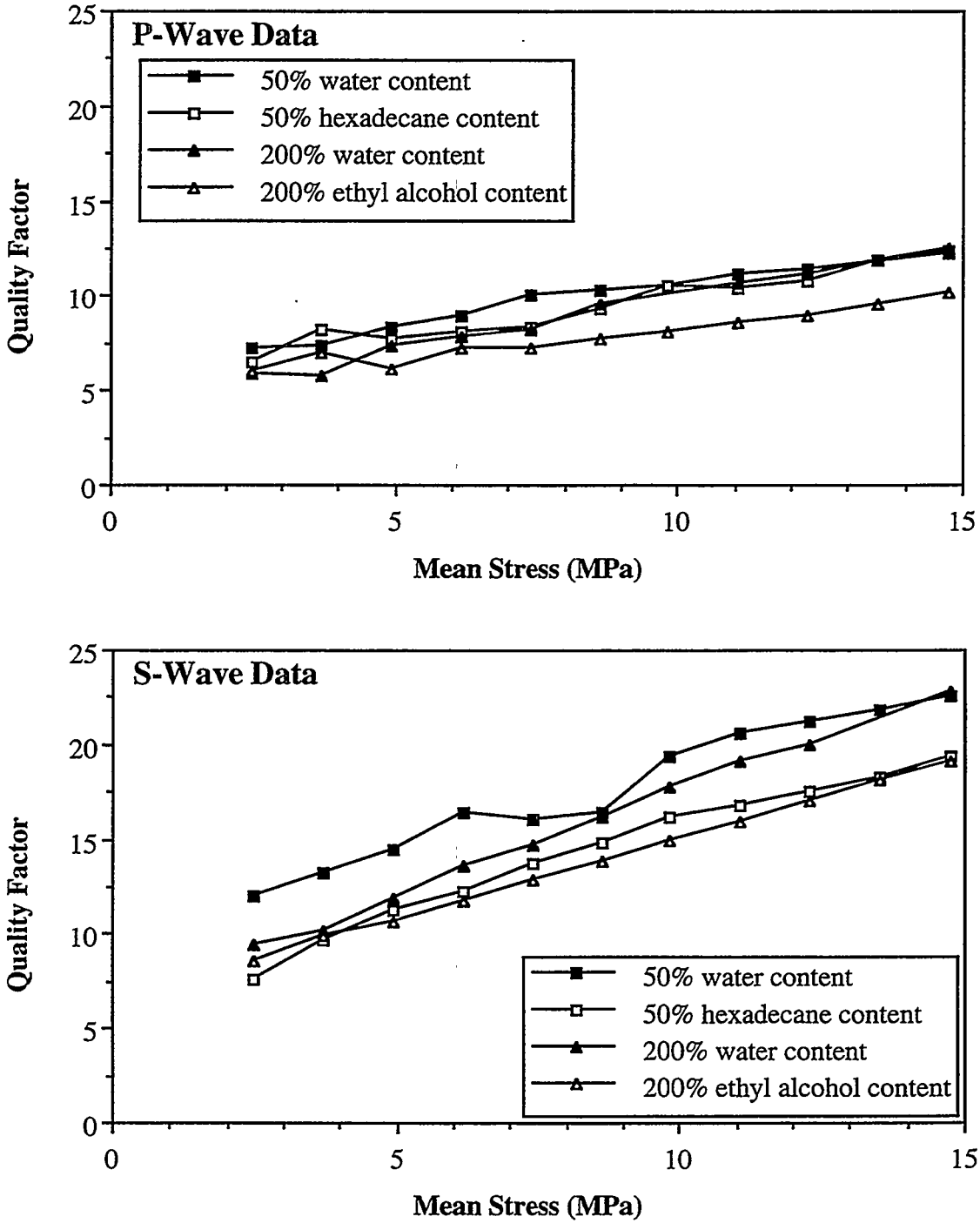

Figure 4.22: (a) P-wave and (b) S-wave quality factor data at individual spectral peak frequencies for clay-coated bead specimens with organic fluids. Equivalent water content data are plotted for comparison. At the lower P-wave stresses and all the S-wave stress levels, the absorbed organic fluid specimens have lower quality factors than the absorbed water specimens. The differences can be attributed to different clay-fluid interations.

The differences between the 200 percent clay ethyl alcohol content and 200 percent clay water content quality factors can be attributed to different clay distributions. During the assembly procedure, it was observed that the clay-ethyl alcohol mixture was more cohesive than the clay-water mixture. This suggests that the clay-ethyl alcohol mixture remained at the grain-to-grain contacts during initial stress cycling. This larger thickness of clay would increase the attenuation, or decrease the quality factors. In fact, the 200 percent clay ethyl alcohol quality factors are more similar to 140 percent clay water quality factors than to 200 percent clay water quality factors. The difference in the clay cohesion is attributed to different chemical interactions between clay and ethyl alcohol and clay and water. This was demonstrated by the differing maximum absorption amounts, and the same factors are involved: dipolar strength and molecular size.

4.7 Summary

In all the specimens, seismic propagation parameters increase with increasing stress. This occurs because the contact stiffnesses of the grain-to-grain contacts in the specimen increase with stress although the porosity remains essentially unchanged. Higher contact stiffnesses may be caused by increases in the number of contacts and/or the size of the contact areas.

Investigations with dry and partially saturated specimens have confirmed that the presence of clay affects the seismic behavior of granular materials. Comparison with seismic propagation in clean beads indicates that clay adds mechanical stiffness and viscosity to the granular contacts.

Both P and S-wave transmissions exhibit the same trends as water content changes. Initially as water is adsorbed into the clay, clay swelling decouples the interfaces and

decreases seismic transmission. At high water contents, the swelled clay begins to lose structural coherence. The local stresses can then force the clay from the grain-to-grain contacts and into the surrounding pore space. Seismic transmission increase in response to the smaller distance between grains and increased contact area.

The agreement in seismic behavior for compressional and shear propagation experiments suggests that the loss mechanisms are similar. Compressional losses are probably due to a pumping mechanism. The clay is pushed into then retreats from the pore space surrounding the point-to-point contact during compressional propagation. Shear losses are probably due to both viscous damping caused by the viscous shear of the clay layer for all contacts and a pumping mechanism for the clay contacts at angles to the propagation direction. The viscous damping acts at contacts in the propagation direction. Pumping occurs as a result of local compression at contacts off-angle to the propagation direction.

The fluid type in the specimen affects the transmission of seismic waves. The absorption of hexadecane, a non-polar fluid, into the clay significantly decreases both P and S-wave transmission compared to a similar amount of water absorption. This is attributed to its non-polar nature. Because it does not interact with the charged clay, it is probably present as an unbound fluid near the grain-to-grain contacts. Movement between the clay matrix and unbound fluid molecules increases dissipation and thus attenuation during seismic propagation. Also, the unbound fluid may lubricate the platelets so that clay distribution is similar to samples with higher water contents. The absorption of ethyl alcohol, a polar fluid, into the clay also decreases seismic transmission compared to a similar amount of water absorption. The difference is probably due to the different adhesive properties of the ethyl alcohol. The ethyl alcohol appears to cause less swelling, resulting in a larger clay coating at the grain contacts compared to the water specimen.

4.8 Conclusions

These experiments have identified the key properties of seismic wave propagation in unconsolidated or poorly consolidated granular materials with clay. First, the grain-to-grain contacts have a major effect on seismic wave propagation in unconsolidated and poorly consolidates materials, probably larger than the effect of porosity. Contact models show that contact stiffnesses increase with stress. Also, the addition of a very small amount of clay at the contacts significantly changes seismic wave propagation. Clay adds both a stiffness and a viscosity to the mechanical properties of the contact due to its structure. The clay rheology is affected by polar fluids sufficient to be detectable seismically. Polar fluids interact with the clay particles and cause swelling. This swelling affects the mechanical properties of the contact. The fluid type is also important, as illustrated by the differences in water and ethyl alcohol specimens. Despite their similar polarities, the chemical interactions were sufficiently distinct to create mechanical property variations that had measurable effects on seismic transmission. In all cases, the differences in attenuations were relatively greater than the differences in velocities.

5.0 Numerical Modeling

5.1 Introduction

Modeling was conducted to aid the interpretation the laboratory results and explore the possible extension of this research to preliminary field characterization. This modeling included analytical low-pass filtering and a numerical boundary element method. The key property required in the numerical code is the ability to input and vary rheologic properties at the grain-to-grain contacts. A boundary element method was found to be particularly versatile in incorporating rheologic interfaces at the grain-to-grain contacts. This chapter discusses the low-pass filtering, numerical technique, model configurations, and numerical simulations conducted to assess the effect of clay at granular contacts on seismic wave propagation.

5.2 Low Pass Filter

In spectral analysis of the laboratory seismic traces, the peak frequencies of the transmitted waves are found to be much lower than the input peak frequencies. This is investigated numerically by applying a low pass, Butterworth filter to aluminum standard traces from the calibration tests.

Two Butterworth filters are used, one of order four and one of order eight. Two different cutoff frequencies are investigated for each wave type: 400 and 800 kHz for the P-wave trace and 250 and 500 kHz for the S-wave trace. The shape of the filters in the frequency domain is shown in Figure 5.1. The lower order filter has a gentler fall-off than the higher order filter.

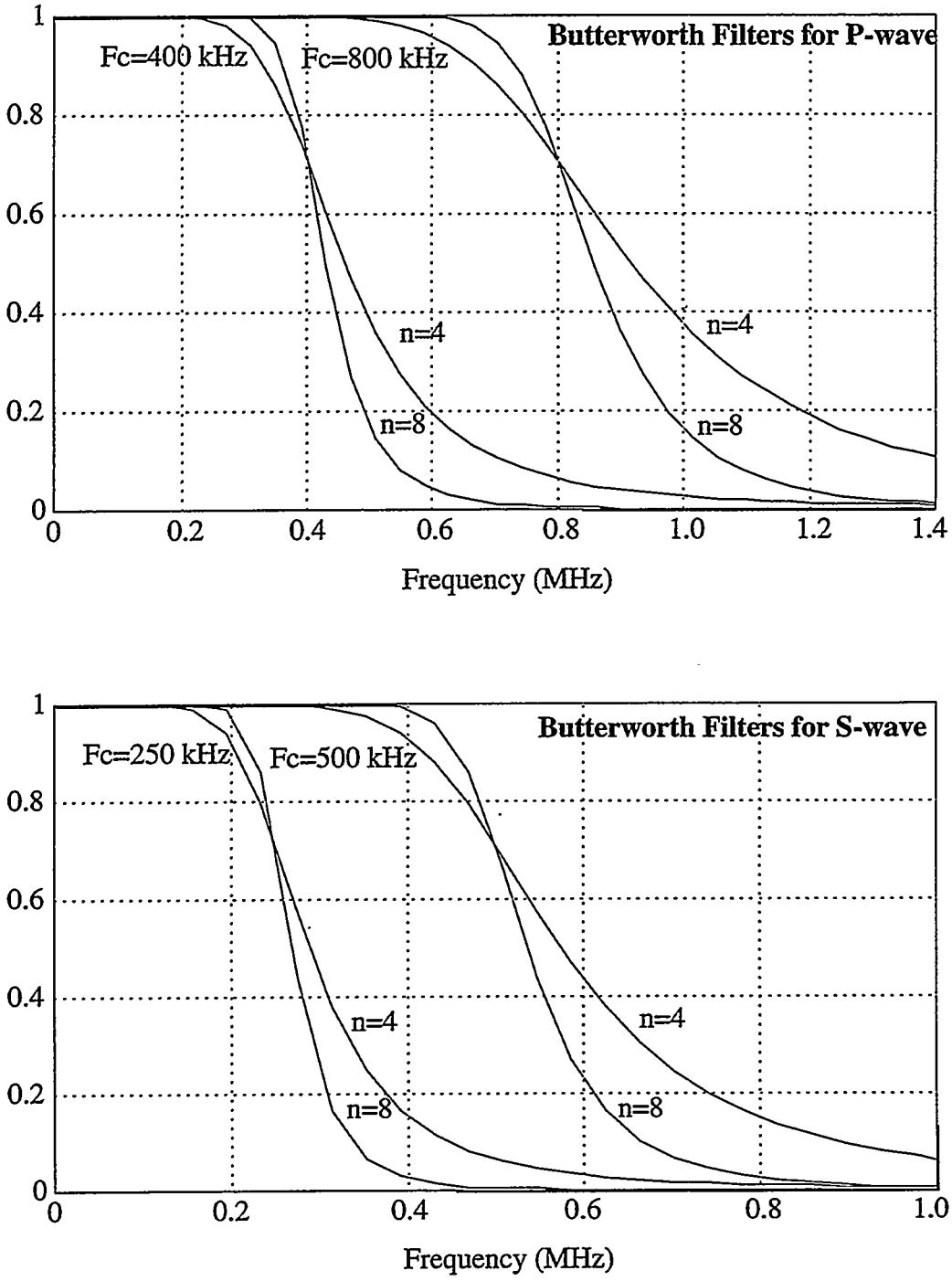

Figure 5.1: Butterworth, low-pass filters are shown in the frequency domain for (a) P-waves and (b) S-waves. Four filters were needed to encompass two different frequencies and two different orders. Cutoff frequencies correspond to the input peak frequency and half the input peak frequency.

The original and filtered spectra are shown in Figure 5.2. As expected, energy above the cutoff frequency is removed from the filtered spectra. The result is much lower peak spectral amplitudes at the lower cutoff frequencies. The lower cutoff-frequency peak spectral amplitude values are within an order of magnitude of values measured in the glass bead specimens. In addition, the peak frequencies at the lower cutoff frequencies are within the same range as the peak frequencies in the glass bead specimens.

The P-wave and S-wave original and filtered waveforms are presented in Figures 5.3 and 5.4 to assess the effects of discontinuous boundary conditions in the time domain. Removal of the high frequency energy has three effects. First, the filtered waves arrive at slightly delayed times. The higher order filters (n=8) have longer delays than the lower order filters (n=4) at similar cutoff-frequencies. Second, significant decreases are seen in the trace amplitudes in accordance with the removal of high frequency energy. The higher order filters appear to cause larger decreases than the lower order filters at similar cutoff frequencies. Lastly, the filtered waveforms are dispersive as indicated by the shift in energy from the first cycle to later cycles in the traces. This is best seen in the higher cutoff-frequency filtered waveforms, where additional peaks appear after filtering. In the laboratory measurements, the clean, dry glass bead specimen tests exhibited this same energy shift (see Figure 4.3). The lack of additional peaks in clay-coated glass bead specimens may be due to viscous losses.

The shapes and peak frequencies of the numerically-filtered waves agree with the laboratory data. These agreements attest that a Butterworth filter can describe the frequency changes seen in the laboratory data. The Butterworth filter is mathematically similar to the displacement and velocity discontinuity boundary condition, as shown by the agreement in the shape of the filters (Figure 5.1) and the displacement discontinuity transmission

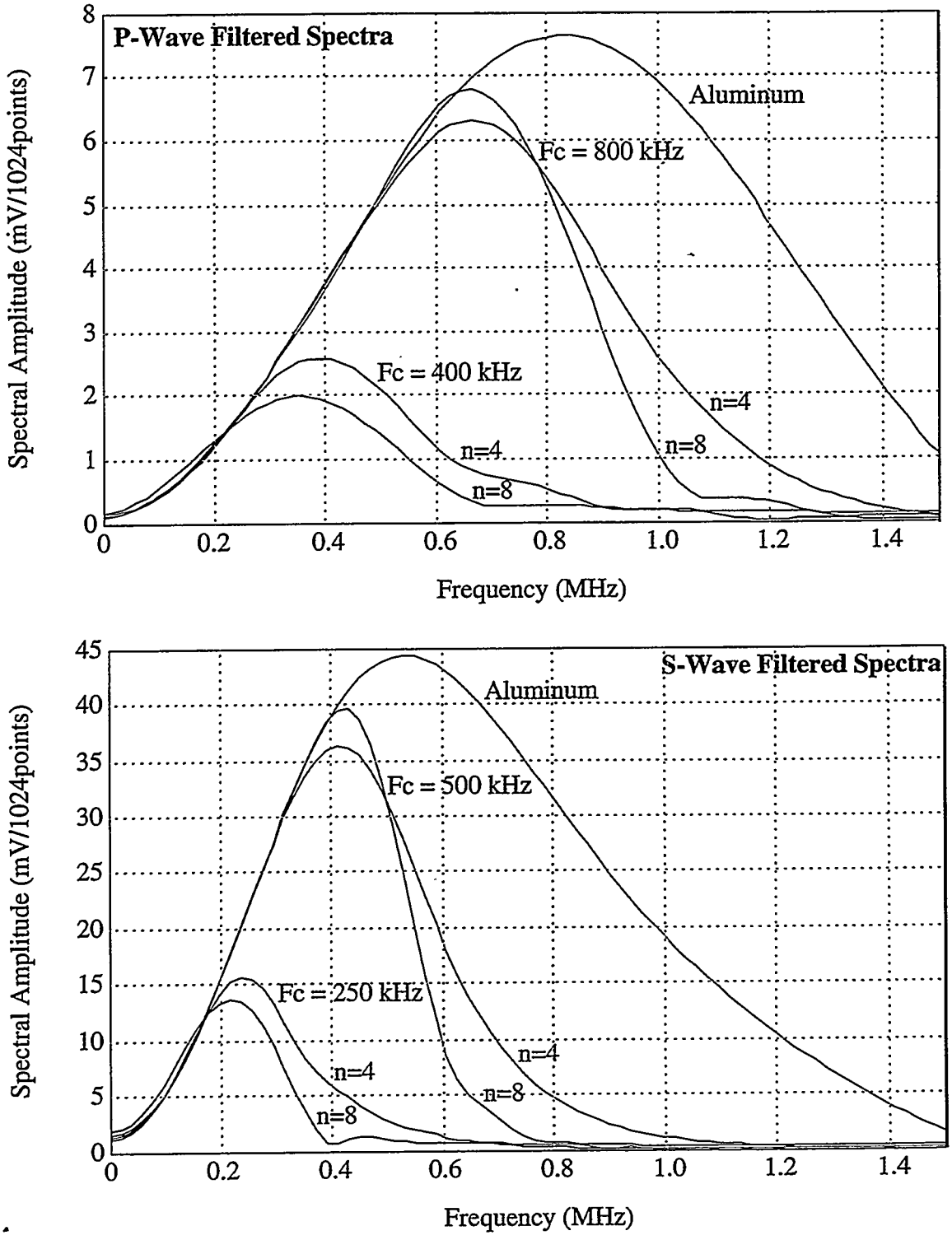

Figure 5.2: Wave spectra before and after applying the filters shown in Figure 5.1 for (a) P-waves and (b) S-waves. Filtering removes the energy above the cutoff frequency, thereby lowering the peak frequencies and peak spectral amplitudes.

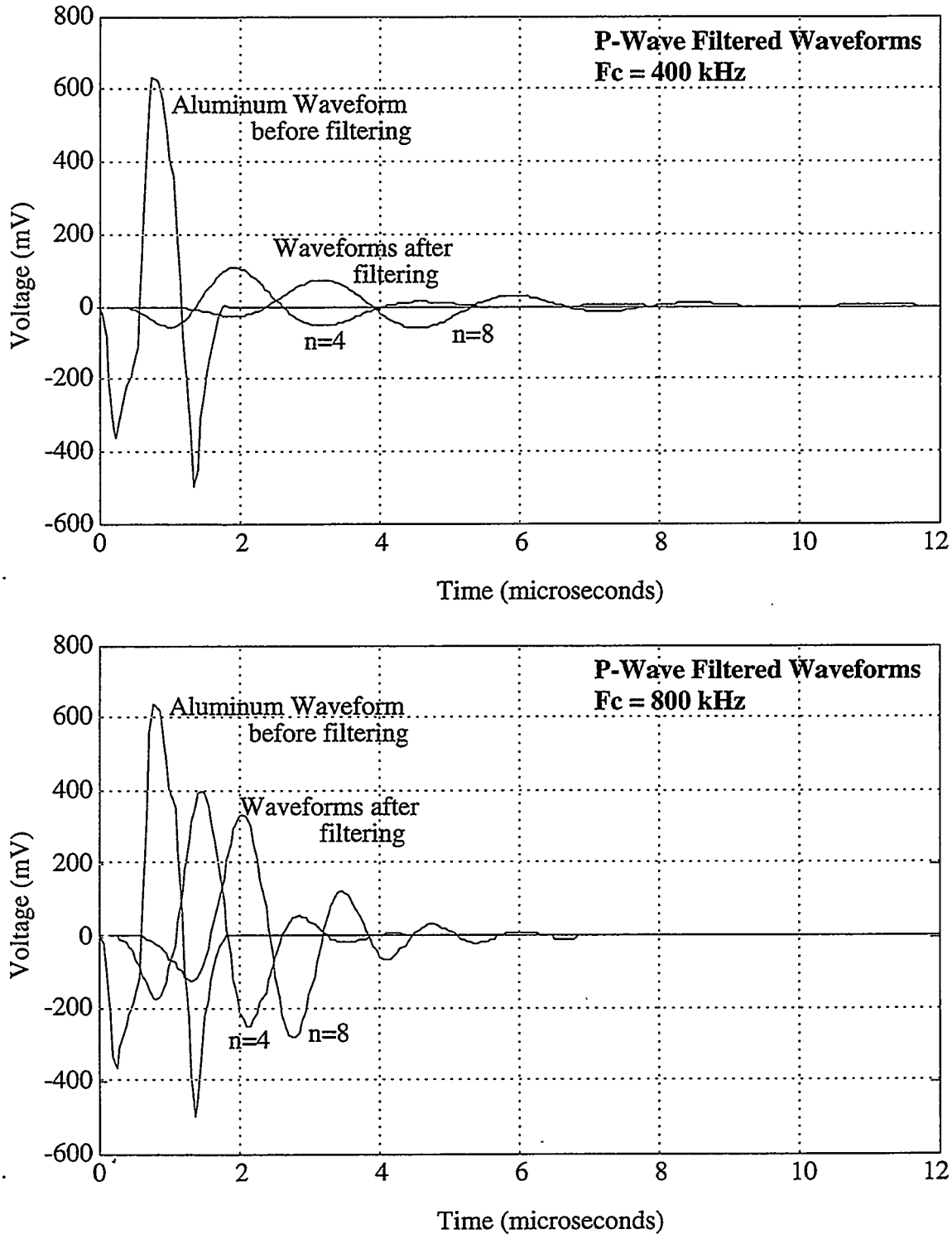

Figure 5.3: Aluminum P-wave traces before and after applying the filters shown in Figure 5.1a for cutoff frequencies of (a) 400 and (b) 800 kHz. Filtering delays the wave arrivals, decreases the displacements, and introduces additional displacement lobes.

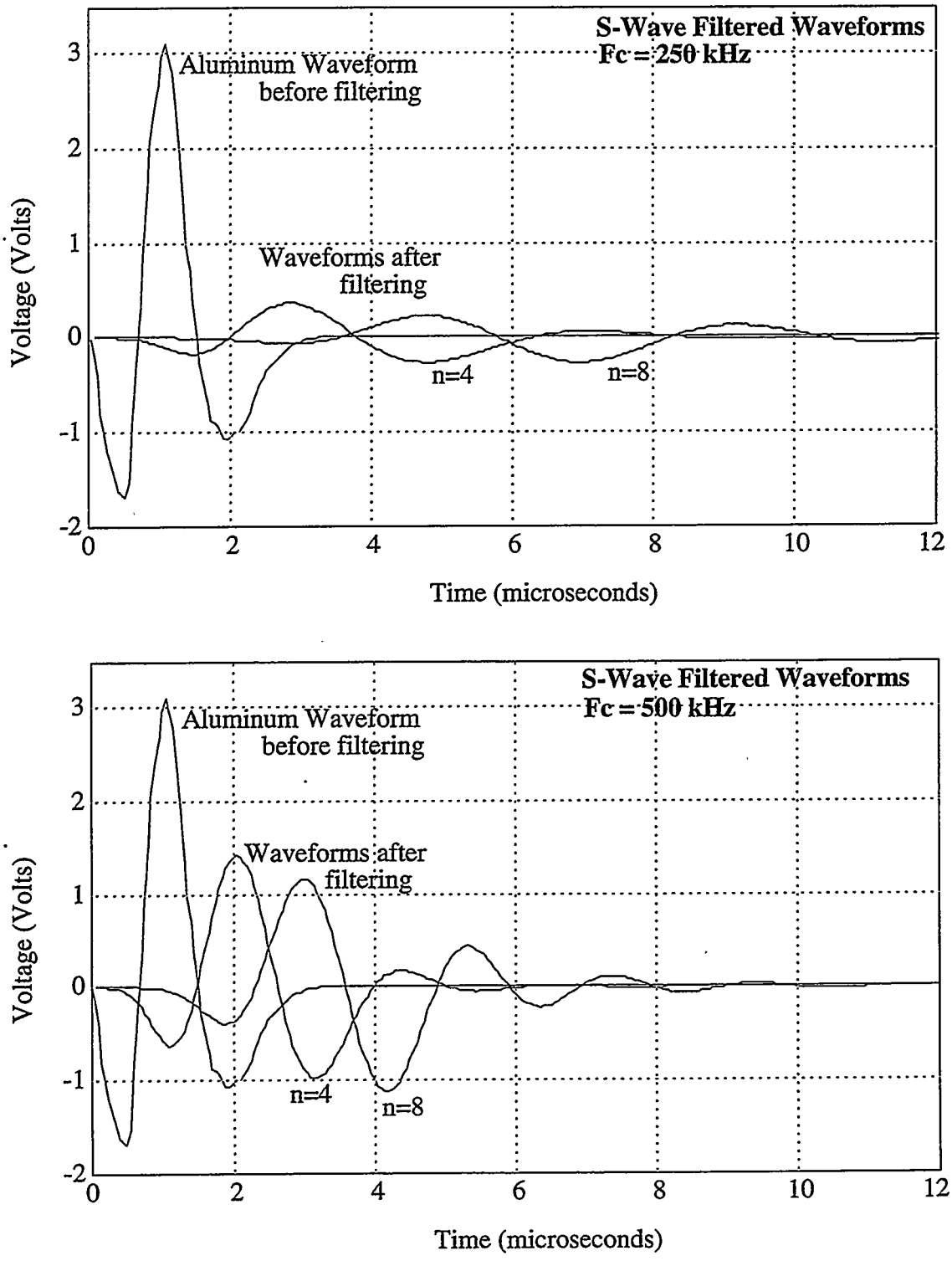

Figure 5.4: Aluminum S-wave traces before and after applying the filters shown in Figure 5.1b for cutoff frequencies of (a) 250 and (b) 500 kHz. Filtering delays the wave arrivals, decreases the displacements, and introduces additional displacement lobes.

coefficient (equation 2.39 and Figure 5.5). This similarity implies that effects at multiple interfaces can be accurately represented by the discontinuous displacement and discontinuous velocity boundary condition.

5.3 Boundary Element Method

Numerical models of granular materials simulate one of two situations. Inclusion models consider the solid matrix to be continuous and input pore space as geometrical inclusions. Grain packing models consider the matrix to be composed of individual grains and allow the contact processes to vary. Although inclusion models are more standard in acoustic analysis, grain packing models are more appropriate for investigating contact mechanics since they more accurately capture the interface mechanics and geometry.

A two-dimensional grain packing model using the boundary element method has been recently developed (Nihei, 1992). This model provides a fully dynamic solution for two dimensional seismic wave propagation within the modeled system. As such, it captures both the scattering and viscous losses that occur during seismic propagation through granular material.

The boundary element method will be summarized here. A full description of the method can be found in Nihei (1992). Elastic wave propagation is described by the elasto-dynamic integral equation (equation 2.5). For a monochromatic wave at frequency ω, the indicial form of the equation is (Aki and Richards, 1980):

$$u_i(r,\omega) = \int_\Gamma \left[G_{ij}(r,r^*,\omega)\sigma_j(r^*,\omega) - \Sigma_{ij}(r,r^*,\omega)u_j(r^*,\omega) \right] d\Gamma(r^*) + \int_\Omega G_{ij}(r,r^p,\omega) f_j(r^p,\omega) d\Omega \qquad (5.1)$$

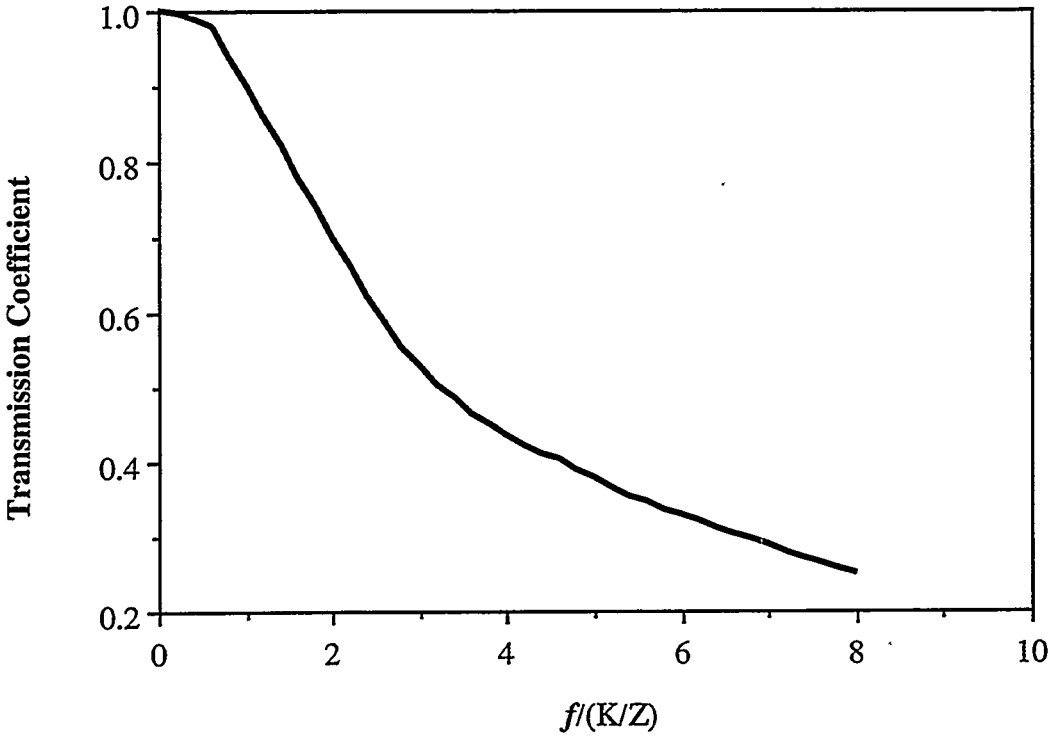

Figure 5.5: Transmission coefficient as a function of normalized frequency at a discontinuous displacement boundary condition for a plane wave normal to a single interface. Normalized frequency is defined as the frequency divided by the interface stiffness over the medium impedance. From Pyrak-Nolte *et. al.* (1990).

where Γ is the surface, Ω the volume, u_i the displacement, G_{ij} the Green's function, σ_j the stress traction, Σ_{ij} is Green's stress tensor, f_j the volumetric body force located in the volume, r the location of the receiver, r^* the location of a point on the surface, and r^p the location of the body force (Figure 5.6). For an SH-wave, Green's function and Green's stress tensor are the scalar quantities:

$$\begin{aligned} G_{ij}(r,r^*,\omega) &= G_{33}(r,r^*,\omega) = \frac{i}{4\mu} H_o^{(1)}(k_T R) \\ \Sigma_{ij}(r,r^*,\omega) &= \Sigma_{33}(r,r^*,\omega) = -\frac{ik_T}{4}(\hat{n}_1\gamma_1 + \hat{n}_2\gamma_2) H_1^{(1)}(k_T R) \end{aligned} \tag{5.2}$$

where μ is the shear modulus, $k_T = \omega/c$ the wavenumber, $R = (r - r^*)$ the distance from the source to the receiver, $\hat{n}_i$ the unit normal at r^*, and $\gamma_i = (x_i^* - x_i)/R$ the direction cosines.

The boundary element method solves for the unknown parameters along the boundaries of specified objects, in this case the displacement and stresses. This is accomplished by allowing r to approach the boundary Γ. Singularities arise when r approaches r^*. At these locations, the contributions of the singular integrals in the elastodynamic equation are replaced by their principal values. The resulting form of the elastodynamic equation is:

$$\begin{aligned} c(r)u_i(r,\omega) = &-\int_\Gamma \Sigma_{ij}(r,r^*,\omega)u_j(r^*,\omega)d\Gamma(r^*) \\ &+\int_\Gamma G_{ij}(r,r^*,\omega)\sigma_j(r^*,\omega)d\Gamma(r^*) + u_i^p(r,w) \end{aligned} \tag{5.3}$$

where c, the free term is:

$$c(r) = \left\{\delta(r - r^*) + \lim_{r \to r^*} \int_{\Gamma_\varepsilon} \Sigma_{ij}(r,r^*,\omega)d\Gamma(r^*)\right\} \tag{5.4}$$

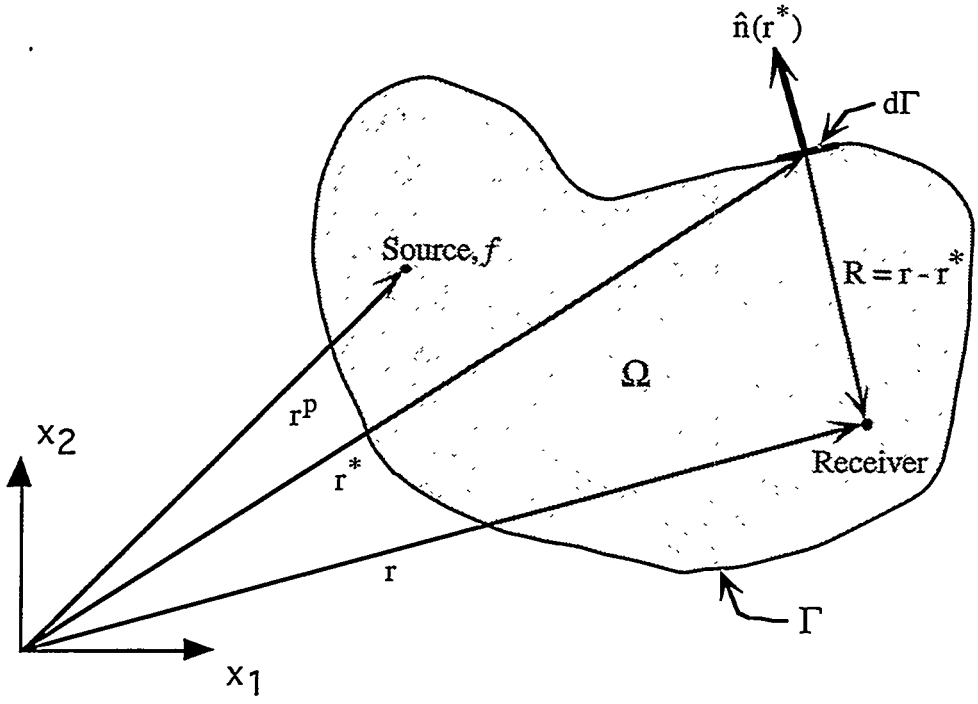

Figure 5.6: Generalized diagram showing the geometry represented in the elastodynamic integral equation where Γ is the surface, Ω the volume, u_i the displacement, f the source, $\hat{n}(r^*)$ the unit normal at the surface, r the location of the receiver, r^* the location of a point on the surface, r^p the location of the source, and R the distance between the surface and receiver.

This equation, called the singular boundary integral equation for displacement u_i, is relevant for two and three dimensional calculations given the appropriate Green's function and Green's stress tensor.

In this two-dimensional formulation, wave excitation is by means of a line source. Displacements and stresses are first calculated in the frequency domain, and then inverted to the time domain using an inverse Fourier Transform. The values within the body are computed from the calculated boundary displacements and stresses by numerically integrating the elasto-dynamic integral equation.

The numerical code is formulated for the special case of SH-waves. Because of the scalar nature of acoustic waves and since this study is not concerned with converted waves, the same solution can also be used for P-waves with an appropriate scaling of the compressional modulus and velocity.

Modeling starts with the discretization of each grain into boundary elements. Neighboring grains are coupled together by a rheologic interface. The interface rheologies can vary from Hooke, Newton, Maxwell, to Kelvin-Voight (Figure 2.3). These simulate the full spectrum of possible interface conditions including dry, fluid-filled, and clay-filled grain contacts. A discontinuous displacement and discontinuous velocity boundary condition is applied at each grain-to-grain contact.

5.4 Numerical Model Evaluation

The boundary element formulation is verified by two tests. The first test is a reciprocal test across a single planar contact. In this test, the source and receiver locations, located on opposite sides of the contact, are inter-changed. The computed traces were

equal, showing that the internal mathematics of the code are consistent. Refraction is simulated in the second verification test. Snell's Law demonstrates that at a contact between two materials, a critical angle exists such that plane-wave energy incident at that angle will travel along the interface instead of traveling into the second media. This is mathematically represented as:

$$\theta_c = \sin^{-1}\left(\frac{c_1}{c_2}\right) \tag{5.5}$$

where θ_c is the critical angle, c_1 the velocity in media 1 and c_2 the velocity in media 2. Simulations showed that the wave did propagate along the contact and did not enter the second medium. This test verified the physical accuracy of the code.

The numerical code was validated by simulating the results of laboratory measurements of shear wave propagation across a single, clay-coated, planar contact between two crystal quartz disks performed by Suárez-Rivera (1992). That study found through analytic equations that both the Kelvin-Voight and Maxwell rheologic models successfully predicted the measured reflected and transmitted spectra for a single, clay-coated planar contact. This data is input into the numerical boundary element code to verify the physics of the model.

The model configuration is shown in Figure 5.7. Modeled distances are equal to the distances in the single planar contact tests performed by Suárez-Rivera. A difference is that the numerical model assumes that the "transducers" are laterally infinite, e.g. plane wave propagation without edge effects. The best-fit specific stiffness and specific viscosity values determined by Suárez-Rivera for both the Kelvin-Voight and Maxwell rheologic models at the single contact for the highest stresses were used. Model results for the dry clay and 27 percent clay water content tests are shown in Figure 5.8 and 5.9. The

Single Contact Numerical Modeling

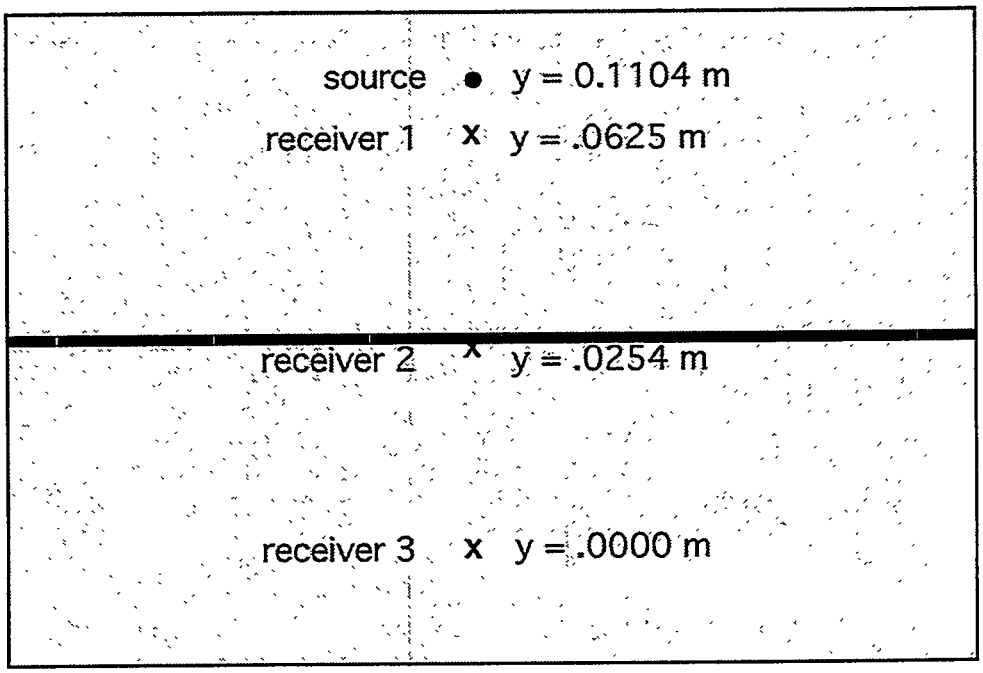

Solid Parameters:

f_c = 525 kHz
c_s = 3222 m/sec
μ = 25.7 GPa
ρ = 2480 m/kg^3

Interface Parameters	Kelvin-Voight Rheology	Maxwell Rheology
K_{dry} (Pa/m)	1.8×10^{13}	6.5×10^{12}
η_{dry} (Pa-s/m)	7.8×10^{5}	1.1×10^{6}
$K_{27\%}$ (Pa/m)	6.5×10^{12}	1.0×10^{13}
$\eta_{27\%}$ (Pa-s/m)	1.1×10^{6}	5.5×10^{6}

Figure 5.7: Model configuration and input parameters for evaluation of the boundary element method. Input parameters equalled values from a single planar contact reported by Suárez-Rivera (1992). The interface is non-welded.

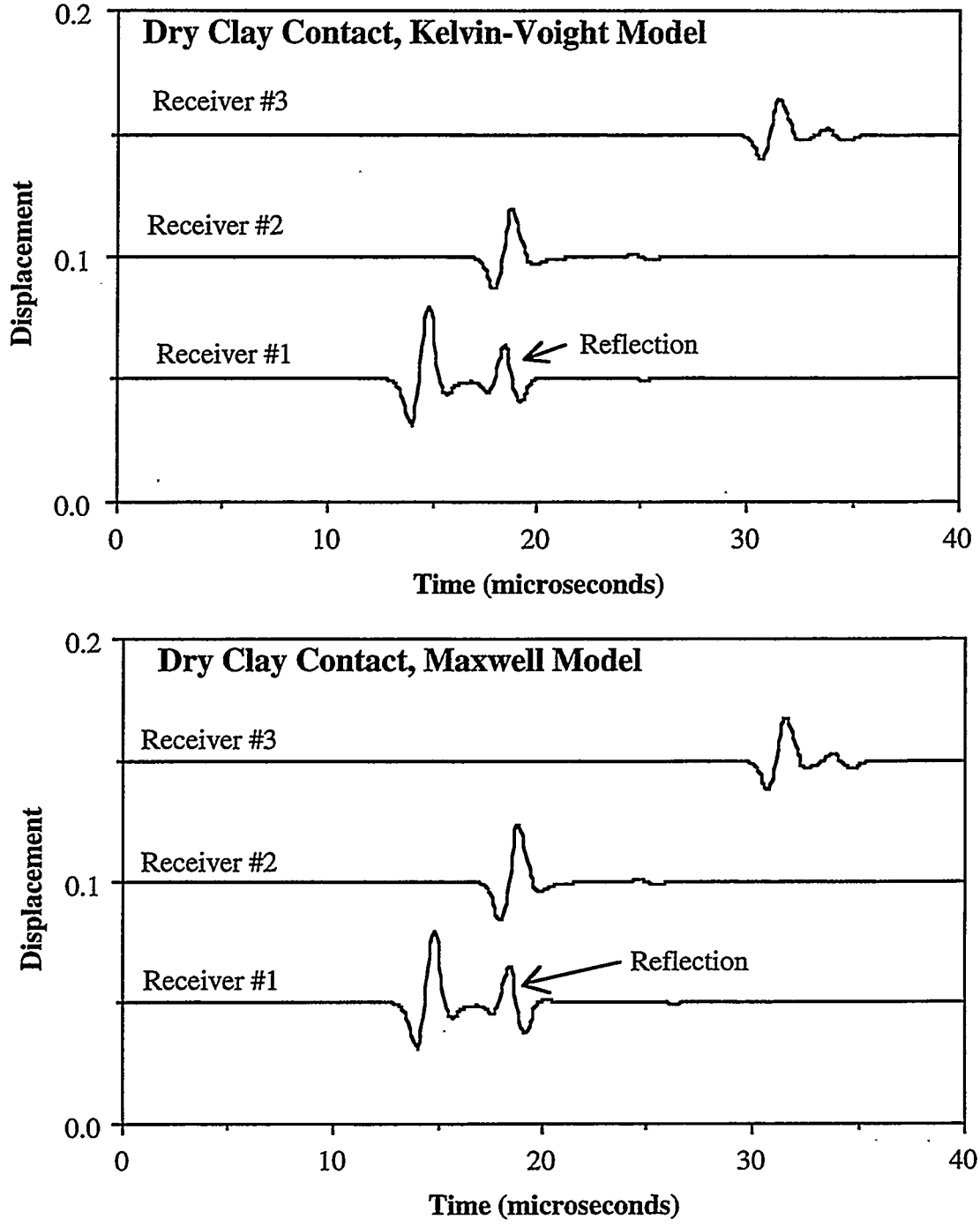

Figure 5.8: Calculated traces for a modeled single interface with dry clay coating. Traces are displayed for the three receiver locations shown in Figure 5.6. Interface properties are equal to the best-fit values for laboratory data reported by Suárez-Rivera (1992). Both Kelvin-Voight and Maxwell rheologic models give similar results.

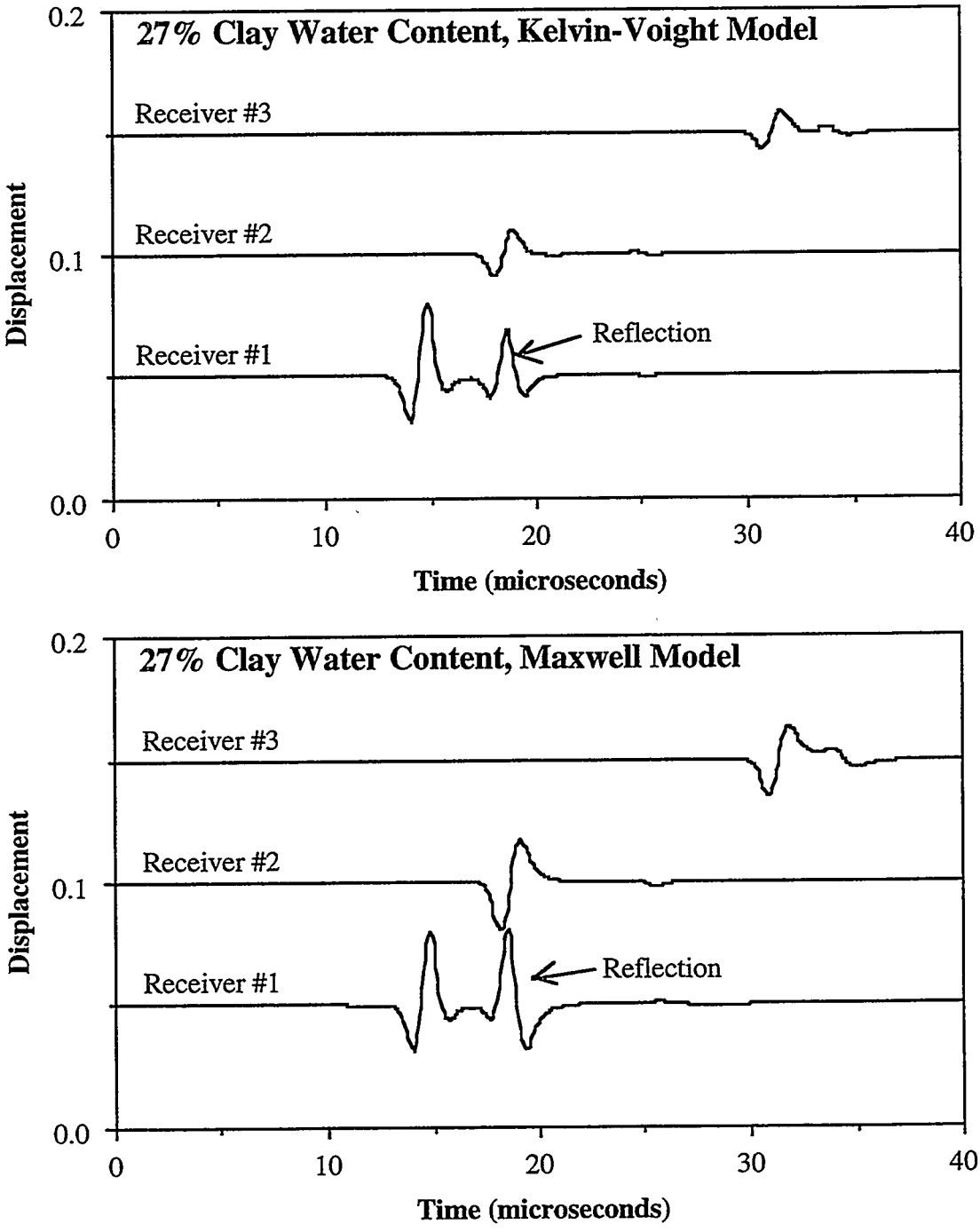

Figure 5.9: Calculated traces for a modeled single interface with clay coating at 27 percent water content clay. Traces are displayed for the three receiver locations shown in Figure 5.6. Interface properties are equal to the best-fit values for laboratory data reported by Suárez-Rivera (1992). Both Kelvin-Voight and Maxwell rheologic models give similar results.

secondary wave arrival at the first receiver is caused by reflection of the wave at the contact. The modeled dry clay traces are similar. The modeled 27 percent clay water content wave traces have small differences in magnitude. The Kelvin-Voight rheology has more reflection and less transmission than the Maxwell rheology. Still, the waveforms are similar and distinctly different than for the dry clay waves. These results suggest that the numerical code does capture the physics of acoustic wave propagation with rheologic contacts. Also, both contact models produce physically realistic transmission charateristics that can be used to analyze propagation in the multiple interfaces.

5.5 Numerical Input

The basic model configuration for both P and S-waves is shown in Figure 5.10. Symmetry in acoustic wave propagation allows the full displacement to be captured by modeling of only one grain column with traction-free sides. Because this work focuses on grain contacts, not grain shape, the spherical grains are approximated as cubically-packed squares to facilitate coupling between the grains. Each grain side is divided into six boundary elements, for a total of 24 boundary elements. The elastic parameters for both the grain column and the upper-half space were set equal to data for isomorphous glass. Accurate numerical results require that the grain column length be larger than one wavelength. Memory constraints set the maximum number of grains to ten. Therefore, the grain diameter is set equal to 400 micrometers to insure that computations are accurate.

The grain column is placed between two half-spaces. The source is located in the top half-space, 400 μm directly above the grain column. A three-lobe Ricker wavelet is used as the source for both P and S-waves. The frequencies for the numerical trials are approximately equal to the laboratory frequencies: 800 kHz for P-wave computations and 525 kHz for S-wave computations. The input waves are shown in Figure 5.11. The

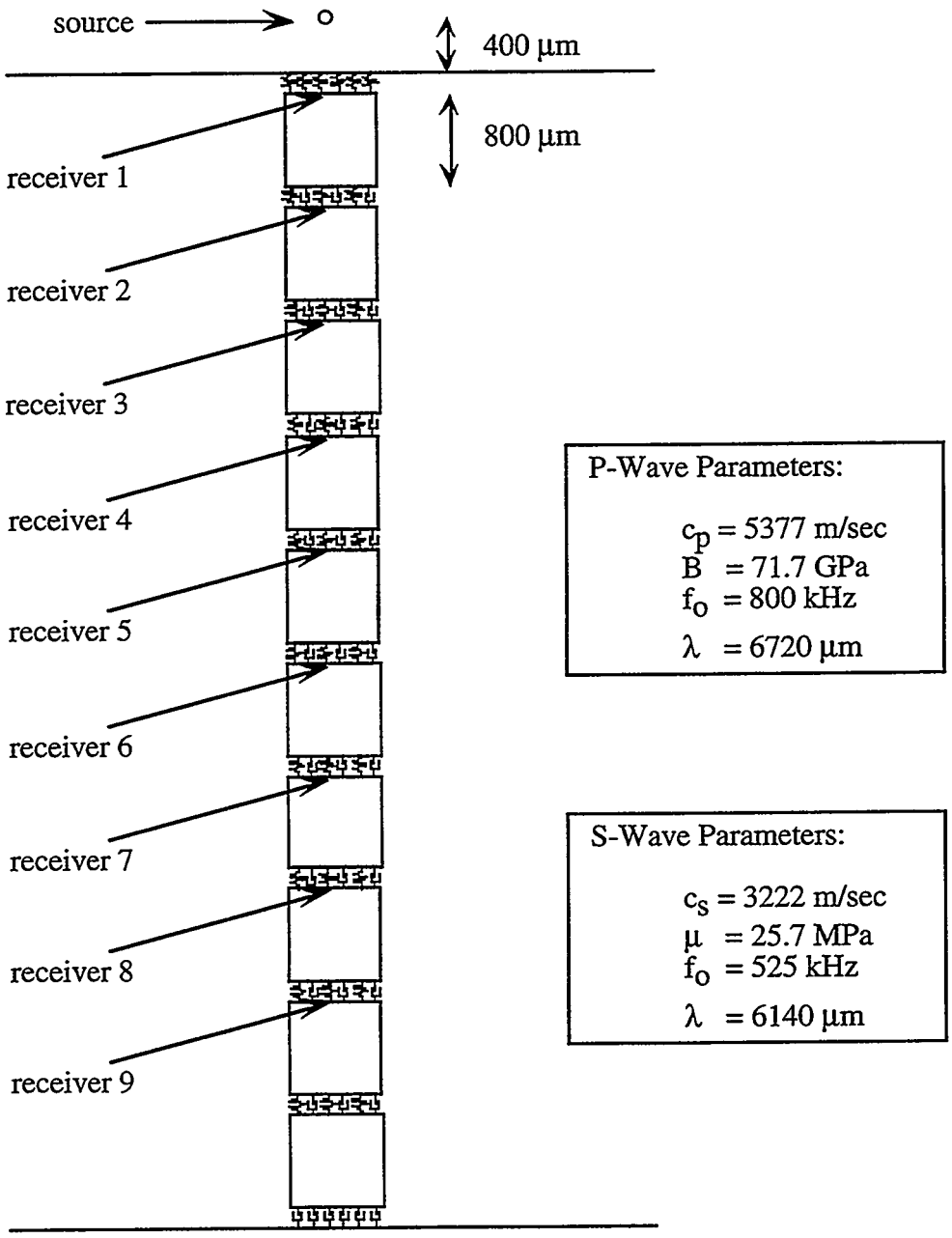

Figure 5.10: Model configuration for the numerical modeling. Specific stiffness and specific viscosity can be varied at the boundaries between the grains. The parameters for the grains and half-spaces are equal to the glass bead specifications.

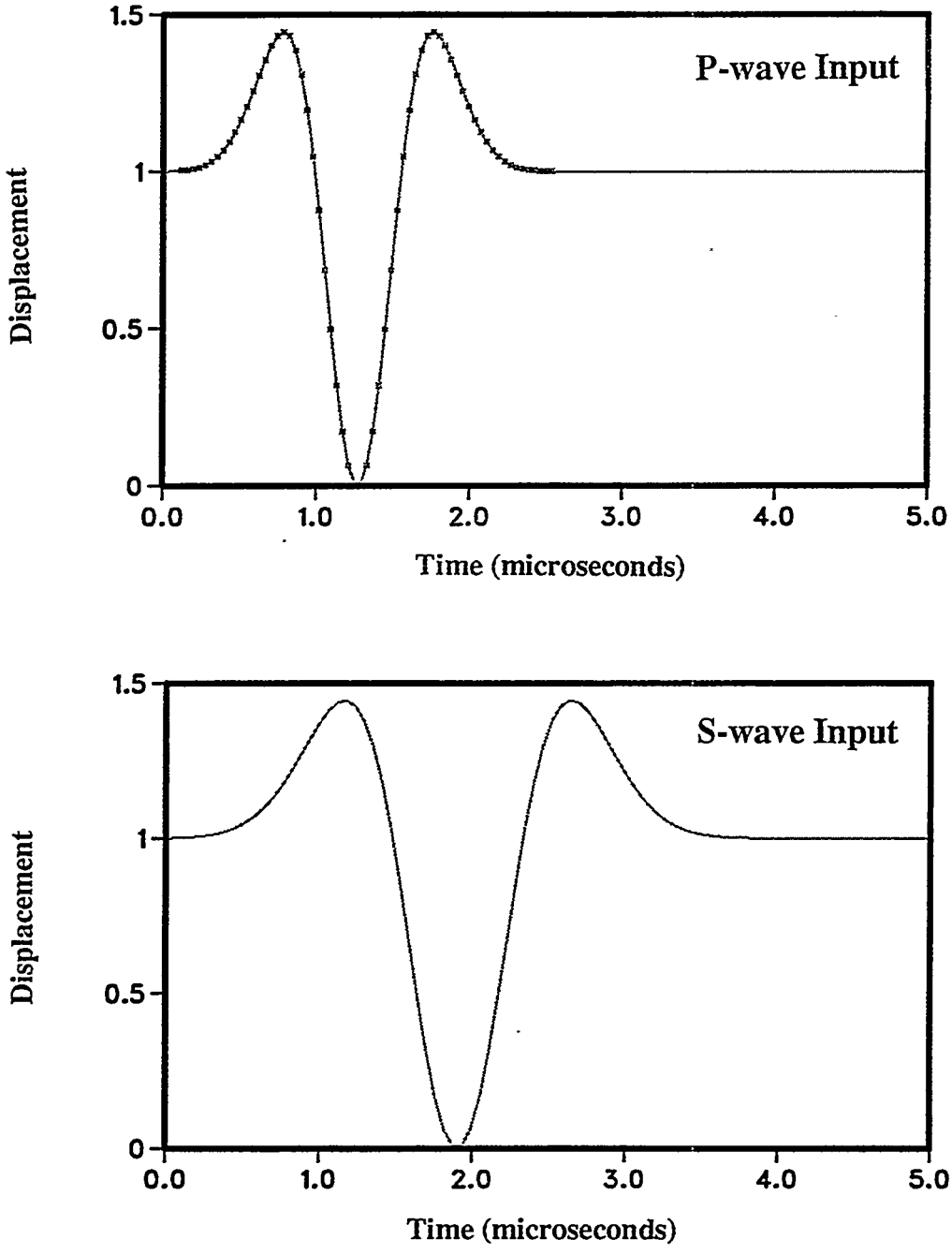

Figure 5.11: Ricker wavelets used as input for (a) P-wave and (b) S-wave numerical simulations.

boundary between the grain column and the upper half-space is welded by setting the specific stiffness equal to $1x10^{22}$ Pa/m and the specific viscosity to 0.0 Pa-s/m. Receivers are placed at the top of grains 1 though 9.

The Kelvin-Voight rheologic model is used in these simulations. A non-reflective interface is incorporated at the boundary between the bottom of the grain column and the lower half-space to absorb the reflections off the boundary. This absorption prevents possible reflected waves from interfering with the directly transmitted waves. Analytical equations for a single interface indicate that two concurrent boundary conditions are needed to produce no reflection at a single interface: 1) impedance-matched viscous elements at the boundary and 2) a large impedance for the second medium to simulate a rigid material. The specific viscosity at the boundary, η, is set equal to the grain column impedance Z:

$$\eta = Z = \rho c. \tag{5.6}$$

This formula gives values of specific viscosity equal to 13.335×10^6 Pa-s/m for compressional waves and 8×10^6 Pa-s/m for shear waves. The elastic properties of the lower half-space are increased five-fold as an approximation to an infinitely larger impedance.

Figures 5.12 and 5.13 show the wave propagation in the grain column when the boundaries are welded. The wave does not change shape as it propagates through this system, in agreement with the system configured as a solid. Also, the velocities agree with the material properties. The lack of reflection off the lower half-space indicates that the non-reflecting boundary condition has been properly incorporated. The lower magnitude of the third lobes of propagating waves compared to the input waves (Figure 5.10) is an effect due to the coupling between the upper half-space and grain column.

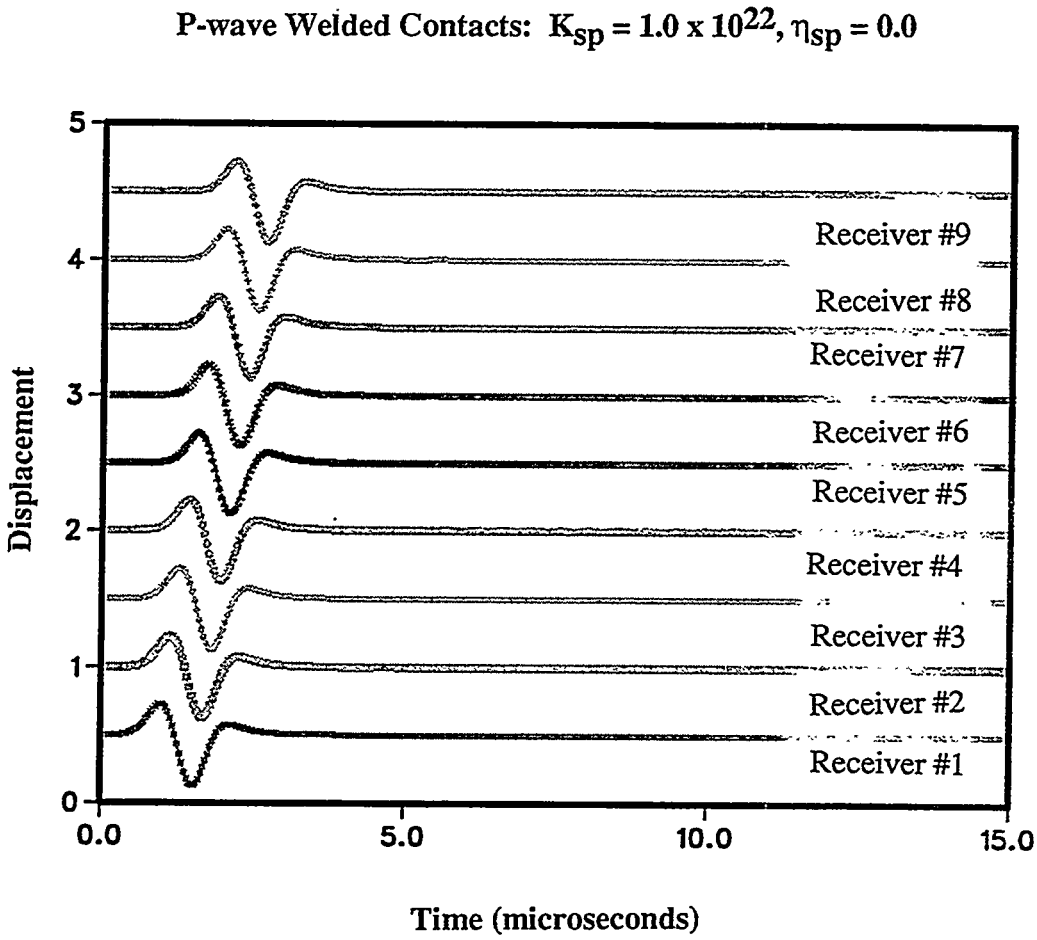

Figure 5.12: Calculated traces for P-wave and simulations for welded grain contacts. The lack of reflection off the bottom boundary indicates that the non-reflecting condition has been properly incorporated.

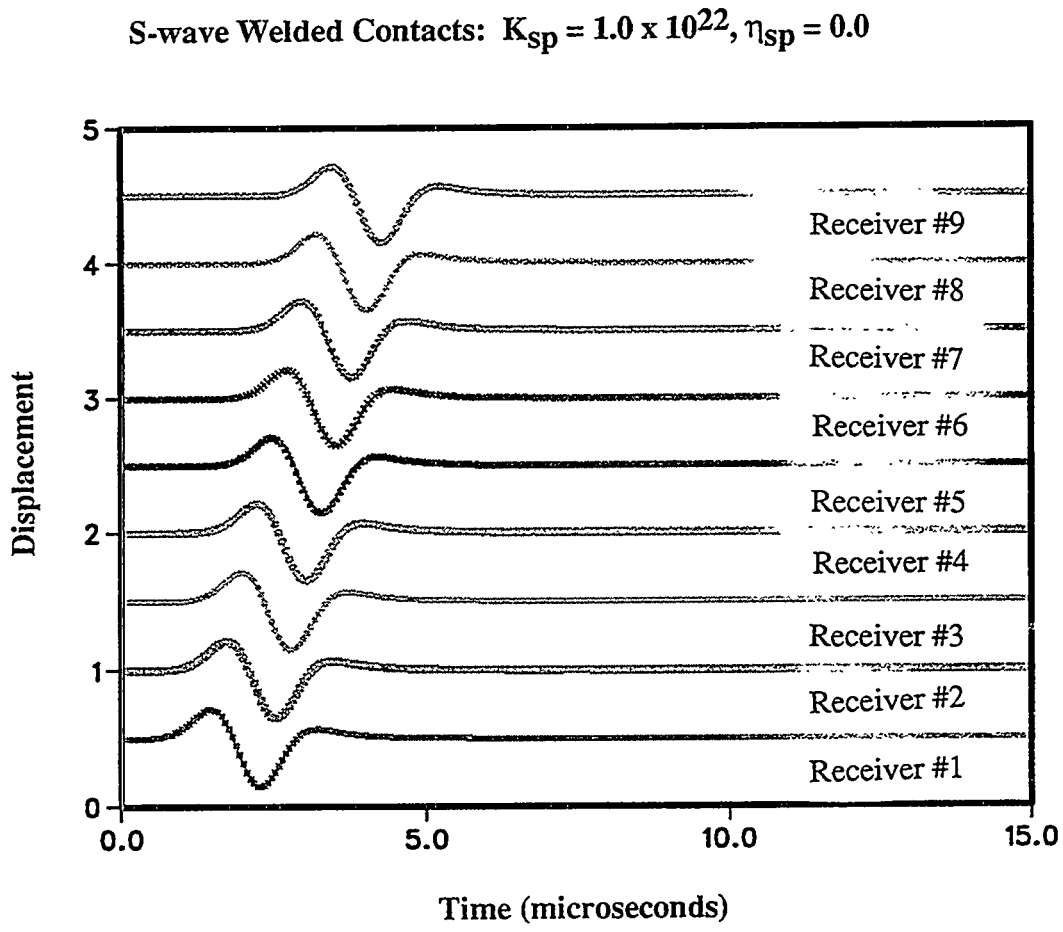

Figure 5.13: Calculated traces for S-wave and simulations for welded grain contacts. The lack of reflection off the bottom boundary indicates that the non-reflecting condition has been properly incorporated.

5.6 Modeling Results

The observed differences in the laboratory specimens were modeled by changing the specific stiffness and specific viscosity in the rheologic boundary between the grains. First, the specific stiffness are varied to match the velocities in the clean dry bead specimens. Then the specific stiffness and specific viscosity are varied to correspond with the addition of clay and water into the grain-to-grain contacts. In all plots, each trace traces is offset along the voltage axis.

5.6.1 Dry Glass Bead Simulation

The laboratory velocities could not be directly modeled due to the different number of interfaces in the specimens and the model. The modeled grains are approximately ten times larger than the laboratory grains, resulting in ten times fewer interfaces in the model than the laboratory specimens. The effect of the differing number of interfaces was investigated using the elastic velocity and effective modulus equations (equations 2.12 and 2.8):

$$c = \sqrt{\frac{E'}{\rho}}$$
$$\frac{1}{E'} = \frac{1}{E} + \frac{n}{K} \qquad (5.7)$$

where c is the velocity, E' the effective modulus, ρ the density, E the intrinsic modulus, n the number of interfaces, and K the interface specific stiffness. Laboratory P and S-wave velocities are used to calculate model velocities given n = 10 for the laboratory data and n = 1 for the numerical models. The P and S-wave laboratory velocities of 1400 and 800 m/sec are transformed to 3500 and 2025 m/sec for the models respectively.

These corrected velocities were matched in the multiple contact modeling trials by varying the specific stiffnesses. Specific stiffnesses of 7.5×10^{13} Pa/m and 2.5×10^{13} Pa/m produced excellent agreements to the corrected velocities for P and S-waves respectively, as shown in Table 5.1. These input data will be used as the clean bead simulations in the section on clay-coated glass beads.

5.6.2 Clay-coated Glass Bead Simulations

The input parameters for the velocity models are used as a base, about which the specific stiffness and specific viscosity values are varied to obtain the behavior seen in the variable water content specimens. Five conditions are modeled: dry clean beads, dry clay-coated beads, low water content clay-coated beads, medium water content clay-coated beads, and high water content clay-coated beads.

Dry clean bead contact parameters were determined by matching the laboratory velocities (section 5.6.1). The addition of dry clay is modeled as an increase in specific stiffness and an introduction of specific viscosity into the system. As water is initially adsorbed into the system, only the specific viscosity increases. Subsequent water additions decrease the specific stiffnesses, but have opposing effects on the specific viscosities of compressional and shear waves due to the different wave motions. Shear wave losses depend on the viscosity of the material at the interface. As the water content of the clay increases, the clay viscosity decreases and so the modeled specific viscosity also decreases. Compressional waves losses depend on the deformation of the clay. At medium water contents near the plastic limit, the clay becomes more deformable. This is modeled by an increase in specific viscosity. At the highest water contents, when clay cohesion changes

Wave Type	Specific Stiffness (Pa/m)	Model Velocity (m/sec)	Modified Laboratory Velocity (m/sec)
P-Wave	7.5×10^{13}	3275	3500
S-Wave	2.5×10^{13}	2030	2025

Table 5.1: Data from calibration test to match laboratory velocities in dry glass beads. The modeled values are in excellent agreement with the laboratory measured values.

and is forced from the contact into the surrounding pore space, the specific viscosity decreases and the specific stiffness increases.

The modeled input contact parameters are given in Tables 5.2 and 5.3. The numerically calculated traces at receiver 9 are shown in Figures 5.14 and 5.15. The laboratory measured traces at the highest stresses are shown for comparison. The modeled trace frequencies are similar to the input frequencies and therefore do not have the frequency losses and variations in frequency losses that the laboratory data exhibit. However, the model traces have only propagated approximately one wavelength in distance. The modeled trace magnitudes do follow the same trends as the laboratory traces: dry clay beads have the largest displacements, followed by the dry clay-coated beads, low clay water content beads, and the medium clay water content beads. The highest clay water content beads have magnitudes higher than the medium water content values and similar to the low water content values. This is investigated quantitatively by comparing quality factors.

Quality factors were calculated by windowing the first period of the modeled traces and using the method of spectral ratios (equation 4.2). Traces from receiver 1 were used as the input waveform reference. The P-wave and S-wave values at the input peak frequencies are given in Tables 5.2 and 5.3 respectively. The quality factors measured in the laboratory are given for comparison. The close agreement between the model and laboratory values indicates that the numerical modeling has accurately captured the energy losses measured in the laboratory. The agreement in quality factors for the dry clean beads is especially notable, since the input parameters were based solely on matching the velocity data. The quality factor data agreements are in spite of the differences in bead size (radii of 400 μm versus ~40 μm) and shape (square versus circular) between the model configuration and laboratory specimens. The differences mean that the values of specific

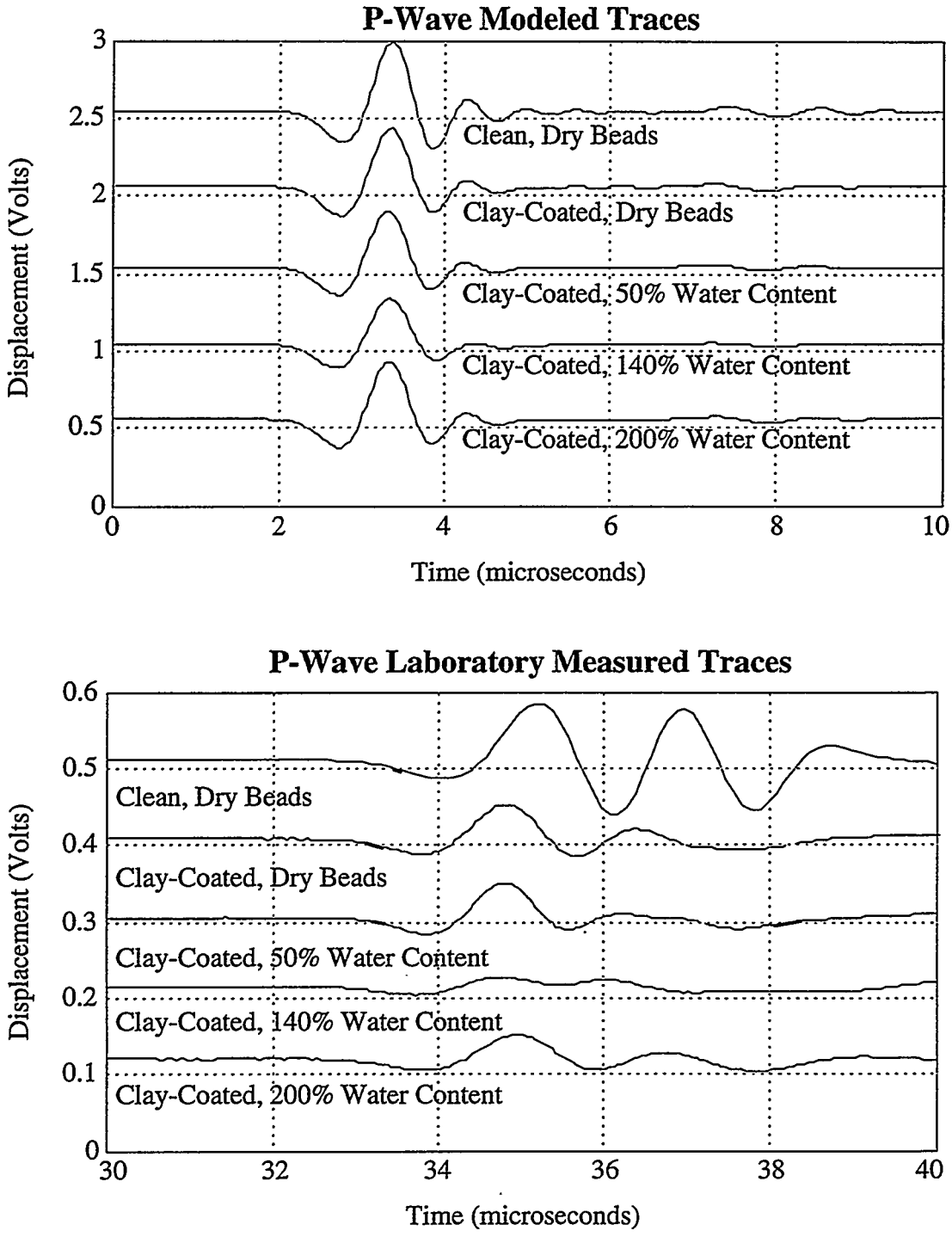

Figure 5.14: (a) Numerically modeled and (b) laboratory measured traces for P-wave propagation in glass bead samples. Laboratory traces have been shifted horizontally to correct for velocity variations in order to facilitate comparisons.

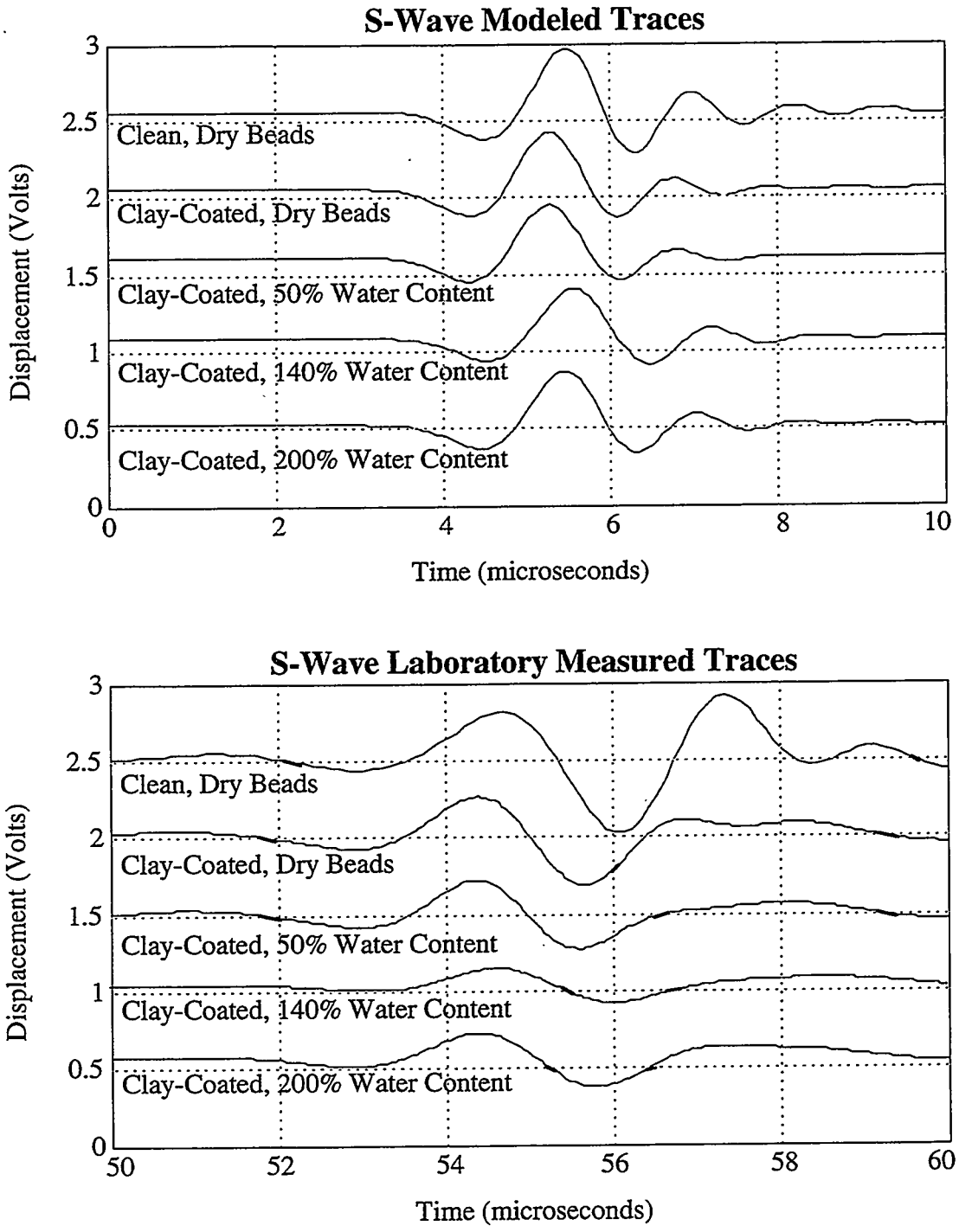

Figure 5.15: (a) Numerically modeled and (b) laboratory measured traces for S-wave propagtion in glass bead samples. The laboratory traces have been shifted horizontally by the velocity variations in order to facilitate comparisons.

Modeled Test	Specific Stiffness (Pa/m)	Specific Viscosity (Pa-s/m)	Modeled Q	Laboratory Q
Dry Clean Beads	7.5×10^{13}	0.0	21.7	22
Dry Clay-Coated Beads	8.0×10^{13}	7.5×10^{5}	14.0	13.6
Clay-Coated Beads, Low Water Content	8.0×10^{13}	1.0×10^{6}	12.8	9.4-13.0
Clay-Coated Beads, Medium Water Content	7.5×10^{13}	2.0×10^{6}	8.8	7.6
Clay-Coated Beads, High Water Content	7.75×10^{13}	8.0×10^{5}	13.4	12.5

Table 5.2: Model parameters and quality factors for P-wave numerical simulations.

Modeled Test	Specific Stiffness (Pa/m)	Specific Viscosity (Pa-s/m)	Modeled Q	Laboratory Q
Dry Clean Beads	2.5×10^{13}	0.0	44.3	44.0
Dry Clay-Coated Beads	3.0×10^{13}	3.0×10^{5}	30.8	31.2
Clay-Coated Beads, Low Water Content	3.0×10^{13}	6.0×10^{5}	20.6	18.0-22.0
Clay-Coated Beads, Medium Water Content	2.25×10^{13}	5.0×10^{5}	14.8	16.1
Clay-Coated Beads, High Water Content	2.50×10^{13}	4.0×10^{5}	19.8	20.0

Table 5.3: Model parameters and quality factors for S-wave numerical simulations.

stiffness and specific viscosity are not directly comparable to laboratory stiffnesses. However, the trends in their values are physically meaningful. They indicate that the attenuation loss mechanisms interpreted from the laboratory data have been accurately characterized and quantified in the numerical models. The agreements are a strong indication that pumping and viscous losses dominate attenuation in granular materials with clay at the contacts.

5.6.3 Grain Size Simulations

Laboratory research has shown that grain size can influence seismic wave propagation (Prasad & Meissner 1992). In these numerical simulations, the modeled grains are approximately ten times larger than the average grain size in the laboratory specimens: 400 μm radius compared to ~37.5 μm radius. The effect of this different grain size is investigated numerically in square-shaped grains by 1) decreasing the grain radius by a factor of two, to 200 μm, 2) increasing the number of grains by a factor of two, to 20 grains, and 3) increasing the rheologic contact parameters by a factor of two. The number of grains are doubled to keep the model distance greater than one wavelength for numerical accuracy. The rheologic parameters are also increased to achieve the same net contact properties. S-wave propagation is simulated with the representative parameters $K_{sp} = 3 \times 10^{13}$, $\eta_{sp} = 5 \times 10^{5}$ Pa/m used as the base case.

The computed traces for the base case and decreased radius grains are given in Figure 5.16. Inspection reveals that first arrival times and thus group velocities for both grain sizes are identical. However, the doubling of the rheologic contact parameters did not produce similar magnitudes. The smaller grain traces have higher amplitudes, and thus less attenuation and higher quality factors, than the larger grain traces. The differences are due to For the amplitudes to match, the rheologic contact parameters should be lower. This

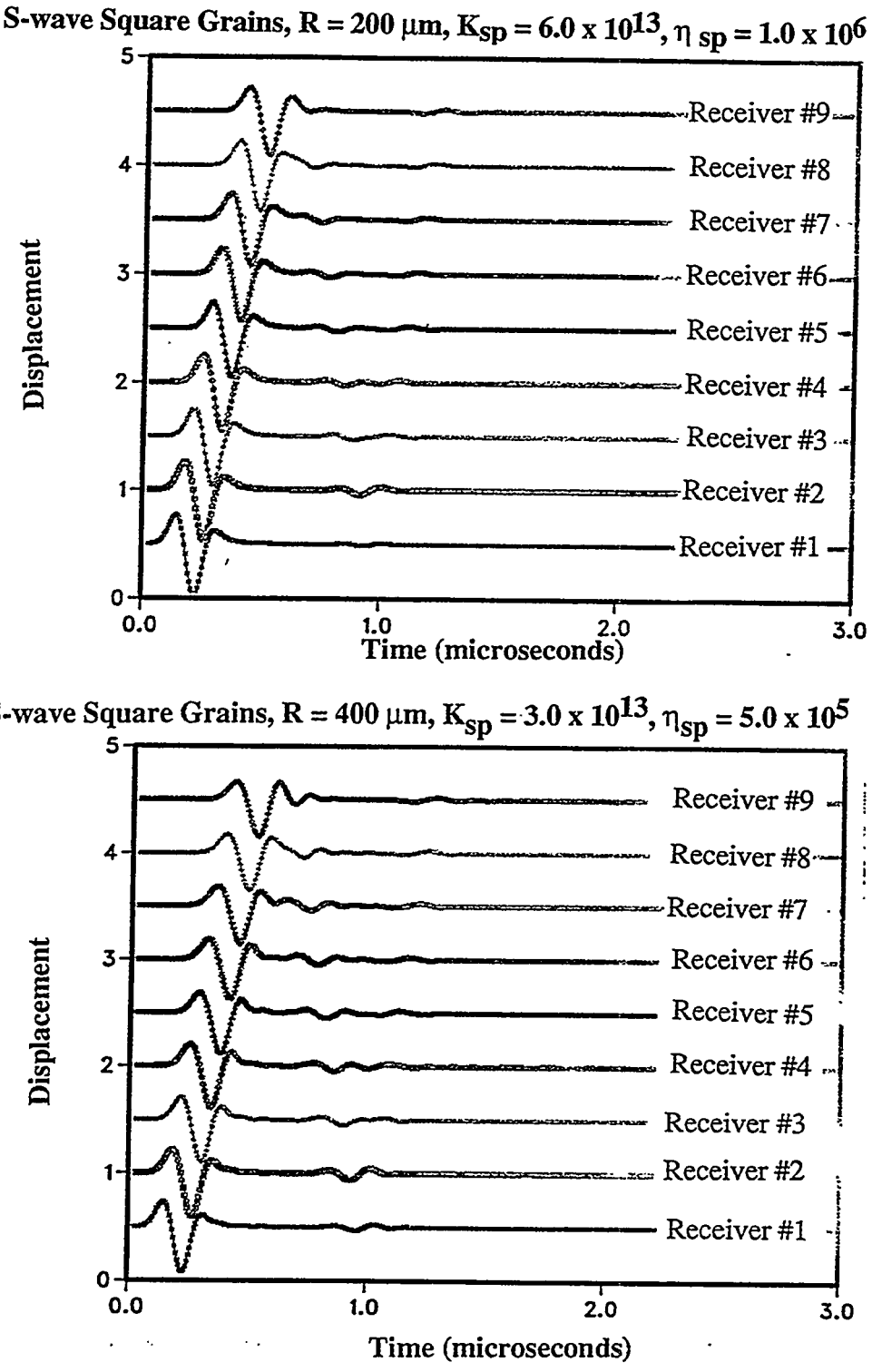

Figure 5.16: Model simulations with grain radius equal to (a) 200 μm and (b) 400 μm grain size. The contact stiffness for the smaller grains are double the larger grains to preserve the overall contact rheology. Group velocities are identical, but the smaller grains transmit more energy.

suggests that to extend the model 400 μm bead radius simulations to the laboratory ~40 μm, the rheologic contact parameters of the models need to be increased, but by less than an order of magnitude. That is, less than the change in the size of the grains.

5.6.4 Grain Shape Simulations

The initial numerical modeling simulations are conducted with square grains, since this modeling work focuses on interpreting grain contact mechanisms. The effects of this approximation are evaluated numerically. Circular grains are approximated as twelve-sided polygons. Grains are connected across one side, which is divided into three boundary elements. The ten non-connected sides have only one boundary element, for a total of sixteen elements per grain. S-wave propagation is simulated through ten grains, each with a radius of 400 μm. Because there are half the number of contact elements in the circular grain simulations compared to the square grain simultions, the contact rheologic properties for the circular grains are doubled in magnitude over the square grain simulations to simulate the same overall contact rheology, since $K \propto 1/\text{Area}$. Again, the representative parameters $K_{sp} = 3 \times 10^{13}$, $\eta_{sp} = 5 \times 10^{5}$ Pa/m are used as the base case.

Figure 5.17 presents the computed traces for the circular grains and square grains. Inspection shows that the first arrival times in the circular grains are later than through square grains. Also, the pulse amplitudes are lower and there is more coda in the circular grains. The smaller direct wave and resultant coda are due to scattering off grain edges and/or multiple reflections. For real glass beads much of this coda will be damped by internal attenuation in the glass beads themselves. The slower group velocities probably arise from the local deformation of the circular grains the vicinity of each contact. This suggests that the use of square grains requires an artificially low contact stiffness to simulate energy transmission. Also, the lower amplitudes indicate that contact viscosities

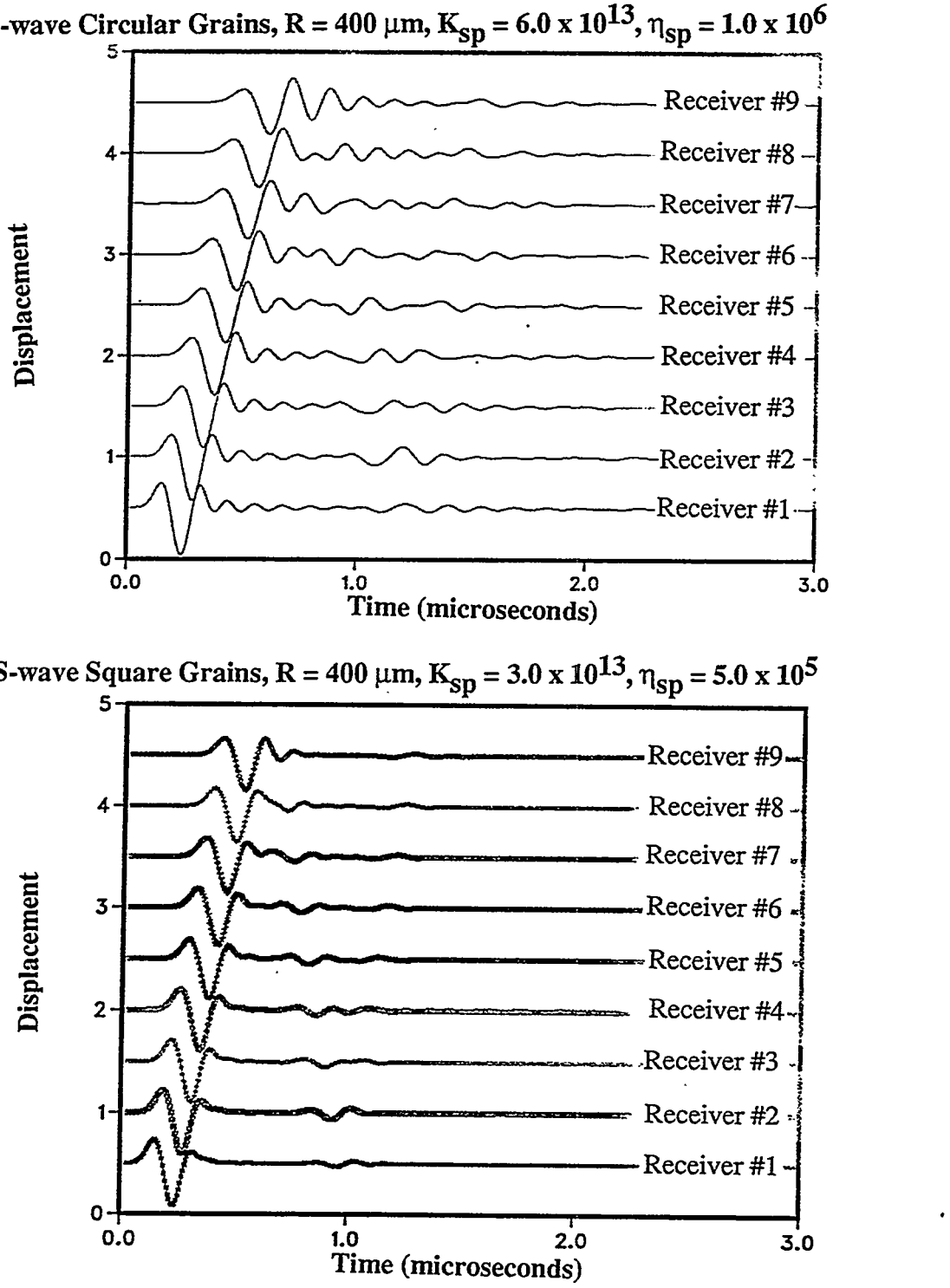

Figure 5.17: Model simulations with (a) circular grains and (b) square grains. Contact parameters for the circular grains are double the square grain values to preserve the overall contact rheology. Group velocities are slower and trace magnitudes are lower for the circular grains.

need to be lower for the laboratory data in order to have similar attenuation, because there is more scattering attenuation.

5.7 Summary and Conclusions

This chapter evaluated the experimental data through numerical techniques to investigate the contact mechanisms and begin the expansion of this work to larger scales. The first technique applied a Butterworth filter to aluminum calibration traces and spectra. Resulting waveforms and spectra were similar to experimental data, confirming that the grain contacts act as low-pass filters. That is, the grain contacts removed the high frequency energy through scattering and attenuation while transmitting the low frequency energy. The peak frequencies of the experimental data could be explained by cutoff frequencies of 400 kHz for P-waves and 250 kHz for S-waves. This is consistent with the contacts acting as displacement discontinuity boundaries.

The experimental data were further analyzed by use of a fully dynamic boundary element method. Seismic wave propagation through a column of grains was solved using Green's functions in the frequency space, then inversely Fourier transforming the computed data to time space. The discontinuous displacement and discontinuous velocity combined boundary condition was incorporated through a complex stiffness. For the Kelvin-Voight rheologic model used in these simulations, the real stiffness corresponds to the specific stiffness and the imaginary stiffness corresponds to the specific viscosity.

In the first simulations, the specific stiffnesses were varied to match the laboratory velocities for dry clean beads. The quality factors for these simulations closely agreed with the quality factors measured in the laboratory. These parameters were then used as a base case for variations in the specific stiffnesses and specific viscosities to correlate with

changes in the clay water content. These simulations showed the correct velocity changes and had quality factors that followed the same trends as the laboratory values and had similar magnitudes. This indicated that the proposed clay rheologic changes due to clay swelling and attenuation mechanisms of pumping and viscous losses had been accurately characterized and properly interpreted.

Further simulations investigated the extensions of the experiments by examining the effects of grain size and grain shape. The relationship between the rheologic parameters and grain size was not directly inverse. Two-fold increases in the rheologic properties as grain size decreased two-fold resulted in similar velocities, but lower magnitudes in the the computed traces. A change in grain shape from the square approximations to circular resulted in delayed arrivals and decreased magnitudes, suggesting that the contact stiffness and contact viscosity parameters determined from the numerical modeling for the clay-coated specimens were smaller than actual values for the laboratory specimens.

6.0: Summary and Conclusions

6.1 Summary and Conclusions

Seismic methods are a very important tool in characterizing the subsurface. Currently, seismic imaging is conducted by using the travel times to delineate the subsurface boundaries of impedance and velocity contrasts. The improvement of field tools now allows the full seismic waveforms to be recorded during testing. The incorporation of attenuation data offers the potential for improved characterization of the subsurface properties, including determination of lithology and fluid type.

The interpretation of attenuation data requires the use of a theoretical model for attenuation losses. A number of models have been proposed for granular materials, including Rayleigh scattering for dry materials, physico-chemical interactions at low saturations, entrapped air bubble resonance and squirt flow for nearly saturated materials, and Biot fluid flow for fully-saturated materials. Studies on single fractures have indicated that these single discontinuities also affect seismic velocities and transmission (Pyrak-Nolte, 1988; Suárez-Rivera, 1992). Recent work on sandstones has indicated that grain contact discontinuities can have an effect equal to the porosity (Nihei, 1992) and that clay can have an effect on attenuation (Klimentos and McCann, 1990). This dissertation is the first research to focus on the mechanics of how clay affects seismic wave propagation.

Experimental tests were conducted using glass beads as a representative granular material. Montmorillonite clay was deposited onto the beads by an evaporation process, resulting in samples with 0.8% clay by dry weight. Scanning electron microscope photographs showed that this procedure resulted in distributed, as opposed to uniform, clay layers on each bead. Polar and non-polar fluids were added to the specimens by the

process of condensation in a clean box with controlled relative humidity. Ultrasonic pulse propagation experiments for both compressional and shear waves were performed under hydrostatic stress conditions. The data were analyzed by comparison of measured velocities and calculated quality factors.

For all specimens, the velocities and quality factors increased with stress. Theoretical contact stiffness models showed that contact stiffness increases with stress. These results indicated that grain-to-grain contacts regulate seismic wave propagation in poorly consolidated and unconsolidated granular materials. Tests on dry and wet specimens showed that the presence of the small amounts of clay at the grain-to-grain contacts increased the seismic velocity and decreased the quality factor. Clay's structure accounted for these changes. Clay is composed of a random assemblage of clay particle aggregates that added both a stiffness and viscosity to the mechancial properties of the grain-to-grain contacts.

A new attenuation mechanism, called pumping loss, was proposed to explain the agreement in the compressional and shear quality factors trends upon variation of the fluid content and fluid type. This mechanism depends upon the rheologic deformation of the clay-fluid mixture at the grain contacts. Stresses during seismic wave propagation caused the clay layer to viscously deform. The clay motion into and out of the surrounding open pore space transfer strain energy into heat. The amount of attenuation depends on the material viscosity. Pumping losses occured at contacts in the propagation direction for compressional waves and at contacts at angles to the propagation direction for shear waves. Propagating shear waves were also subjected to viscous layer losses at the contacts not at 45° angles to the propagation direction. Pumping losses depend on the contact microgeometry, specifically the ease with which the clay can flow as a result of contact deformation. Flat planar interfaces essentially impose uniaxial strain conditions for

compressional waves and hence show negligible pumping losses. Point-to-point contacts have large perpendicular cross-sectional area and so have significant pumping losses.

The experimental quality factor data showed that clay-fluid interactions produce different rheologies that can be detected seismically. The absorption of fluids into the clay did not alter the seismic velocities significantly. Quality factors did vary with fluid content and type. As larger amounts of water were absorbed, the quality factors initially decreased. The quality factors suddenly increased at a water content of 200 percent by weight of clay. This behavior is attributed to clay-fluid interactions. Solvation of the clay's cations caused the clay volume to increase as water was absorbed. Initially, the increase in clay-layer thickness at the grain-to-grain contacts decreased the seismic transmission and associated quality factors. At the high water content, clay appears to have exceeded its plastic limit and flowed in response to applied forces. Local stresses during sample consolidation appear to have forced the clay from the contacts into the surrounding open pore space, where it formed a toroidal mass about the contact. The contact stiffnesses increased due to the removal of clay from the direct contact, thereby increasing the seismic transmission and associated quality factor. The absorption of ethyl alcohol and hexadecane instead of water produced lower quality factors at similar fluid contents. For ethyl alcohol, this is ascribed to different physico-chemical properties, including dipolar strength and molecular size, that reduced the amount of clay swelling. Hexadecane is non-polar and thus did not cause clay to swell. The lower quality factors are believed to be the result of movement between the unbound fluid and the clay particles. These data provide a basis for interpreting fluid properties from seismic measurements.

Numerical techniques were used to investigate the experimental interpretations and to begin the extension of this research to larger scales. Butterworth filters were applied to traces through aluminum standards to explore the frequency effect of the grain-to-grain

contacts. Numerical peak frequencies correlated with the experimental peak frequencies when cutoff frequencies were set to 800 kHz for compressional waves and 525 kHz for shear waves in the Butterworth filters. This agreement confirmed that the grain-to-grain contacts acted as low-pass filters, consistent with displacement discontinuity boundaries.

A combined discontinuous displacement and discontinuous velocity boundary condition was incorporated as a complex boundary rheology into a boundary element code to analyze seismic wave propagation through a column of beads. The fully dynamic boundary element formulation allowed for simulation of both boundary scattering and dissipation. These tests utilized the Kelvin-Voight rheologic model, where the spring and dashpot elements are parallel across the connected elements. To emphasize the grain-to-grain contact effects, the grains were configured as squares in cubic packing as a first-order approximation. Due to memory constraints, the simulated grain sizes were approximately ten times the size of the average laboratory beads. The modeled central frequencies were set equal to the laboratory values: 800 kHz for compressional waves and 525 kHz for shear waves.

In the first simulations, only specific stiffness elements were used to match the laboratory velocities for dry glass beads. The quality factors obtained in these simulations closely matched the laboratory values. These specific stiffnesses were then used as a base case to model the effects of clay and water. The addition of clay was modeled as an increase in specific stiffness and the incorporation of specific viscosity. Water additions were modeled initially as an increase in only the specific viscosity, then decreases in specific stiffness and viscosity. For the largest water contents, the specific stiffnesses were increased to correlate with the movement of the clay from the grain-to-grain contact to the surrounding pore space. These parameter trends were found to give good agreement with the measured laboratory quality factors.

Simulations were performed with changes in bead size, bead shape, and input frequency to investigate their effects on the rheologic parameter magnitudes. Rheologic parameters were found to depend directly on bead size, but to a power less than one. Circular grains required higher rheologic parameter values to produce the same transmission. The difference is attributed to higher scattering losses due to contact geometry. These results suggest that the rheologic parameters for the laboratory samples are higher than the model values given in chapter 5.

6.2 Futher Research

This investigation has confirmed that very small amounts of clay and incorporated fluids at point-to-point grain contacts have measurable effects on seismic wave propagation in the laboratory. Further research must be done before these results can be extended to field interpretations. Laboratory tests at differing clay contents and at higher fluid saturations would determine the range where pumping losses are predominant. Experimental tests on more representative grain shapes would better characterize the importance of pumping and viscous losses. Clay located at contacts should be at critical throats for fluid flow and may also have a direct effect on the permeability of the granular material. In these experiments, the overall high porosity, large pore shapes, and small clay contents were not believed to have affected permeability. Tests both at higher clay contents and with representative grain shapes would establish the possible relationship. Also, the code needs to be modified to permit larger simulations. This will allow a full range of numerical simulations to be performed to extend this research to field frequencies.

REFERENCES

Aki, K. and P.G. Richards. 1980. Quantitative Seismology: Theory and Methods Volume 1. W.H. Freeman and Company, 557 p.

Amari, T., S. Fujioka and K. Watanabe. 1990. "Acoustic properties of aqueous suspensions of clay and calcium carbonate". *Journal of Colloid and Interface Science*, **134**, 2, 366-375.

Anderson, A.L. and L.D. Hampton. 1980. "Acoustics of gas-bearing sediments I. Background". *Journal of the Acoustical Society of America*, **67**, 6, 1865-1889.

Anderson, A.L. and L.D. Hampton. 1980. "Acoustics of gas-bearing sediments II. Measurements and models". *Journal of the Acoustical Society of America*, **67**, 6, 1890-1903.

Angel, Y.C. and J.D. Achenbach. 1985. "Reflection and Transmission of Elastic Waves by a Periodic Array of Cracks". *Journal of Applied Mechanics*, **52**, p.33-41.

Anstey, N.A. 1991. "Velocity in thin section". *First Break*, **9**, 449-457.

Ayers, J.F. 1989. "Application and comparison of shallow seismic methods in the study of an alluvial aquifer". *Groundwater*, **27**, 4, 550-563.

Badri, M. and H.M. Mooney. 1987. "Q measurements from compressional seismic waves in unconsolidated sediments". *Geophysics*, **52**, 772-784.

Bala, M. 1992. "The evaluation of the influence of various parameters on the velocity of elastic wave propagation in a rock medium". *Transport in Porous Media*, **9**, 123-134.

Bass, R. 1958. "Diffraction Effects in the Ultrasonic Field of a Piston Source". *J. Acoust. Soc. Am.*, **30**, 602-605.

Batzle, M. and J. Wang. 1992. "Seismic properties of pore fluids". *Geophysics*, **57**, 11, 1396-1408.

Bedford, A. and M. Stern. 1983. "A model for wave propagation in gassy sediments". *Journal of the Acoustical Society of America*, **73**, 2, 409-417.

Berryman, J.G. 1980. "Confirmation of Biot's Theory". *Appl. Phys. Lett.*, **37**, 382-384.

Berryman, J.G. 1988. "Seismic Wave Attenuation in Fluid-Saturated Porous Media". *Pageoph*, **128**, n.1/2, 423-432.

Berryman, J.G. 1992. "Effective stress for transport properties of inhomogenous porous rock". *Journal of Geophysical Research*, **97**, 17409-17424.

Biot, M.A. 1956. "Theory of propagation of elastic waves in a fluid saturated, porous solid, 1. Low frequency range". *Journal of the Acoustical Society of America*, **28**, 168-178.

Biot, M.A. 1956. "Theory of Propagation of elastic waves in a fluid saturated, porous solid, II. Higher frequency range". *Journal of the Acoustical Society of America*, **28**, 179-191.

Biot, M.A. 1962. "Mechanics of deformation and acoustic propagation in porous media". *Journal of Applied Physics*, **33**, 1482-1498.

Birch, F. and D. Bancroft. 1938. "Elasticity and Internal Friciton in a Long Column of Granite". *Bulletin of the Seismological Soceity of America*, **28**, 243-254.

Blair, D.P. 1990. "A Direct Comparison Between Vibrational Resonance and Pulse Transmission Data for Assessment of Seismic Attenuation in Rock". *Geophysics*, **v.55**, n.1, p.51-60.

Born, W.T. 1941. "The Attenuation Constant of Earth Materials". *Geophysics*, **6**, 132-148.

Bourbie, T. and B. Zinszner. 1985. "Hydraulic and Acoustic Properties as a Function of Porosity in Fontainebleu Sandstone". *Journal Geophysical Research*, **90**, B13, p.11524-11532.

Bourbie, T., O. Coussy and B. Zinszner. 1987. Acoustics of Porous Media. Gulf Publishing Company, Houston. 334 p.

Brandt, H. 1955. "A study of the speed of sound in porous granular media". *Journal of Applied Mechanics*, **22**, 479-486.

Brutsaert, W. and J.N. Luthin. 1964. "The velocity of sound in soils near the surface as a function of the moisture content". *Journal of Geophysical Research*, **69**, 643-652.

Bulau, J.R., B.R. Tittmann, M. Abdel-Gawad, et al. 1984. "The Role of Aqueous Fluids in the Internal Friction of Rock". *Journal of Geophysical Research*, **89**, n.B6, 4207-4212.

Burridge, R. and J.B. Keller. 1981. "Poroelasticity Equations Derived from Microstructure". *Journal of the Acoustical Society of America*, **70**, 1140-1146.

Carpenter, P.J., S.F. Calkin and R.S. Kaufmann. 1991. "Assessing a fractured landfill cover using electrical resistivity and seismic refraction techniques". *Geophysics*, **56**, 1896-1904.

Cheng, C.H. and M.N. Töksoz. 1979. "Inversion of seismic velocities for the pore aspect ratio spectrum of a rock". *Journal of Geophysical Research*, **84**, 7534-7543.

Clark, V.A., B.R. Tittmann and T.W. Spencer. 1980. "Effect of volatiles on attenuation (Q^{-1}) and velocity in sedimentary rocks". *Journal of Geophysical Research*, **85**, 5190-5198.

Corapcioglu, M.Y. 1989. "Wave propogation in porous media -- A review". *unpublished manuscript*, 60 pp.

Crampin, S. 1984. "Effective anisotropic elastic constants for wave propagation through cracked solids". *Geophysical Journal of the Royal Astronomical Society*, **76**, 135-145.

DeMartini, D.C., D.C. Beard, J.S. Danburg, et al. 1976. "Variations of Seismic Velocities in Sandstones and Limestones with Lithology and Pore Fluid at Simulated In Situ Conditions". Proceedings EGPC Exploration Seminar, Nov.15-17, 1976.

DeVilbiss, J.W. 1984. "Some effects of pore fluids on dispersion and absorption of viscoelastic waves". 54th Annual International Meeting and Exposition, Society for Exploration Geophysics, Atlanta, GA, USA.

Dietrich, J.H. and G. Conrad. 1984. "Effect of Humidity on Time- and Velocity-Dependent Friction in Rocks". *Journal Geophysical Research*, **89**, 4196-4202.

Domenico, S.N. 1974. "Effect of water saturation on seismic reflectivity of sand reserviors encased in shale". *Geophysics*, **39**, 759-769.

Domenico, S.N. 1977. "Elastic properties of unconsolidated porous sand reserviors". *Geophysics*, **42**, 1339-1368.

Dutta, N.C. and H. Odé. 1979. "Attenuation and dispersion of compressional waves in fluid-filled porous rocks with partial gas saturation (White model) - Part I: Biot theory". *Geophysics*, **44**, 1777-1788.

Dutta, N.C. and H. Odé. 1979. "Attenuation and dispersion of compressional waves in fluid-filled porous rocks with partial gas saturation (White model) - Part II: Results". *Geophysics*, **44**, 1789-1805.

Dvorkin, J., G. Mavko and A. Nur. 1991. "The Effect of Cementation on the Elastic Properties of Granular Material". *Mechanics of Materials*, **12**, 207-217.

Dvorkin, J., R. Nolen-Hoeksema and A. Nur. 1994. "The squirt-flow mechanism: Macroscopic description". *Geophysics*, **59**, 428-438.

Eberhart-Phillips, D., D.-H. Han and M.D. Zoback. 1989. "Empirical relationships among sesmic velocity, effective pressure, porosity, and clay content". *Geophysics*, **54**, 82-89.

Elliot, S.E. and B.F. Wiley. 1975. "Compressional velocities of partially saturated, unconsolidated sands". *Geophysics*, **40**, 949-954.

Gardner, G.H.F., M.R.J. Wyllie and D.M. Droschak. 1964. "Effects of Pressure and Fluid Saturation on the Attenuation of Elastic Waves in Sands". *Journal of Petroleum Technology*, **16**, 189-198.

Gassman, F. 1951. "Uber die elastizitat poroser medien:". *Vier. der Natur Gesellschaft*, **96**, 1-23.

Geertsma, J. 1961. "Velocity-Log Interpretation: The Effect of Rock Bulk Compressibility". *Soc. Petr. Eng. J.*, **1**, 235-248.

Goldberg, D. and B. Zinszner. 1989. "P-wave attenuation measurements from laboratory resonance and sonic waveform data". *Geophysics*, **54**, 76-81.

Gordon, R.B. and L.A. Davis. 1968. "Velocity and Attenuation of Seismic Waves in Imperfectly Elastic Rock". *J. Geophys. Res.*, **v.73**, p.3917-3935.

Gordon, R.B. and D. Rader. 1971. "Imperfect Elasticity of Rock: Its Influence on the Velocity of Stress Waves", eds. J. Heacock, Structure and Physical Properties of the Earth's Crust. Geophysical Monograph Series, **14**, 235-242.

Hadley, K. 1976. "Comparison of calculated and observed crack densities and seismic velocities in Westerly granite". *Journal of Geophysical Research*, **81**, 3483-3494.

Hamilton, E.L. 1971. "Elastic properties of marine sediments". *Journal of Geophysical Research*, **76**, 579-604.

Han, D. 1986. *Effects of porosity and clay content on acoustic properties of sandstones and unconsolidated sediments*, Stanford University, PhD. Thesis.

Han, D., A. Nur and D. Morgan. 1986. "Effects of Porosity and Clay Content on Wave Velocities in Sandstones". *Geophysics*, **51**, n.11, 2093-2107.

Hornby, B. and W.F. Murphy III. 1987. "V_p/V_s in unconsolidated oil sands: Shear from Stoneley". *Geophysics*, **52**, 502-513.

Hovem, J.M. 1980. "Viscous attenuation of sound in suspensions and high porostiy marine sediments". *Journal of the Acoustical Society of America*, **67**, 1559-1563.

Hölscher, P. 1992. "Numerical simulation of a fluid-saturated soil under a dynamically loaded pile". *Transport in Porous Media*, **9**, 1-2, 73-84.

Hudson, J.A. 1981. "Wave speeds and attenuation of elastic waves in material containing cracks". *Geophysical Journal of the Royal Astronomical Society*, **64**, 133-150.

Ita, S.L., L.R. Myer and N.G.W. Cook. 1994. "Effects of clay-fluid interactions at grain contacts on seismic wave propagation". Proceedings of the 1994 North American Rock Mechanics Symposium, Austin, TX, USA, June 1-4, 1994, eds. Nelson & Laubach. Balkema, Rotterdam, p.783-790.

Ito, H., J. DeVilbiss and A. Nur. 1979. "Compressional and shear waves in saturated rock during water-steam transition". *Journal of Geophysical Research*, **84**, 4731-4735.

Iwasaki, Y.T. 1988. "In-situ seismic velocity and its relationship with soil characteristics in Osaka Bay". Earthquake Engineering and Soil Dynamics II - Recent Advances in Ground-Motion Evaluation, Park City, UT, USA, ASCE. 290-304.

Jaeger, J.C. and N.G.W. Cook. 1969. Fundamentals of Rock Mechanics. Methuen & Co. Ltd., London. 513 p.

Johnston, D.L. and T.J. Plona. 1982. "Acoustic Slow Waves and the Consolidation Transition". *Journal of the Acoustical Society of America*, **72**, 556-565.

Jongmans, D. 1990. "In-situ attenuation measurements in soils". *Engineering Geology*, **29**, 2, 99-118.

Keller, J.D. 1989. "Acoustic wave propagation in composite fluid-satured media". *Geophysics*, **54**, 12, 1554-1563.

Kendall, K. and D. Tabor. 1971. "An Ultrasonic Study of the Area of Contact Between Stationary and Sliding Surfaces". *Proceedings of the Royal Society of London*, **323**, 321-340.

Kjartansson, E. 1979. "Constant Q-wave Propagation and Attenuation". *Journal Geophysical Research*, **84**, 4737-3748,

Klimentos, T. and C. McCann. 1988. "Why is the Biot slow compressional wave not observed in real rocks?". *Geophysics*, **53**, 12, 1605-1609.

Klimentos, T. and C. McCann. 1990. "Relationships among compressional wave attenuation, porosity, clay content, and permeability in sandstones". *Geophysics*, **55**, 8, 998-1014.

Klimentos, T. 1991. "The effects of porosity-permeability-clay content on the velocity of compressional waves". *Geophysics*, **56**, 12, 1930-1939.

Knight, R. and R. Nolen-Hoeksema. 1990. "A laboratory study of the dependence of elastic wave velocities on pore scale fluid distribution". *Geophysical Research Letters*, **17**, 1529-1532.

Knight, R. and J. Dvorkin. 1992. "Seismic and electrical properties of sandstones at low saturations". *Journal of Geophysical Research*, **97**, B12, 17,425-17,432.

Korringa, J., R.J.S. Brown, D.D. Thompson, et al. 1979. "Self-consistent imbedding and the ellipsoidal model for porous rocks". *Journal of Geophysical Research*, **84**, 5591-5598.

Kowallis, B.J., E.A. Roeloffs and H.F. Wang. 1982. "Microcrack studies of basalts from the Iceland Research Drilling Project". *Journal of Geophysical Research*, **87**, 6650-6656.

Kowallis, B.J., L.E.A. Jones and H.F. Wang. 1984. "Velocity-porosity-clay content systematics of poorly consolidated sandstones". *Journal of Geophysical Research*, **89**, B12, 10355-10364.

Kuster, G.T. and M.N. Toksöz. 1974. "Velocity and attenuation of seismic wves in two-phase media: Part 1. theoretical formulations". *Geophysics*, **39**, 5, 587-618.

Lasaga, A.C. 1984. "Chemical Kinetics of Water-Rock Interactions". *Journal of Geophysical Research*, **89**, 4009-4025.

Lucet, N. and B. Zinszner. 1992. "Effects of Heterogeneities and Anisotropy on Sonic and Ultrasonic Attenuation in Rocks". *Geophysics*, **57**, n.8, 1018-1026.

Maconochie, A.J., J.G. Bryden and M.A. Paul. 1991. "Acoustic classification of marine sediments by spectral reflection of ultrasound". Proceedings of the First International

Offshore and Polar Engineering Conference, Edinburgh, Scotland, Int. Society of Offshore and Polar Engineers. 229-238.

Marion, D.P. 1990. *Acoustical, mechanical, and transport properties of sediments and granular materials*, Stanford University. PhD. Thesis.

Marion, D., A. Nur, H. Yin, et al. 1992. "Compressional velocity and porosity in sand-clay mixtures". *Geophysics*, **57**, 4, 554-563.

Marks, S.G. and C. McCann. 1992. "Experimental observations of the relationships between compressional and shear velocities and quality factors of sedimentary rocks". *Society of Exploration Geophysics, 62nd Annual Meeting, New Orleans, October 25-29, 1992*, 666-669.

Mason, W.P., D.N. Beshers and J.T. Kuo. 1970. "Internal Friction in Westerly Granite: Relation to Dislocation Theory". *Journal of Applied Physics*, **41**, 5206-5209.

Mavko, G.M. and A. Nur. 1979. "Wave attenuation in partially saturated rocks". *Geophysics*, **44**, 161-178.

Mavko, G.M. and D. Jizba. 1991. "Estimating grain-scale fluid effects on velocity dispersion in rocks". *Geophysics*, **56**, 12, 1940-1949.

Mavko, G.M. and D. Jizba. 1994. "The relation between seismic P- and S-wave velocity dispersion in saturated rocks". *Geophysics*, **59**, 1, 87-92.

McCann, C. and D.M. McCann. 1985. "A theory of compressional wave attenuation in noncohesive sediments". *Geophysics*, **50**, 8, 1311-1317.

McCann, D.M., R. Baria, P.D. Jackson, et al. 1986. "Application of cross-hole seismic measurements in site investigation surveys". *Geophysics*, **51**, 4, 914-929.

Mehta, C.H. 1983. "Scatterin theory of wave propagation in a two-phase medium". *Geophysics*, **48**, 1359-1370.

Mitchell, J.K. 1991. Fundamentals of Soil Behavior. John Wiley & Sons, New York. 407 p.

Mochizuki, S. 1982. "Attenuation in Partially Saturated Rocks". *J. Geophy. Res.*, **87**, 8598-8604.

Murphy, W.F. 1982. *Effects of Microstructure and Pore Fluids on the Acoustic Properties of Granular Sedimentary Materials*, Stanford University, PhD.

Murphy, W.F. 1982. "Partial saturation on attenuation in Massilon sandstone and Vycor porous glass". *Journal of the Acoustical Society of America*, **71**, 6, 1458-1468.

Murphy, W.F., K.W. Winkler and R.L. Kleinberg. 1984. "Frame modulus reduction in sedimentary rocks: the effect of adsorption on grain contacts". *Geophysical Research Letters*, **1**, 9, 805-808.

Murphy, W.F., A. Reischer and K. Hsu. 1993. "Modulus decomposition of compressional and shear velocities in sand bodies". *Geophysics*, **58**, 2, 227-239.

Nihei, K. 1992. *Micromechanics of seismic wave propagation in granular rocks*, University of California, Berkeley, PhD. Thesis.

O'Connell, R.J. and B. Budiansky. 1974. "Seismic velocities in dry and saturated crack solids". *Journal of Geophysical Research*, **79**, 5412-5426,

O'Connell, R.J. and B. Budiansky. 1977. "Viscoelastic Properties of Fluid Saturated Cracked Solids". *Journal of Geophysical Research*, **v.82**, p.5719-5735,

Ogushwitz, P.R. 1985. "Applicability of the Biot theory. II. Suspensions". *Journal of the Acoustical Society of America*, **77**, 2, 441-452.

Ohya, S. 1986. "In situ P and S wave velocity measurement". Use of In Situ Tests in Geotechnical Engineering, Blacksburg, VA, ASCE. 1218-1235.

Palmer, I.D. and M.L. Traviolia. 1980. "Attenuation by squirt flow in undersaturated gas sands". *Geophysics*, **45**, 12, 1780-1792.

Parks, G.A. 1984. "Surface and Interfacial Free Energies of Quartz". *Journal of Geophysical Research*, **89**, 3997-4008.

Prasad, M. and R. Meissner. 1992. "Attenuation mechanisms in sands: Laboratory versus theoretical (Biot) data". *Geophysics*, **57**, 5, 710-719.

Pyrak-Nolte, L.J., N.G.W. Cook and L. Myer. 1987. "Seismic Visibility of Fractures". University of Arizona, Tucson; 29 June - 1 July 1987: A.A. Balkema, Rotterdam.

Pyrak-Nolte, L.J. 1988. *Seismic Visibility of Fractures*, University of California, Berkeley, PhD. Thesis.

Pyrak-Nolte, L.J., L.R. Myer and N.G.W. Cook. 1990. "Transmission of Seismic Waves Across Single Natural Fractures". *Journal of Geophysical Research*, **95**, B6, 8617-8638.

Quirk, J.P. 1968. "Particle Interaction and Soil Swelling". *Israel Journal of Chemistry*, **6**, 213-234.

Remy, J.-M., M. Bellanger and F. Homand-Etienne. 1994. "Laboratory velocities and attenuation of P-waves in limestones during freeze-thaw cycles". *Geophysics*, **59**, 2, 245-251.

Rokhlin, S.I. and Y.J. Wang. 1991. "Analysis of Ultrasonic Wave Interaction with Imperfact Interface Between Solids". *Review of Progress in Quantitative Nondestructive Evaluation*, **10A**, 185-192.

Rokhlin, S.I. and Y.J. Wang. 1991. "Analysis of Boundary Conditions for Elastic Wave Interaction with an Interface Between Two Solids". *J. Acoust. Soc. Am.*, **89**, 2, 503-515.

Savage, J.C. 1966. "Thermoelastic Attenuation of Elastic Waves by Cracks". *Journal Geophysical Research*, **71**, 3929-3938.

Sayers, C.M. 1981. "Ultrasonic Velocity Dispersion in Porous Materials". *Journal of Physics D: Applied Physics*, **14**, 850-864.

Schoenberg, M. 1980. "Elastic Wave Behavior Across Linear Slip Interfaces". *J. Acoust. Soc. Am.*, **68**, 5, 1516-1521.

Schwartz, L.M. 1984. "Acoustic properties of porous systems: II. Microscopic description". *Transport in Porous Media: Special Issue on Waves in Saturated Media*, **9**, 1-2, 105-118.

Spencer, J.W. 1981. "Stress relaxations at low frequencies in fluid-saturated rocks: attenuation and modulus dispersion". *Journal of Geophysical Research*, 1803-1812.

Sperry, W.C. 1964. "Rheological-model concept". *Journal of the Acoustical Society of America*, **36**, 2, 376-385.

Sposito, G. 1984. The Surface Chemistry of Soils. Oxford University Press, New York. 234 p.

Sridharan, A., N.S.V.V.S.J. Gandhi and S.Suresh. 1990. "Stiffness Coefficients of Layered Soil Systems". *Journal of Geotechnical Engineering*, **116**, 4, 604-624.

Stoll, R.D. and G.M. Bryan. 1970. "Wave Attenuation in Saturated Sediments". *J. Acoust. Soc. Am.*, **47**, 1440-1447.

Strick, E. 1967. "The determination of Q, dynamic viscosity and transient creep curves from wave propagation measurements". *Geophysical Journal of the Royal Astronomical Society*, **13**, 197-218.

Suárez-Rivera, R. 1992. *The influence of thin clay layers containing liquids on the propagation of shear waves*, University of California, Berkeley, PhD. Thesis.

Tittmann, B.R., V.A. Clark and J.M. Richardson. 1980. "Possible mechanism for seismic attenuation in rocks containing small amounts of volatiles". *Journal of Geophysical Research*, **85**, B10, 5199-5208.

Toksöz, M.N., D.H. Johnston and A. Timur. 1979. "Attenuation of seismic waves in dry and saturated rocks - 1. Laboratory measurements". *Geophysics*, **44**, 681-690.

Toksöz, M.N. and C.H. Cheng. 1980. "Velocities of Seismic Waves in Porous Rocks". *Geophysics*, **41**, 621-645.

Toksöz, M.N. and D.H. Johnston. 1981. "Laboratory Measurements of Attenuation", *eds.* M. N. Töksoz and D. H. Johnston, Seismic Wave Attenuation. Society of Exploration Geophysicists, Tulsa, Oklahoma, p.6-12.

Tosaya, C. and A. Nur. 1982. "Effects of diagenesis and clays on compressional velocities in rocks". *Geophysical Research Letters*, **9**, 1, 5-8.

Tosaya, C., A. Nur, D. Vo-Thanh, et al. 1987. "Laboratory seismic methods for remote monitoring of thermal EOR". *SPE Reservoir Engineering*, May, 235-242.

Turgut, A. and T. Yamamoto. 1990. "Mesurements of acoustic wave velocities and attenuation in marine sediments". *Journal of the Acoustical Society of America*, **87**, 6, 2376-2383.

Tutuncu, A.N. and M.M. Sharma. 1992. "The influence of fluids on grain contact stiffness and frame moduli in sedimentary rocks". *Geophysics*, **57**, 12, 1571-1582.

Tutuncu, A.N., A.L. Podio and M.M. Sharma. 1994. "An experimental investigation of factors influencing compressional- and shear-wave velocities and attenuations in tight gas sandstones". *Geophysics*, **59**, 1, 77-86.

van Olphen, H. 1977. An Introduction to Clay Colloid Chemistry. John Wiley & Sons, New York. 301 p.

Vassiliou, M., C.A. Salvado and B.R. Tittmann. 1984. "Seismic Attenuation", ed. R.S. Carmichael, Handbook of Physical Properties of Rocks. CRC Press, Boca Raton, Florida, 295-328.

Vernik, L. 1993. "Microcrack-induced versus intrinsic elastic anisotropy in mature HC-sources shales". *Geophysics*, **58**, 11, 1703-1706.

Wang, Z. and A. Nur. 1992. "Elastic Wave Velocities in Porous Media: A Theoretical Recipe", *eds.* Z. Wang and A. Nur, Seismic and Acoustic Velocities in Reservoir Rocks Volume 2: Theoretical and Model Studies. Society of Exploration Geophysicists, Tulsa, Oklahoma, p.1-35.

Wheeler, S.J. and T.N. Gardner. 1989. "Elastic moduli of soils containing large gas bubbles". *Geotechnique*, **39**, 2, 333-342.

White, J.E. 1983. Underground Sound: Application of Seismic Waves. Elsevier, New York. 249 p.

White, R.E. 1992. "The accuracy of estimating Q from seismic data". *Geophysics*, **57**, 11, 1508-1511.

Winkler, K.W. and A. Nur. 1979. "Pore Fluid and Seismic Attenuation in Rocks". *Geophysical Research Letters*, **6**, n.1, p.

Winkler, K.W., A. Nur and M. Gladwin. 1979. "Friction and Seismic Attenuation in Rocks". *Nature*, **277**, p.528-531.

Winkler, K.W. and A. Nur. 1982. "Seismic attenuation: Effects of pore fluids and frictional sliding". *Geophysics*, **47**, 1, 1-15.

Winkler, K.W. 1983. "Contact stiffness in granular porous materials: Comparison between theory and experiment". *Geophysical Research Letters*, **10**, 1, 1073-1076.

Winkler, K.W. 1983. "Frequency Dependent Ultrasonic Properties of High-Porosity Sandstones". *Journal of Geophysical Research*, **88**, B11, 9493-9499.

Winkler, K.W. and W.F. Murphy. 1984. "Scattering in glass beads: Effects of frame and pore fluid compressibilities". *Journal of the Acoustical Society of America*, **76**, 3, 820-825.

Winkler, K.W. 1985. "Dispersion Analysis of Velocities and Attenuation in Berea Sandstone". *Journal Geophysical Research*, **90**, 6793-6800.

Winkler, K.W., H.L. Liu and D.L. Johnson. 1989. "Permeability and borehole Stoneley waves: Comparison between experiment and theory". *Geophysics*, **54**, 1, 66-75.

Yale, D.P. 1985. "Recent advances in rock physics". *Geophysics*, **50**, 12, 2480-2491.

Yamamoto, T. and A. Turgut. 1988. "Acoustic Wave Propagation through Porous Media with Arbitrary Pore Size Distributions". *J. Acoust. Soc. Am.*, **83**, 1744-1751.